공학박사 학위논문

Development of a Pin Level Thermal/Hydraulics-Neutronics Coupled Core Simulator for High Fidelity Steady-state and Transient Analyses

정상상태 및 과도상태 해석을 위한 고신뢰도 핵특성 연계 봉단위 열수력 노심 모의 코드 개발

2021년 2월

서울대학교 대학원
에너지시스템공학부
알베르토 파치니
Facchini Alberto

Development of a Pin Level Thermal/Hydraulics-Neutronics Coupled Core Simulator for High Fidelity Steady-state and Transient Analyses

정상상태 및 과도상태 해석을 위한 고신뢰도 핵특성 연계 봉단위
열수력 노심 모의 코드 개발

지도 교수 주 한 규

이 논문을 공학박사 학위논문으로 제출함
2021년 1월

서울대학교 대학원
에너지시스템공학부
Facchini Alberto – 알베르토파치니

알베르토파치니의 공학박사 학위논문을 인준함
2021년 1월

위 원 장 조 형 규 (인)
부위원장 주 한 규 (인)
위 원 김 응 수 (인)
위 원 이 은 기 (인)
위 원 조 진 영 (인)

Abstract

A pin level reactor core thermal-hydraulics (T/H) code capable of massively parallel execution is developed and coupled with a transport direct whole core calculation (DWCC) code and with a pin-by-pin SP_3 code for both steady-state and transient neutronics-T/H analyses. The Efficient Simulator of COre Thermal hydraulics (ESCOT) employs the 4-equation drift-flux model for two phase calculations while the numerical solution is obtained by applying the finite volume method and the Semi-Implicit Method for Pressure Linked Equation Consistent (SIMPLEC) algorithm. Important constitutive models to describe key subchannel phenomena, such as turbulent mixing, pressure drops, vapor generation, liquid-vapor interfacial heat transfer and wall heat transfer, are implemented to ensure the validity of subchannel-scale analyses. The ESCOT code solutions are validated through the simulation of various experiments and the comparison between the predicted quantities. The solutions are assessed also by the comparison with the corresponding results of the other subchannel-scale solvers like COBRA-TF, MATRA and/or CUPID.

ESCOT has been successfully employed in steady-state transport DWCC analyses by coupling it with the nTRACER code through a wrapping system. The general coupling technique based on the Picard fixed-point iteration (FPI) has low robustness and the application of relaxation factors leaves too much freedom to the user. Thus, the application of the Anderson Acceleration (AA) as an effort to improve the stability of coupled steady-state calculations is analyzed through a series of 3-

dimensional problems solved with increasing complexity starting from a single assembly steady-state problem to a full core depletion problem via checker-board (CB) problems. The convergence behavior is examined in terms of true error reduction by comparing the intermediate fission source distributions with the fully converged reference solution obtained by applying a very tight convergence criterion. It turns out that the number of neutronics-T/H iterations is reduced considerably because the oscillatory behaviors of the local solutions noted in the ordinary FPI can be smoothened. Convergence is reached earlier with AA so that the computing times of the coupled calculations can be reduced by about 25% retaining the solution accuracy.

In addition, the improvements in both accuracy and details of the time-dependent coupled analyses are shown through the solution of the Main Steam Line Break (MSLB) accident. This scenario involves a considerable reduction of the inlet coolant temperature of one side of the reactor core which results in significant asymmetry in the radial flow characteristics. Because of this asymmetry, the positive reactivity feedback effect introduced by the decrease of the coolant temperature occurs with strong spatial dependence. For sufficient conservatism, a stuck rod in the cold side is assumed during the reactor trip. Thus, employing the pin level solvers increases the fidelity of the calculated results.

Despite the increased performances of transport transient solvers, the computing time is still a burden for the calculation of transients lasting longer than 20*sec* in simulation time. Therefore, ESCOT has been coupled with a pin-by-pin SP_3 based code instead of a DWCC code. The analysis of the Nuclear Energy Agency of the Organization for Economic Cooperation and Development MSLB benchmark is performed by solving the Exercise II problem which does not require system modeling since it provides two sets of core flow boundary conditions.

It turns out that the better neutronics and T/H nodalization of the core leads to a higher SCRAM worth which implies a lower maximum return-to-power when it is compared with assembly-wise solvers (< 2%). It is noted also that the mixing effect between the hot and cold sides is constrained only to the first assembly row and the size of the mixing region increases with the core axial level. A dominant axial velocity and a CB-like power shape around the separation between the two sides are the primary reasons for the lack of mixing beyond the first assembly row. Moreover, the better T/H nodalization describes more reliably the coolant behavior around the stuck rod.

The use of a pin-by-pin solver allows also to capture the high gradient in pin power inside the assemblies close to the stuck rod at the instance of maximum return-to-power, which was not possible with the conventional assembly-wise solvers. The pin-level coupled neutronics-T/H does not increase the computing time noticeably owing to the parallelized execution capability. This study demonstrates the importance of advancing to pin-wise coupled transient analyses in order to fully understand the core power and temperature behaviors in the severe conditions involving highly distorted flow and power distributions.

Keywords: ESCOT, Core Thermal-hydraulics Analysis, Multiphysics, Coupled Neutronics-Thermal/Hydraulics Calculations, Anderson Acceleration, Pin Level Transient Coupled Calculations, Main Steam Line Break (MSLB), Pin-by-pin SP$_3$ Transient Analyses

Student Number: 2017 – 35470

Contents

List of Figures

List of Tables

Chapter 1. Introduction

An accurate prediction of neutronics and thermal-hydraulics (T/H) is necessary to ensure proper performances and safety of the core design. The simulation of reactor cores is generally carried out by integrating various physics (multiphysics) phenomena such as nuclear fission, heat conduction and/or convection. The integrated simulation of neutronics and T/H is essential to incorporate properly the thermal feedback effects. The primary solution of a neutronics-T/H coupled problem is the power distribution determined along with the distributions of temperature, density, velocity and pressure of the coolant as well as the fuel temperature profiles.

Traditionally, the integration of multiphysics phenomena is performed at coarse mesh level due to the limitation of computing power. In the conventional two-step based neutronics calculation, the internal structure of fuel assemblies (FA) is neglected by smearing out the constituents and by using homogenized multi-group cross sections. After that, assembly averaged flow channels are used to calculate the T/H variables. Finally, the pin level (or subchannel) analysis is performed separately to estimate power peaks and/or departure of nucleate boiling ratios (DNBR), namely in a decoupled mode. When using approximated methods and coarse spatial resolution, the prediction accuracy deteriorates and considerable uncertainties are introduced. Thus, some level of conservatism is usually applied in the interpretation of results which may cause penalties in the economics of the nuclear power plant.

The conservatism originated from the approximated solutions has been alleviated in the past decades thanks to the continued enhancement in computing power and performances. The direct whole core calculation (DWCC) together with the pin-by-pin diffusion/Simplified P_3 (SP_3) based analysis have rapidly emerged as improvement means in core design analyses. Examples of DWCC codes are DeCART [1], nTRACER [2] and MPACT [3]. They all employ the planar method of characteristics (MOC) solution based coarse mesh finite difference (CMFD) formulation in solving three-dimensional (3D) neutron transport problems retaining subpin-level heterogeneity. For the axial solution, a SP_3 or MOC kernel is generally used.

On the other hand, examples of pin-by-pin diffusion/ SP_3 based code are NECP-Bamboo2.0 [4], SPHINCS [5] and VANGARD [6]. They employ finite difference method (FDM) or nodal methods implemented within the 3D CMFD framework.

To incorporate T/H effects inside neutronics codes, two main approaches have been employed:

- Implementation of a simplified T/H module which is for closed channels involving no pressure drop. This solution has been adopted by DeCART [1], nTRACER [2], MPACT [3], SPHINCS [5], VANGARD [6].
- Incorporation of an existing subchannel or computational fluid dynamics (CFD) code which requires extensive calculation of the flow field with increased realism. Examples of this type of couled systems are: nTRACER/MATRA [2], MPACT/CTF [7], nTER/CUPID [8], MASTER/CUPID [9], COBAYA4/CTF [10].

Alternating calculations of the neutronics and T/H problems are carried out in order to resolve the thermal feedback effects which induce nonlinear changes in the coefficients of the neutron transport equation, namely, the macroscopic cross sections. This methodology can be regarded as a Picard or fixed-point iteration (FPI).

The main advantage of a FPI based coupling lies in the simplicity of the implementation since it does not require any modification of the two solvers once each field information is exchanged through either an interface or a wrapper code. Moreover, the same scheme can be applied to both steady-state and transient simulations.

A new challenge has been introduced in multiphysics coupling through the Jacobian-Free Newton-Krylov method (JFNK) [11]. The method prevents the access to the full Jacobian matrix and only the action of the Jacobian applied to a vector is performed [12]. The Multiphysics Object Oriented Simulation Environment (MOOSE) framework adopts a Krylov Subspace Method which prevents the construction of the exact Jacobian matrix [13]. Unfortunately, this method cannot be readily and easily applied to existing codes unless significant changes are introduced in the code element [14].

Therefore, the application of a FPI based algorithm is reasonable in the case of neutronics-T/H coupling between two separate codes. Unfortunately, FPI based methods have generally poor robustness and acceleration techniques are required to increase the convergence rate. Toth et al. [15] demonstrated that the Anderson Acceleration (AA) [16] improves the convergence of simplified coupled neutronics-T/H while Hamilton et al. [12] showed similar improvements when the AA was applied to more sophisticated coupled problems. Subsequently Lee [17] applied the algorithm to core problems and showed the reduction of the number of FPI. However, the main reason why AA may improve the robustness of coupled calculations was not found.

In this regard, the improvement of coupled neutronics-T/H calculations in fidelity and performances will be analyzed in this manuscript. The fidelity is improved by replacing the simplified T/H solver with a pin level T/H module while performances are enhanced by applying acceleration techniques and parallelization. The following chapters describe in detail the purpose, objectives and scopes of this research. The differences and the unicity of this work will be treated inside section 1.2 while section 1.3 provides the outlines and the structure of this manuscript.

1.1 Purpose, Objectives and Scopes of the Research

The purpose of this research is to improve the fidelity of coupled neutronics-Thermal/Hydraulics analyses by employing a pin level T/H solver. The main objective is to develop coupled neutronics-T/H highly parallelized systems capable of solving steady-state and transient problems without excessively increasing the burden of the calculation.

In order to achieve the purpose and the objective of this research, a pin level (subchannel-like) nuclear reactor core T/H code, which calculates the flow channel conditions, represents the right compromise between accuracy and performances. Ideally, a two-fluid three-field model would be perfect to completely solve the T/H variables inside a nuclear reactor core. However, the importance of void fraction, complex flow and boiling regimes for coupled neutronics-T/H simulations is minor compared to the one they have in accident conditions. Nonetheless, the Homogeneous Equilibrium Model (HEM) introduces assumptions which do not allow high-fidelity analyses. The Drift-Flux model (DFM) [18] represents a proper accommodation between solution accuracy and calculation performances. The Efficient Simulator of COre Thermal/hydraulics (ESCOT), a pin level core T/H code, has been developed based on the DFM. This code has been written from scratch by Lee [19] in 2016 and subsequently extended to full core coupled analyses [20]. In order to use the code for core design and safety analyses, several additions of models, tasks and application of optimization techniques were in order; such as:

- Modeling: implementation of single and two phase key subchannel level phenomena.
- Validation: accordance between the code and the experimental data.
- Parallelization: application of domain decomposition.
- Coupled Operations: implementation of the solid conduction solver.

The first step is, therefore, represented by the full development and validation of the ESCOT code.

The subsequent step is the establishment of an efficient coupled calculation system between neutronics and T/H for steady-state DWCC analyses employing the Anderson Acceleration. To realize such system, the implementation of an interface and a wrapper code were in order.

The last step is the extension of the coupled analysis to transient scenarios. Thus, ESCOT is coupled with an SP_3 pin-by-pin code to perform efficient time-dependent analyses. To achieve this objective, a new interface has been implemented together with an optimized algorithm.

The steady-state coupled analysis is carried out employing the nTRACER DWCC code while the transient is performed using a code which employs a methodology called direct calculation with multi-level CMFD acceleration, developed by Hwang [21] in his M.Sc. dissertation.

In this study, the range of applications of steady-state analysis has been limited to pressurized water reactors (PWR). A series of coupled 3D DWCC problems are solved with increasing complexity starting from a single assembly problem to a full core depletion problem via checker-board problems in order to demonstrate the mathematical and physical meaning of the AA. At the same time, the range of transient analysis concerned the solution of the Nuclear Energy Agency (NEA) of the Organization for Economic Cooperation and Development (OECD) Main Steam Line Break (MSLB) Exercise II benchmark [22]. This latter part of the research will show the improvements of the results by employing neutronics and T/H pin level solvers.

As previously mentioned, the ESCOT code has been written at four hands and the following section describes in detail the separate and common contributions of the two developers.

1.2 Roadmap of Multiphysics Analyses at SNU Reactor Physics Laboratory

The initial development of the nTRACER code contained a full coupling with the HEM code MATRA [23]. Subsequently, Lee et al. [24] coupled the nTRACER code with the most widely used subchannel code COBRA-TF (CTF) [25], a two-fluid three-field model core T/H code. The performance of the coupled simulations nTRACER/CTF were not good enough with a high burden of the T/H calculation time-fraction. In order to decrease the computation time of T/H, the DFM based code ESCOT was initially developed and verified by Lee in 2016 [19]. Subsequently, two main tasks were necessary in order to complete the steady-state and transient coupling:

- Parallelization, and
- Modeling and Validation

The former task was mainly taken by Lee [26] while the latter was mainly performed by Facchini [27]. Once the validation process and parallelization scheme were completed, the ESCOT code was fully released in 2019 [20].

The following task concerned the development of the coupling interface and fuel conduction solver. With the finalization of those tasks, two DWCC systems nTER/ESCOT [28] and nTRACER/ESCOT [29] were released.

The last steps concerned the implementation and development of the Anderson Acceleration for improving the convergence of steady-state coupled simulations, a solid comparison between two different FPI coupling methods and the transient coupling. In his Ph.D. dissertation, Lee [17] explored and demonstrated the efficiency of the application AA to steady-state problems. He also showed that the application of sequential coupling results faster than tandem coupling in the case of poor load balance between the two coupled codes.

The transient coupling was performed between ESCOT and a SP_3 pin-by-pin code to solve the NEA/OECD MSLB benchmark [30].

In the future, the ESCOT code could be coupled with the nTRACER GPU transient version, since the initial steady-state coupling has been already developed by Kim [31] to simulate transport coupled transient problems or with a system code to create a full PWR primary loop system.

1.3 Outlines of the Thesis

The comprehensive description of the ESCOT code development is provided In Chapter 2, focusing on the implemented models and the two phase validation tests with a brief mention to the parallelization scheme. The validation of the code will be presented by showing the comparison of the ESCOT calculated variables with the experimental data and other codes results.

Chapter 3 shows the analysis of steady-state whole core coupling. The analysis will treat the advantages gained by the application of Anderson Acceleration and will provide a mathematical and physical demonstration of AA's effect in the reduction of the number of FPIs.

Chapter 4 analyzes the improvements of coupled transient calculations when using the ESCOT code as T/H module. Transient coupled analysis generally deals with reactivity insertion accidents (RIA). Two types of scenarios are usually simulated: fast (or prompt) and slow (or delayed) transients. In fast transients the coolant hydraulics variation is generally less important than the fuel temperature one, therefore the benefits of using ESCOT in control rod extraction-like scenarios is minor while in slow transients, such as loss of power/mass flow, turbine trip or MSLB, the use of ESCOT is more beneficial since large asymmetry and mixing are predominant phenomena. In particular, the analysis of the NEA/OECD MSLB benchmark Exercise II is presented. Conclusions are drawn inside Chapter 5.

Chapter 2. Development of a Pin level Thermal-hydraulics code

This section initially introduces the DFM, the calculation algorithm and the discretization approach. Those topics have been explained by Lee in his dissertations [17], [19] and there is not necessity to further them. Subsequently, the subchannel models and the conduction equation solver implemented in ESCOT are detailed. Then, the validation process and results are provided and finally, the parallelization scheme of the pin level thermal/hydraulics code ESCOT is briefly described. This code aims at providing an accurate yet fast core T/H solution. Its target is cluster-level calculations.

As previously mentioned, the ESCOT code adopts the DFM [18]. In particular, the four equation DFM are integrated by applying the Finite Volume Method (FVM) and the solution is calculated employing the Semi-Implicit Method for Pressure-Linked Equation Consistent (SIMPLEC) algorithm [32] in a staggered grid system. The ESCOT solution has been verified and validated towards single phase flow conditions by Lee [19] and here only the validation of the two phase flow validation results is shown.

The ESCOT code is highly parallelized with MPI and it can split its domain planar and assembly-wise. The momentum and pressure systems are solved by using the Block Jacobi preconditioned Bi-Coniugate Gradient with Stabilization (BiCGStab) available inside the PETSc library [33].

2.1 Four-equation drift-flux model

The drift-flux model proposed firstly by Zuber and Findlay in 1965 [18] is one of the available two phase models. The basic simplification of the DFM is to use the mixture velocity in the momentum conservation equation rather than using the gas and liquid velocities individually. This simplification leads to a great advantage that can reduce the computational burden by establishing so-called 5-equations model. By solving only for the mixture energy and assuming the vapor in saturated conditions, the number of equations can further decrease to four. The DFM is in contrast to the two-fluid model that involves 6 or 9 equations in the two-fluid, three-field model. Moreover, this approach avoids the modeling of the interfacial area constitutive relations, one of the most complex and difficult parts in the two-fluid models [34].

In the DFM, the mixture velocity can be separated into each phase velocity by adopting two drift-flux parameters, namely the distribution parameter (C_0) and the drift velocity V_{gj}. Those parameters can be determined by experimental results, and this is the reason why the DFM is a semi-empirical method. By using these parameters, one can model the vapor-liquid velocity slip, which cannot be considered in the standard HEM. The DFM is known as a good and practical model for the bubbly, slug, churn, and counter-current flow [35].

2.1.1 Mixture properties

To formulate the governing equations, some relations have to be defined. First, the mixture properties are defined by Ishii et al. [36]:

- Mixture density as:

$$\rho_m = \alpha\rho_v + (1-\alpha)\rho_l \,. \tag{2.1}$$

- Mixture velocity as:

$$\vec{u}_m = \frac{\alpha\rho_v\vec{u}_v + (1-\alpha)\rho_l\vec{u}_l}{\rho_m} \,. \tag{2.2}$$

- Mixture enthalpy as:

$$h_m = \frac{\alpha\rho_v h_v + (1-\alpha)\rho_l h_l}{\rho_m} \,. \tag{2.3}$$

- Thermodynamic quality:

$$\begin{gathered} x_{th} = \frac{h_{l,fl} - h_{l,sat}}{h_{fg}} \\ h_{l,fl} = \frac{\alpha\rho_v v_v h_v + (1-\alpha)\rho_l v_l h_l}{\alpha\rho_v v_v + (1-\alpha)\rho_l v_l} \end{gathered} \tag{2.4}$$

- Flow quality:

$$x = \frac{\alpha\rho_v v_v}{\alpha\rho_v v_v + \left(1-\alpha\right)\rho_l v_l} \tag{2.5}$$

2.1.2 Drift-flux parameters and phasic velocities

The vapor velocity can be defined as:

$$u_v = j + (u_v - j), \tag{2.6}$$

after performing area average after multiplying both side by void fraction, Eq. (2.6) becomes:

$$\langle j_v \rangle = \langle \alpha j \rangle + \langle \alpha (u_v - j) \rangle, \tag{2.7}$$

where the operation $\langle \cdot \rangle$ represents the flow area averaging as:

$$\langle \phi \rangle = \frac{1}{A} \int \phi dA . \tag{2.8}$$

Let us define the distribution parameter, C_0, and the gas drift velocity V_{gj} as follows:

$$C_0 \equiv \frac{\langle \alpha j \rangle}{\langle \alpha \rangle \langle j \rangle} \quad \text{and} \tag{2.9}$$

$$V_{gj} \equiv \frac{\langle \alpha (u_g - j) \rangle}{\langle \alpha \rangle}, \tag{2.10}$$

thus, Eq. (2.6) becomes as follows:

$$\langle j_v \rangle = \langle \alpha \rangle \langle j \rangle C_0 + \langle \alpha \rangle V_{gj} . \tag{2.11}$$

To derive the drift-flux field velocities, it is necessary to define the phasic relative (or slip) velocity as:

$$u_r = \langle u_v \rangle - \langle u_l \rangle, \tag{2.12}$$

and the relation between the slip velocity and drift flux parameters can be derived as the following by using Eqs. (2.9) and (2.10):

$$u_r = \frac{\langle j \rangle (C_0 - 1) + V_{gj}}{(1 - \langle \alpha \rangle)} = \frac{V'_{gj}}{(1 - \langle \alpha \rangle)} . \tag{2.13}$$

The last challenge to tackle is represented by deriving the final relations for the vapor and liquid velocities expressed in terms of the mixture velocity and the drift-flux parameters. Starting from Eq. (2.2) and replacing each phase velocity with Eq. (2.13), the following relations can be derived:

$$u_l = u_m - \frac{\alpha}{1-\alpha}\frac{\rho_v}{\rho_m} V'_{gj} \quad \text{and} \tag{2.14}$$

$$u_v = u_m + \frac{\rho_l}{\rho_m} V'_{gj} \,. \tag{2.15}$$

The empirical correlations used in the ESCOT for calculating the distribution parameter and the gas drift velocity are described in section 2.5.3.2. This model has been originally developed for one-dimensional (1D) problems and it is here employed for a two-dimensional (2D) one. The general form of the gas drift velocity derived term is given at the numerator of Eq. (2.13). The general formulation of $\vec{V}'_{gj}$, in 2D, can be expressed as:

$$\begin{aligned} \vec{V}'_{gj} &= V'_{gx}\hat{e}_x + V'_{gz}\hat{e}_z = \\ &= \sum_j \langle j \rangle_j \left(C_0 - 1\right) + V_{gj} \end{aligned} , \tag{2.16}$$

where the subscript j represents the two directions. Historically, the gas drift velocity is provided as a function of the gravity vector. Thus, the contribution of V_{gx} is neglected in the calculation of $\vec{V}'_{gj}$

$$\begin{aligned} \vec{V}'_{gj} &= V'_{gx}\hat{e}_x + V'_{gz}\hat{e}_z = \\ &= \langle j \rangle_x \left(C_0 - 1\right)\hat{e}_x + \left[\langle j \rangle_z \left(C_0 - 1\right) + V_{gz}\right]\hat{e}_z \end{aligned} . \tag{2.17}$$

2.2 Balance equations

2.2.1 Mixture mass balance

The mass conservation equation for the mixture *m* follows:

$$\frac{\partial \rho_m}{\partial t} + \nabla \cdot (\rho_m \vec{u}_m) = -\nabla \cdot \left(\vec{W}''_{tm} \right), \tag{2.18}$$

the form of the balance presented in Eq. (2.18) is not the canonical one. In fact, the term on the right-hand side (RHS) represents the horizontal mixture mass transfer and void drift which is detailed in Section 2.5.3.2.

2.2.2 Vapor mass balance

The vapor *v* mass balance for the DFM model is formulated as:

$$\frac{\partial \left(\alpha \rho_v \right)}{\partial t} + \nabla \cdot \left(\alpha \rho_v \vec{u}_m \right) = \Gamma_v - \nabla \cdot \left(\frac{\alpha \rho_l \rho_v}{\rho_m} \vec{V}'_{gj} \right) - \nabla \cdot \left(\vec{W}''_{tm,v} \right), \tag{2.19}$$

where the terms on the RHS represents the vapor generation rate, the drift-flux contribution and the horizontal vapor turbulent mixing and void drift.

2.2.3 Mixture momentum balance

The mixture *m* momentum balance is formulated as follows:

$$\begin{gathered} \frac{\partial \left(\rho_m \vec{u}_m \right)}{\partial t} + \nabla \cdot \left(\rho_m \vec{u}_m \vec{u}_m \right) = \rho_m \vec{g} - \\ -\nabla P + \nabla \cdot \boldsymbol{\tau}_m^{ij} - \nabla \cdot \left(\vec{F}''_{tm} \right) - \nabla \cdot \left(\frac{\alpha}{1-\alpha} \frac{\rho_v \rho_l}{\rho_m} \vec{V}'_{gj} \vec{V}'_{gj} \right) \end{gathered}, \tag{2.20}$$

the sum of all the exerted forces is present on the RHS, such as the body forces, the pressure gradient, the friction, the momentum transfer by turbulent mixing and void drift and the drift-flux contribution. This equation can be further decoupled in axial and radial momentum equations [38].

2.2.4 Mixture energy balance

The mixture energy balance is written in terms of enthalpy balance as:

$$\begin{aligned} \frac{\partial\left(\rho_m h_m\right)}{\partial t} + \nabla\cdot\left(\rho_m h_m \vec{u}_m\right) = -\nabla\cdot\vec{Q}_{tm}^{"} + q_w''' + q_v''' + \\ + \frac{\partial P}{\partial t} - \nabla\cdot\left(\frac{\alpha\rho_v\rho_l}{\rho_m}\left(h_v - h_l\right)\vec{V}_{gj}'\right) \end{aligned} . \tag{2.21}$$

The terms on the RHS represents the horizontal energy exchange because of the turbulent mixing and void drift, the energy transfer rate coming from the heated wall, the possible volumetric heat generation in the fluid (γ heating), the pressure work and the contribution of the drift-flux.

2.3 Equations of state

The solution of the four equations provided in the previous section is possible only for the four primary variables: the mixture velocity u_m, the pressure P, the void fraction α and the liquid enthalpy h_l. The fluid secondary variables are determined using the equations of state. In ESCOT, the water and steam properties are calculated by a set of functions and routines based on either the IAPWS-IF97 [37] or the CTF ASME steam tables [25]. For example, the liquid temperature and density are obtained as a function of the primary variables as:

$$\rho_l = \rho_l(P, h_l), \tag{2.22}$$

$$T_l = T_l(P, h_l)\,. \tag{2.23}$$

Since the vapor is assumed to be saturated, its properties are calculated using only the calculated pressure:

$$\begin{aligned} \rho_v &= \rho_{v,sat}(P) \\ T_v &= T_{v,sat}(P) \\ h_v &= h_{v,sat}(P)\,. \end{aligned} \tag{2.24}$$

2.4 Discretization and solution algorithm

To solve numerically the balance equations provided in Section 2.2, three major actions are necessary. The first one is the discretization of the domain into control volumes (CV). The second one is the integration of the conservation equations inside the CVs and the last one is the establishment of the pressure correction equation in order to apply the SIMPLEC algorithm.

The staggered grid approach allows to define different volumes for scalar and vector variables. Fig. 2.1 shows the three types of meshes used in the ESCOT code.

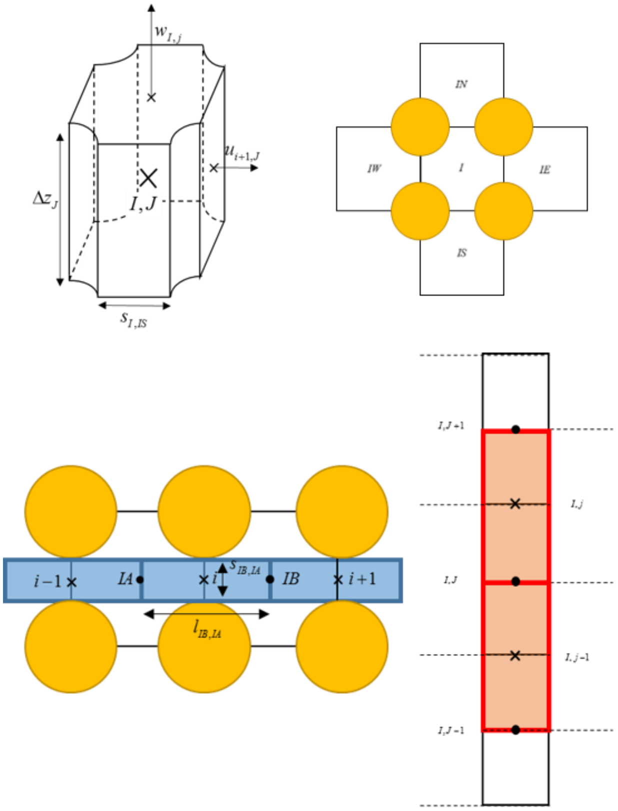

Fig. 2.1: control volumes for the scalar values (*top*), for the radial (*bottom left*) and axial velocity variables (*bottom right*).

The equations are then integrated in the three different types of volume employing first order upwind scheme to the convection terms.

Finally, the pressure correction equation can be derived by linearizing mixture mass, vapor mass and mixture energy balances and by applying the SIMPLEC algorithm. The calculation flow of the ESCOT code is presented inside Fig. 2.2 and Fig. 2.3 for the calculation of steady-state and transient problems where it can be clearly seen the classic nested loop of SIMPLE-like algorithms.

The entire derivation can be found inside the Theory Manual of the code [38].

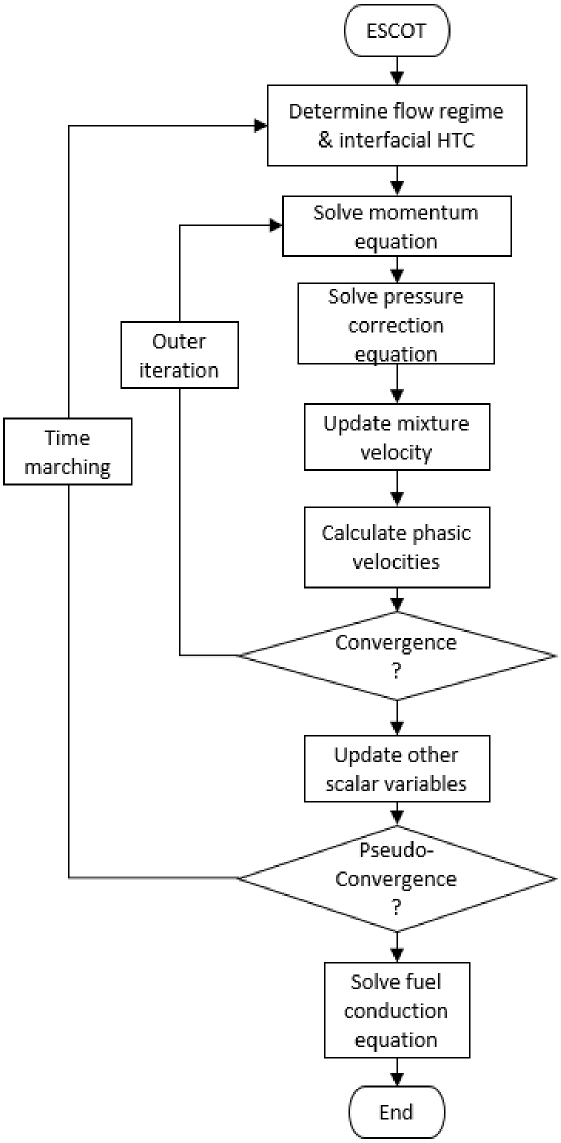

Fig. 2.2: ESCOT calculation flow for steady-state analyses.

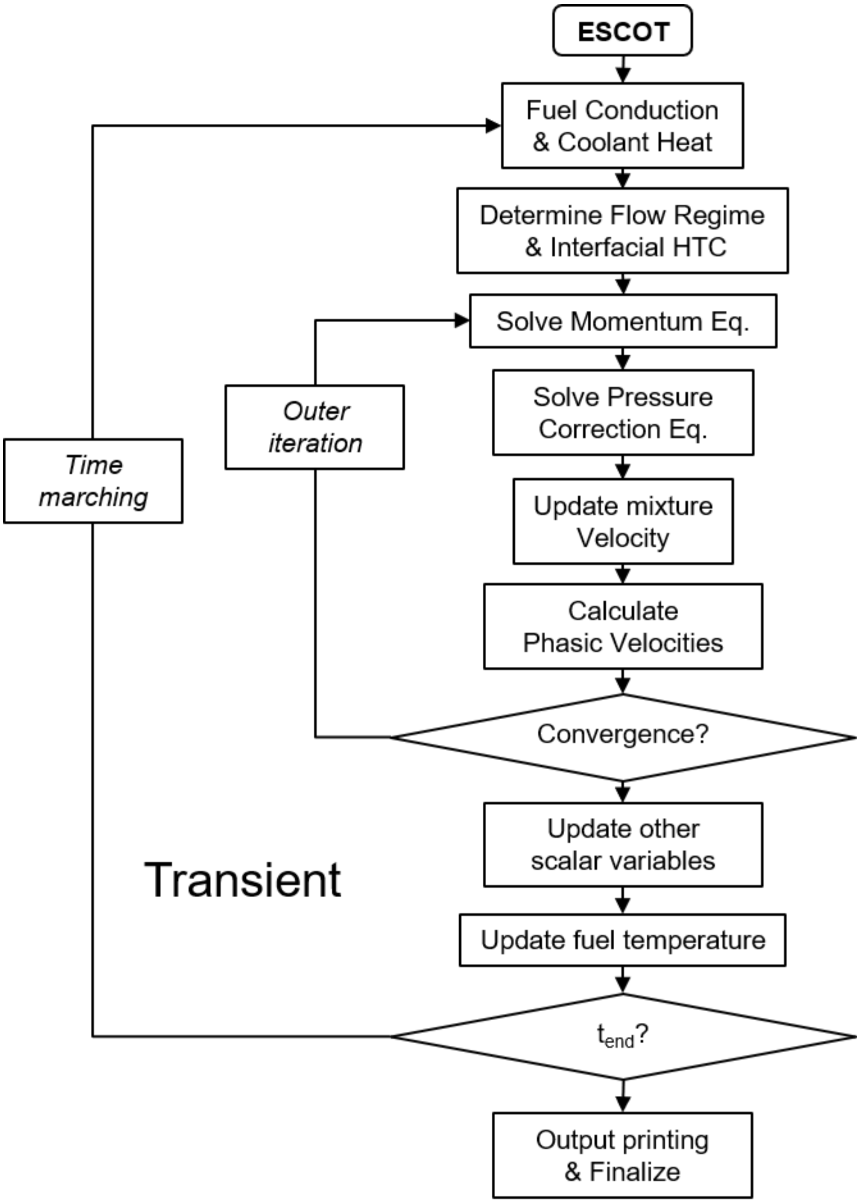

Fig. 2.3: ESCOT calculation flow for transient analyses.

2.5 Description of subchannel-level phenomena

Several subchannel phenomena are present inside a fuel bundle of the nuclear reactor core. This section is to explain the models adopted inside the code in order to represent each term on the RHS of the balance equations presented inside section 2.2. After the initial introduction of the flow and heat regime maps, three more sections will describe the macro-mesh cell closure laws, the micro-mesh cell closure laws and the wall temperature calculation.

2.5.1 Flow regime map

The four balances described in chapter 2.2 contain terms that must be solved before the solution of conservation equations. These terms include the interfacial heat transfer or vapor generation rate. However, these terms are strongly dependent on the behavior of the two phase flow, which is generally classified as one of several flow regimes using the flow regime maps.

RELAP5 [39] and MARS [40] flow regime maps (FRM) for the Pre-CHF have been adopted in ESCOT since the DFM model is very similar to the one used in these two codes. Fig. 2.4 shows the adopted flow regime map. The map depends on the mixture velocity, the void fraction and the $T_v - T_w$. The selection of the flow regime plays a crucial role in the calculation of the interfacial heat transfer coefficient as section 2.5.4.2 will show later.

The ESCOT code accepts five possible regimes:

- Single phase liquid,
- bubbly flow,
- slug flow,

- churn flow, and
- annular flow.

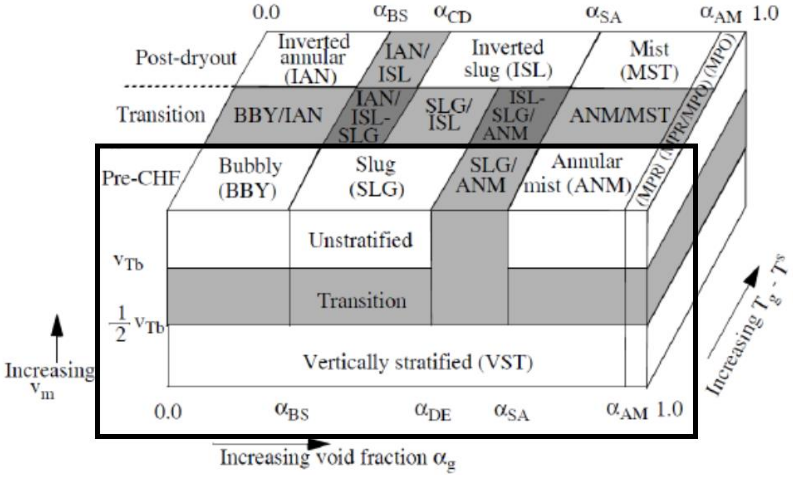

Fig. 2.4: flow regime map of the ESCOT code [41].

2.5.1.1 Single phase liquid

This regime exists in the case of absence of void fraction. In particular for $\alpha < 10^{-5}$.

2.5.1.2 Bubbly flow

The channel is considered in bubbly flow if its velocity is bigger than the Taylor bubble velocity and the void fraction is $0 < \alpha \leq \alpha_{BS}$. The Taylor bubble velocity can be expressed as:

$$v_{TB} = 0.35\left[\frac{gD\left(\rho_l - \rho_g\right)}{\rho_l}\right]^{0.5}, \tag{2.25}$$

$$\alpha_{BS} = \begin{cases} \alpha_{BS}^{*} \quad if\ G_m \le 2000 \\ \alpha_{BS}^{*} + \dfrac{0.5-\alpha_{BS}^{*}}{1000}(G_m - 2000) \quad if\ 2000 < G_m \le 3000 \\ 0.5 \end{cases}, \qquad (2.26)$$

with:

$$D^{*} = D\left[\frac{g\left(\rho_l - \rho_g\right)}{\sigma}\right]^{0.5} \quad \text{and}$$

$$\alpha_{BS}^{*} = \max\left\{0.25\min\left[1.0, 0.045D^{*}\right], 10^{-3}\right\}. \qquad (2.27)$$

2.5.1.3 Slug flow

This regime is constituted of a mix of small and large bubbles. The conditions for a channel to be in slug flow are the following: $v_m > v_{TB}$ and $\alpha_{BS} < \alpha \le \alpha_{DE}$. The Taylor velocity is still calculated like in Eq. (2.25) while the upper limit for the void fraction is taken as following:

$$\alpha_{DE} = \max\left(\alpha_{BS}, \alpha_{SA} - 0.05\right), \qquad (2.28)$$

where α_{BS} is calculated by Eq. (2.26) while α_{SA} is computed according to this procedure:

$$\alpha_{SA} = \max\left[\alpha_{AM}^{min}, \min\left(\alpha_l^{crit}, \alpha_l^{e}, \alpha_{BS}^{max}\right)\right] \qquad (2.29)$$

$$\alpha_l^{crit} = \begin{cases} 0.75 & \text{for downflow} \\ \dfrac{1}{v_g}\left[\dfrac{gD_h\left(\rho_l-\rho_g\right)}{\rho_g}\right]^{0.5} & \text{for upflow} \end{cases}$$

$$\alpha_l^e = \frac{3.2}{v_g}\left(\sigma g\frac{\rho_l-\rho_g}{\rho_l\rho_g}\right)^{0.25} \tag{2.30}$$

$$\alpha_{AM}^{min} = 0.75$$

2.5.1.4 Churn flow

This regime contains large bubbles but respect to slug flow is more chaotic in nature. The idea is to make a blend between slug and annular flow. To consider a fluid in churn flow the conditions to be fulfilled are: $v_m > v_{TB}$ and $\alpha_{DE} < \alpha \leq \alpha_{SA}$.

2.5.1.5 Annular flow

This flow regime is characterized by a liquid film surrounding the wall with a vapor core that can (or cannot) contains droplets. To consider a channel in annular flow, the conditions to be fulfilled are: $v_m > v_{TB}$ and $\alpha_{SA} < \alpha \leq \alpha_{AM}$ with $\alpha_{AM} = 0.9999$.

2.5.2 Boiling regimes

The calculation of the wall temperature requires the computation of the wall heat transfer coefficient which is influenced by the flow conditions. The boiling (or heat) regimes do not coincide with the flow regimes. The ESCOT code recognizes four heat regimes:

- convective heat transfer to liquid: this regime exists if the void fraction is smaller than 10^{-5},

- convective heat transfer to vapor: this regime exists if the void fraction is bigger than 0.9999,
- subcooled nucleate boiling: this unstable regime exists in the conditions of void fraction bigger than 10^{-5} and x_{th} smaller than 0, and
- saturated nucleate boiling: this regime exists when both void fraction and thermodynamic quality are bigger than zero.

Fig. 2.5 is inserted to summarize both the heat and flow regimes [42].

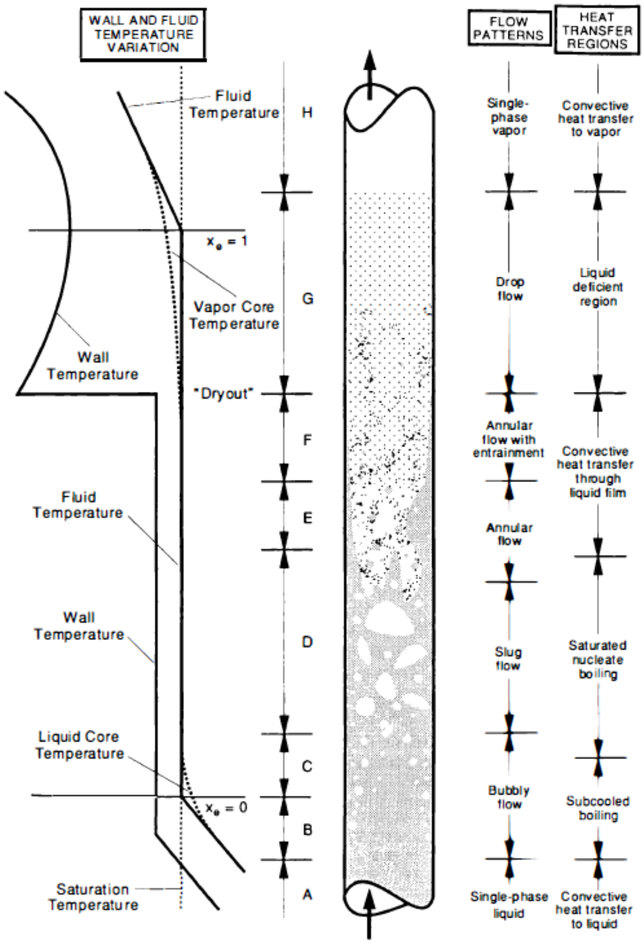

Fig. 2.5: the *boiling channel* with both flow and heat regimes [42].

2.5.3 Macro-mesh cell closure laws

This section describes all the closure laws which apply to the overall channel. These closure parameters include the wall shear stress, the form loss, the drift-flux correlations and the turbulent mixing and void drift.

2.5.3.1 Wall shear stress and form loss

The momentum balance provided in Eq. (2.20) contains the pressure drops induced by friction. This term can be defined as the contribution of two main factors, the wall shear stress and form loss:

$$\nabla \cdot \boldsymbol{\tau}_m^{ij} = -\left(\left.\frac{dP}{dX}\right|_{friction} + \left.\frac{dP}{dX}\right|_{form} \right). \tag{2.31}$$

The first term is only applied to the axial momentum balance since it is the main flow direction, and it is calculated as:

$$\left.\frac{dP}{dX}\right|_{friction,z} = \Phi \left(\sum_k \frac{f}{2D_h} \frac{G_k |G_k|}{\rho_k} \right), \tag{2.32}$$

while the second one is applied to both directions:

$$\begin{aligned} \left.\frac{dP}{dX}\right|_{form,x} &= \Phi \frac{K_x}{2\Delta x} \rho_m u_m |u_m| \\ \left.\frac{dP}{dX}\right|_{form,z} &= \Phi \frac{K_z}{2\Delta z} \rho_m w_m |w_m| \end{aligned}. \tag{2.33}$$

The friction factor *f* is expressed as function of the Reynolds number:

$$f_k = aRe_k^b + c\,, \tag{2.34}$$

where the parameters of Eq. (2.34) are given inside Tab. 2.1.

Tab. 2.1: friction factor default values for the calculation of *f*.

Range of *Re*	***a***	***b***	***c***
$\leq 2{,}300$	64	-1	0
$\leq 30{,}000$	0.316	-0.25	0
$> 30{,}000$	0.184	-0.20	0

The two phasic Reynolds numbers are calculated using the flow quality as:

$$\begin{gathered} Re_l = \frac{(1-x)\rho_l v_l}{\mu_m}, \; Re_v = \frac{x\rho_v v_v}{\mu_m} \\ \mu_m = \left[\frac{1-x}{\mu_l} + \frac{x}{\mu_v}\right] \end{gathered} . \tag{2.35}$$

K represents a form loss factor and it is generally users' dependent. For the axial solution the default value of K_z is zero while for the lateral momentum a default value of $K_x = 0.5$ is used in the ESCOT code.

The last parameter to introduce is the two phase multiplier. In two phase flow, pressure drops are higher than in single phase flow. Since ESCOT treats the friction separately for each phase, the approach proposed by Lockhart and Martinelli [42], which requires the calculation of a factor $\Phi > 1$, is employed. The ESCOT code adopts the two phase multiplier proposed by Armand [43], which is formulated as:

$$\Phi = \begin{cases} 1 & if\ \alpha = 0 \\ \dfrac{(1-x)^2}{(1-\alpha)^{1.42}} & if\ 0 < \alpha \leq 0.6 \\ 0.478\dfrac{(1-x)^2}{(1-\alpha)^{2.2}} & if\ 0.6 < \alpha \leq 0.9 \end{cases} \tag{2.36}$$

2.5.3.2 Drift-flux correlations

The DFM allows to solve the momentum balance equation just for the mixture velocity without losing the information about the two separate phases. In order to do that, two empirical parameters have been introduced and condensed into $\vec{V}'_{gj}$ (Eq. (2.13)). The ESCOT code uses two main empirical formulations to calculate C_0 and V_{gj}. The default correlation has been proposed by Chexal and Lellouche [44]. This correlation has the advantage of being flow regime independent. The distribution parameter is formulated as:

$$C_0 = \frac{L}{K_0 + (1 - K_0)\alpha^{\gamma}}\ , \tag{2.37}$$

where the three parameters L, K_0 and γ are given as:

$$L = \frac{L_n}{L_d} \quad \text{with} \tag{2.38}$$

$$L_n = \begin{cases} 1 - \exp(-\alpha C_1) & \mathit{if}\ \alpha C_1 < 170 \\ 1 & \mathit{otherwise} \end{cases}$$
$$L_d = \begin{cases} 1 - \exp(-C_1) & \mathit{if}\ C_1 < 170 \\ 1 & \mathit{otherwise} \end{cases}\ , \tag{2.39}$$
$$C_1 = \frac{4P_{crit}^2}{P(P_{crit} - P)}$$

$$K_0 = B_1 + (1 - B_1)\left(\frac{\rho_v}{\rho_l}\right)^{0.25} \quad \text{with} \tag{2.40}$$

$$B_1 = \min\left(0.80, \frac{1}{1 + \exp(-\max(\mathrm{Re}_f, \mathrm{Re}_v)/6 \times 10^4)}\right) \quad \text{and} \tag{2.41}$$

$$\gamma = \frac{1 + 1.57(\rho_v / \rho_l)}{1 - B_1}\ . \tag{2.42}$$

The gas drift velocity instead is defined as:

$$\vec{V}_{gj} = 1.41\left[\frac{g\sigma\left(\rho_l-\rho_v\right)}{\rho_l^2}\right]^{0.25} C_2C_3C_4C_5, \tag{2.43}$$

where:

$$C_2 = \begin{cases} 0.4757\left(\ln\dfrac{\rho_l}{\rho_v}\right)^{0.7} & if\ \dfrac{\rho_l}{\rho_v} \le 18 \\ 1 & if\ C_6 \ge 1 \\ \left(1-\exp\left(\dfrac{-C_6}{1-C_6}\right)\right)^{-1} & if\ C_6 < 1\ and\ if\ \dfrac{\rho_l}{\rho_v} > 18 \end{cases},$$

$$C_3 = \max\left[0.5,\ 2\exp\left(\frac{-\left|\mathrm{Re}_f\right|}{6\times10^4}\right)\right], \tag{2.44}$$

$$C_4 = \begin{cases} 1 & if\ C_7 \ge 1 \\ \left(1-\exp\left(\dfrac{-C_7}{1-C_7}\right)\right)^{-1} & if\ C_7 < 1 \end{cases},$$

$$C_5 = \left(1-\alpha\right)^{B_1},\ \ C_6 = \sqrt{150\frac{\rho_l}{\rho_v}}\ \ \text{and}\ \ C_7 = \left(\frac{0.09114}{D_h}\right)^{0.6}.$$

This correlation has validity within the following ranges:

$$0.01 \le \langle\alpha\rangle \le 0.95,$$

$$\left.\begin{matrix} 0.01 \le G \le 2{,}100\,\mathrm{kg/m^2}s \\ 0.1 \le P \le 14.5\mathrm{MPa} \end{matrix}\right\}\text{for diabatic tests}\text{, and}$$

$$\left.\begin{matrix} 0.01 \le G \le 2{,}550\,\mathrm{kg/m^2}s \\ 0.1 \le P \le 18\mathrm{MPa} \end{matrix}\right\}\text{for adiabatic tests}.$$

Additionally, the original drift-flux correlation developed by Zuber and Findlay is implemented inside the ESCOT code [18]. The distribution parameter changes according to the lookup table provided in Tab. 2.2. The bubble diameter d_b is calculated as:

$$d_b = \frac{5\sigma}{\rho_l v_{fg}} \tag{2.45}$$

Tab. 2.2: values of the distribution parameter for Zuber and Findlay correlation.

Flow Regime	**Conditions**	C_0
Bubbly flow	$\alpha < 0.001$	$C_0 = 0.0$
	$d_b < 0.5cm$ $d_b \geq 0.5cm$	$C_0 = 1.2$
Slug flow	-	$C_0 = 1.2$
Churn and Annular flow	-	$C_0 = 1.2$
	$\alpha \geq 0.9$	$C_0 = 1.0$

The gas drift flux velocity is formulated in terms of the bubble rise terminal velocity [42]:

$$V_{gj} = (1-\alpha)^n V_\infty \tag{2.46}$$

The values of V_∞ are provided inside Tab. 2.3.

Tab. 2.3: parameters to calculate the gas drift velocity for Zuber and Findlay correlation.

Flow Regime	**Conditions**	***n***	V_∞
Bubbly flow	$d_b < 0.5cm$	3	$V_\infty = \frac{g(\rho_l - \rho_g)d_b}{18\mu_l}$
	$d_b \geq 0.5cm$	1.5	$V_\infty = 1.53\left[\frac{g\sigma(\rho_l - \rho_g)}{\rho_l^2}\right]^{0.25}$
Slug flow	-	0	$V_\infty = 0.35\left[\frac{g(\rho_l - \rho_g)D_h}{\rho_l}\right]^{0.5}$
Churn and Annular flow	$\alpha \geq 0.9$	0	$V_\infty = 1.53\left[\frac{g\sigma(\rho_l - \rho_g)}{\rho_l^2}\right]^{0.25}$

2.5.3.3 Turbulent mixing and void drift

In a bundle geometry with spacer grids, eddies are always present. Unfortunately, subchannel codes employ fixed geometries and the planar mass, momentum and energy exchange that an eddy present in subchannel (*I,J*) may have with its neighbor cannot be directly caught. To take in account about this physical phenomenon several empirical models have been proposed. The most famous are the Equal Mass exchange Void Drift (EMVD) and the Equal Volume exchange Void Drift (EVVD) [45]. In ESCOT, the EVVD model proposed by Kelly et al. [46] is employed.

Fig. 2.6 sketches the two phenomena. They have generally opposite effect, in fact the mixing model helps the void fraction (and its momentum and energy) to distribute in all the plane while the void drift tends to coalesce the bubbles towards regions with higher void fraction.

The turbulent mixing has the effect of increasing the axial mass flux of a neighbor cell(s) that has lower value and decreasing the analyzed one. Void drift has exactly opposite behavior.

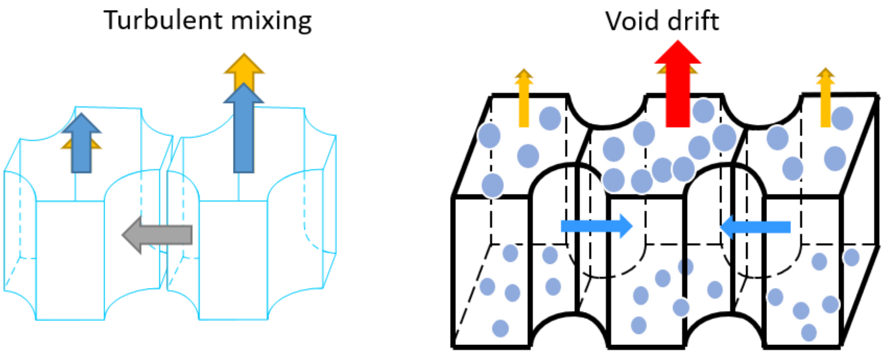

Fig. 2.6: simplified sketch of turbulent mixing model and void drift.

The three terms added to the RHS of the four balance equations are here presented.

Mixture mass exchange:

$$\nabla\cdot\left(\vec{W}_{tm}^{''}\right)=\sum\Theta_{ij}\frac{s_{ij}}{A_i}\left(W_{tm}^{''TM}+W_{tm}^{''VD}\right)=$$
$$=\sum\Theta_{ij}\frac{s_{ij}}{A_i}\left(\frac{\varepsilon}{z_{ij}}\right)\left[\left(\rho_m\right)_i-\left(\rho_m\right)_j\right]- \qquad . \qquad (2.47)$$
$$-\sum\Theta_{ij}\frac{s_{ij}}{A_i}\left(\frac{\varepsilon}{z_{ij}}\right)K_M\frac{G_i-G_j}{G_i+G_j}\left[\left(\alpha\rho_v-\alpha\rho_l\right)_i+\left(\alpha\rho_v-\alpha\rho_l\right)_j\right]$$

Vapor mass exchange:

$$\begin{aligned}\nabla\cdot\left(\vec{W}_{tm,v}^{''}\right)&=\sum\Theta_{ij}\frac{s_{ij}}{A_i}\left(W_{tm,v}^{''TM}+W_{tm,v}^{''VD}\right)\\&=\sum\Theta_{ij}\frac{s_{ij}}{A_i}\left(\frac{\varepsilon}{z_{ij}}\right)\left[\left(\alpha\rho_v\right)_i-\left(\alpha\rho_v\right)_j\right]-\\&-\sum\Theta_{ij}\frac{s_{ij}}{A_i}\left(\frac{\varepsilon}{z_{ij}}\right)K_M\frac{G_i-G_j}{G_i+G_j}\left[\left(\alpha\rho_v\right)_i+\left(\alpha\rho_v\right)_j\right]\end{aligned}\tag{2.48}$$

Momentum exchange:

$$\begin{aligned}\nabla\cdot\vec{F}_{tm}^{''}&=\sum\Theta_{ij}\frac{s_{ij}}{A_i}\left(F_{tm}^{''TM}+F_{tm}^{''VD}\right)_{ij}=\\&=\sum\Theta_{ij}\frac{s_{ij}}{A_i}\left(\frac{\varepsilon}{z_{ij}}\right)\left[\left(\rho_m u_m\right)_i-\left(\rho_m u_m\right)_j\right]-\\&-\sum\Theta_{ij}\frac{s_{ij}}{A_i}\left(\frac{\varepsilon}{z_{ij}}\right)K_M\frac{G_i-G_j}{G_i+G_j}\cdot\\&\cdot\left\{\left[\alpha\left(\rho_v u_v-\rho_l u_l\right)\right]_i+\left[\alpha\left(\rho_v u_v-\rho_l u_l\right)\right]_j\right\}\end{aligned}\tag{2.49}$$

Energy exchange:

$$\begin{aligned}\nabla\cdot\left(\vec{Q}_{tm}^{''}\right)&=\sum\Theta_{ij}\frac{s_{ij}}{A_i}\left(Q_{tm}^{''TM}+Q_{tm}^{''VD}\right)_{ij}=\\&=\sum\Theta_{ij}\frac{s_{ij}}{A_i}\left(\frac{\varepsilon}{z_{ij}}\right)\left[\left(\rho_m h_m\right)_i-\left(\rho_m h_m\right)_j\right]-\\&-\sum\Theta_{ij}\frac{s_{ij}}{A_i}\left(\frac{\varepsilon}{z_{ij}}\right)\left\{\left[\alpha\left(\rho_v h_v-\rho_l h_l\right)\right]_i+\left[\alpha\left(\rho_v h_v-\rho_l h_l\right)\right]_j\right\}\end{aligned}\tag{2.50}$$

ε here is eddy diffusivity, and z^T is tubulent mixing length. K_m denotes the scaling factor whose typical value is taken to be 1.4. It can be flexibly assigned by the user. The mixing coefficient can be reformulated as a function of mass flux [25] as:

$$\frac{\varepsilon}{z_{ij}^T}=\frac{\beta\bar{G}}{\bar{\rho}}.\tag{2.51}$$

The value of the turbulent mixing coefficient *β* is provided by the user. In the case of the two phase multiplier Θ, the model proposed by Beus [47] is used as follows:

$$\Theta = \begin{cases} 1+\left(\Theta_M - 1\right)\left(\dfrac{x}{x_M}\right) & \Rightarrow if \quad x \le x_M \\ 1+\left(\Theta_M - 1\right)\left(\dfrac{x_M - x_0}{x - x_0}\right) & otherwise \end{cases}, \tag{2.52}$$

with:

$$x_M = \frac{0.4\dfrac{\left[\rho_l\left(\rho_l-\rho_g\right)gD_h\right]^{0.5}}{G}+0.6}{\left(\dfrac{\rho_l}{\rho_g}\right)^{0.5}+0.6} \quad \text{and} \tag{2.53}$$

$$\frac{x_0}{x_M} = 0.75\,\mathrm{Re}^{0.0417} \tag{2.54}$$

Default values for *β*, K_M and Θ_M are 0.05, 1.4 and 5.0 [38]. For more information about the implementation strategy, the reader may check the theory manual [38].

2.5.4 Micro-mesh cell closure laws

This section describes all the closure laws which apply to the microscopic level of the cell. These closure parameters only include the wall vapor generation rate and the liquid-vapor interfacial vapor generation rate.

In the ESCOT code, only the vapor mass balance contains interfacial terms. ESCOT uses the same vapor generation rate implemented in RELAP5 [41] where the term is split between the volumetric vapor generation rate from the thermal boundary layer near the wall and the volumetric mass transfer rate between the interface of vapor and liquid. The vapor generation rate can be generally expressed by:

$$\Gamma_v = \Gamma_{iv} + \Gamma_w = \frac{H_{iv}(T_v - T_{sat}) + H_{il}(T_l - T_{sat})}{h_{vi} - h_{li}} + \Gamma_w, \tag{2.55}$$

in the assumption initially made of vapor in saturation condition, Eq. (2.55) becomes:

$$\Gamma_v = \Gamma_{iv} + \Gamma_w = \frac{H_{il}(T_l - T_{sat})}{h_{v,sat} - h_{li}} + \Gamma_w. \tag{2.56}$$

This section will describe the two terms part of Γ_v.

2.5.4.1 Wall vapor generation rate

The model to describe the small bubbles generated next to the thermal boundary layer near the wall is taken from Lahey [48]. The formulation follows:

$$\Gamma_w = \frac{q_w^{"} A_w}{V\left[\max\left(h_{fg}, 10^4 \frac{J}{kg}\right)\right]} F, \tag{2.57}$$

Where the term F is calculated as:

$$F = \frac{h_l - h_{cr}}{\left(h_{l,sat} - h_{cr}\right)\left(1+\varepsilon\right)}, \text{ and} \tag{2.58}$$

$$\varepsilon = \frac{\rho_l \left[h_{l,sat} - \min\left(h_{l,sat}, h_l\right)\right]}{\rho_v h_{fg}}. \tag{2.59}$$

The critical enthalpy h_{cr}, is a fundamental parameter in this empirical model. It sets the threshold in which Γ_w is starting to be calculated. It depends on the Peclet number $Pe = Re \cdot Pr$ as:

$$h_{cr} = \begin{cases} h_{l,sat} - 0.0022\dfrac{q_w^{"} D_h c_{p,l}}{k_l} & if\ Pe < 7\times10^4 \\ h_{l,sat} - 154\dfrac{q_w^{"}}{G} & if\ Pe \geq 7\times10^4 \end{cases} . \tag{2.60}$$

Finally, the actual wall vapor generation rate expressed by Eq. (2.57) is modified into the following stepwise function:

$$\Gamma_w = \begin{cases} 0 & if\ \min\left(h_l, h_{l,sat}\right) < h_{cr} \\ \dfrac{q_w^{"} A_w}{V\left[\max\left(h_{fg}, 10^4 \dfrac{J}{kg}\right)\right]} F & if\ \min\left(h_l, h_{l,sat}\right) \geq h_{cr} \end{cases} . \tag{2.61}$$

2.5.4.2 Liquid-vapor interfacial heat transfer coefficient

Once the flow regime map for the subchannel (*I,J*) is selected according to the rules provided in section 2.5.1, the interfacial heat transfer coefficient H_{il} can be calculated. Each heat transfer coefficient is differentiated between the subcooled (SCL) and superheated (SHL) liquid. A fluid will be considered in SCL state if $T_l < T_{sat}$.

For SCL bubbly flow, the formulation follows the one given by Unal [49]:

$$H_{il} = \frac{F_3 F_5 h_{fg} \rho_g \rho_l \alpha_{bub}}{\rho_l - \rho_g} , \tag{2.62}$$

where:

$$\rho_l - \rho_g = \max\left(\rho_l - \rho_g, 10^{-7} \frac{kg}{m^3}\right), \tag{2.63}$$

$$F_3 = \begin{cases} 1 \quad if\, \Delta T_{sat} < 1.0 \\ \max\left[0.0, F_4\left(1+\Delta T_{sat}\right) - \Delta T_{sat}\right] \;\; if\; -1 < \Delta T_{sat} < 0.0 \\ \max\left[0.0, F_4\right] \;\; otherwise \end{cases}, \tag{2.64}$$

$$F_4 = \min\left[1, \alpha\right], \tag{2.65}$$

$$\alpha_{bub} = \max\left(\alpha, 10^{-5}\right), \tag{2.66}$$

$$F_5 = \begin{cases} 0.075 \qquad if\, \alpha_{bub} < 0.25 \\ 1.8\phi C \exp\left(-45\alpha_{bub}\right) + 0.075 \end{cases}, \tag{2.67}$$

$$C = \begin{cases} 65.0 - 5.69 \cdot 10^{-5}\left(p - 10^5\right) \\ \dfrac{2.5 \cdot 10^9}{p^{1.1272}} \quad if\;\; p > 1.1272 \cdot 10^6 \end{cases} \quad \text{(Pressure in } Pa\text{), and} \tag{2.68}$$

$$\phi = \begin{cases} 1.0 \quad if\, \left|v_l\right| \le 0.61\, m/s \\ \left(1.639344\left|v_l\right|\right)^{0.47} \end{cases}. \tag{2.69}$$

For the SHL bubbly flow, the code chooses between the Plesset et al. [50] and the Lee et al. [51] correlations to express H_{il}:

$$H_{il,bub} = \max\left[-\frac{k_l}{d_b}\frac{12}{\pi}\Delta T_{sat,l}\frac{\rho_l c_{p,l}}{\rho_v h_{fg}}\beta, \frac{k_l}{d_b}\left(2 + 0.74\,\mathrm{Re}_b^{0.5}\right)\right] a_{gf} F_2 F_3 + \\ +0.4 a_{gf}\left|u_l\right| \rho_l c_{p,l} F_1 F_2 F_3 . \tag{2.70}$$

d_b, F_3 and α_{bub} are calculated according to Eqs. (2.45), (2.64) and (2.66) while the other parameters are here provided:

$$\mathrm{Re}_b = \frac{We\sigma\left(1-\alpha_{bub}\right)}{\mu_l\left(v_{fg}^2\right)^{0.5}}, \tag{2.71}$$

$$We = 5,\;\; \beta = 1.0,\;\; We\sigma = \max\left(We\sigma, 10^{-10}\right), \tag{2.72}$$

$$a_{gf} = \frac{3.6\alpha_{bub}}{d_b}, \tag{2.73}$$

$$v_{fg} = \begin{cases} v_g - v_l & if\,\alpha > 10^{-5} \\ \alpha\left(v_g - v_l\right)10^5 \end{cases}, \tag{2.74}$$

$$v_{fg}^2 = \max\left[v_{fg}^2, \frac{We\,\sigma}{\rho_l \min\left(D'\alpha_{bub}^{1/3}, D_h\right)}\right], \tag{2.75}$$

$$D' = 0.005\ \ m,$$

$$F_1 = \frac{\min\left(0.001, \alpha_{bub}\right)}{\alpha_{bub}} \quad \text{and} \tag{2.76}$$

$$F_2 = \frac{\min\left(0.25, \alpha_{bub}\right)}{\alpha_{bub}}. \tag{2.77}$$

The adopted approach for slug flow is to considered two main contributions to the heat transfer:

- the heat transfer between large bubble and the liquid surrounding them, and
- the heat transfer between the small bubble in the slug liquid and their host liquid, so that

$$H_{il} = H_{il,Tb} + H_{il,bub}. \tag{2.78}$$

For SCL slug flow, $H_{il,Tb}$ follows the approach proposed by Kreith [52]:

$$H_{il,Tb} = 1.18942\,\mathrm{Re}_l^{0.5}\,\mathrm{Pr}_l^{0.5}\,\frac{k_l}{D}\alpha_{Tb}a_{gf,Tb}^*, \tag{2.79}$$

where:

$$a_{gf,Tb}^* = \frac{4.5\varepsilon}{D} \quad with\,\varepsilon = 2.0, \tag{2.80}$$

$$\alpha_{Tb} = \frac{\alpha - \alpha_{gs}}{1 - \alpha_{gs}}, \tag{2.81}$$

$$\alpha_{gs} = \alpha_{BS} F_9, \tag{2.82}$$

$$F_9 = \exp\left[-8\left(\frac{\alpha - \alpha_{BS}}{\alpha_{SA} - \alpha_{BS}}\right)\right] \text{ and} \tag{2.83}$$

$$\Pr_l = \frac{c_{p,l}\mu_l}{k_l}, \ \ \mathrm{Re}_l = \frac{\rho_l D \min\left(\left|v_g - v_l\right|, 0.8\right)}{\mu_l}. \tag{2.84}$$

For the SHL instead, the code uses the RELAP5 ad hoc correlation [41]:

$$H_{il,Tb} = 3.0 \cdot 10^6 \alpha_{Tb} a^*_{gf,Tb}, \tag{2.85}$$

where each coefficient is calculated with the relations of the SCL $H_{il,Tb}$.

For both SCL and SHL, $H_{il,bub}$ is calculated as the bubbly flow, with the following modifications for the SHL condition:

$$\alpha_{bub} = \alpha_{BS} F_9, \tag{2.86}$$

$$v_{fg} = \left(v_g - v_f\right) F_9^2, \tag{2.87}$$

$$a_{gf,bub} = \left(a_{gf}\right)_{bub} \left(1 - \alpha_{Tb}\right) F_9 \ \text{ and } \ \beta = F_9. \tag{2.88}$$

$\left(a_{gf}\right)_{bub}$ is calculated according to Eq. (2.80).

Churn and annular flow regimes are characterized by liquid covering the wall and surrounding a vapor core in which entrained droplets may be dispersed. Therefore, ESCOT adopts an additive model for the interface heat transfer coefficient:

$$H_{il} = H_{il,ann} + H_{il,drp}. \tag{2.89}$$

The annular contribution of SCL follows Theofanous' approach [53], in which:

$$H_{il,ann} = \rho_l c_{p,l} \left|v_l\right| a_{gf,ann} F_{10} \cdot 10^{-3}, \tag{2.90}$$

where:

$$a_{gf,ann} = \left(\frac{4C_{ann}}{D}\right)\left(1-\alpha_{ff}\right)^{0.5}, \tag{2.91}$$

$$C_{ann} = \varepsilon\left(30\alpha_{ff}\right)^{0.125} \quad with\, \varepsilon = 2.5, \tag{2.92}$$

$$\alpha_{ff} = \max\left[0.0, \left(1-\alpha\right)F_{11}\right], \tag{2.93}$$

$$F_{11} = \gamma^* \max\left[0.0, \left(1-G^*\right)\right]\exp\left(-7.5\lambda^6 \cdot 10^{-5}\right), \tag{2.94}$$

$$\lambda = \frac{\alpha v_g}{v_{crit}}, \tag{2.95}$$

$$v_{crit} = 3.2\frac{\left[\max\left(\sigma, 10^{-7}\right)g\left(\rho_l - \rho_v\right)\right]^{0.25}}{\rho_v^{0.5}}, \tag{2.96}$$

$$G^* = Re_l^{0.25} \cdot 10^{-4}, \ Re_l = \frac{\left(1-\alpha\right)\rho_l \left|v_l\right| D}{\mu_l}, \tag{2.97}$$

$$\gamma^* = \begin{cases} \dfrac{1-\alpha-\alpha_{AD}}{\alpha_{ED}-\alpha_{AD}} & if\ \alpha > \alpha_{SA}\ and\ 1-\alpha < \alpha_{EF} \\ 1 & \end{cases}, \tag{2.98}$$

$$\alpha_{AD} = 10^{-4}, \ \alpha_{EF} = \max\left[2\alpha_{AD}, \min\left(2.0 \cdot 10^{-3}\frac{\rho_g}{\rho_l}, 2.0 \cdot 10^{-4}\right)\right] \text{ and} \tag{2.99}$$

$$F_{10} = \min\left(1.0 + \left|\lambda\right|^{0.5} + 0.05\left|\lambda\right|, 6.0\right). \tag{2.100}$$

Those parameters are used also for the Ishii et al. [36] correlation which is employed for SHL:

$$H_{il,ann} = 3.0 a_{gf,ann} F_{10} \cdot 10^6. \tag{2.101}$$

Both SCL and SHL adopts the Brown correlation [54] for $H_{il,drp}$:

$$H_{il,drp}=\frac{k_l}{d_d}F_{12}F_{13}a_{gf,drp}, \tag{2.102}$$

in which,

$$a_{gf,drp}=\frac{3.6\alpha_{fd}}{d_d}\left(1-\alpha_{ff}\right), \tag{2.103}$$

$$F_{13}=2.0+7.0\min\left[1.0+\frac{c_{p,l}\max\left(0,\Delta T_{sat,l}\right)}{h_{fg}},8.0\right], \tag{2.104}$$

$$d_d=\frac{We\sigma}{\rho_v\bar{v}_{fg}^{2}},\ \ We=1.5,\ \ We\sigma=\max\left[We\sigma,10^{-10}\right], \tag{2.105}$$

$$\bar{v}_{fg}^{2}=\max\left[v_{fg}^{**2},\frac{We\sigma}{\rho_v\min\left(D'\alpha_{fd}^{1/3},D\right)}\right], \tag{2.106}$$

$$v_{fg}^{**}=\begin{cases}v_{fg}^{*}\left(1-\alpha\right)\cdot10^{6} & \\ v_{fg}^{*} & if\left(1-\alpha\right)\geq10^{-6}\end{cases}, \tag{2.107}$$

$$v_{fg}^{*}=\begin{cases}v_{fg}\left(1-F_{11}\gamma\right) & if\,\alpha>\alpha_{SA}\,and\,1-\alpha<\alpha_{EF}\\ v_{fg}\left(1-F_{11}\right) & otherwise\end{cases}, \tag{2.108}$$

$$v_{fg}=v_g-v_l,$$

$$D'=0.0025,\ \ \alpha_{fd}=\max\left(\frac{1-\alpha-\alpha_{ff}}{1-\alpha_{ff}},\alpha_{AD}^{*}\right), \tag{2.109}$$

$$\alpha_{AD}^{*}=\begin{cases}\alpha_{AD}\gamma+\left(1-\gamma\right)\cdot10^{-5} & if\,\alpha>\alpha_{SA}\,and\,1-\alpha<\alpha_{EF}\\ \alpha_{AD} & \end{cases}\quad\text{and} \tag{2.110}$$

$$F_{12}=1+\xi\left(250+50\xi\right)\ \text{and}\ \ \xi=\max\left(0,-\Delta T_{sat,l}\right). \tag{2.111}$$

2.5.5 Wall temperature calculation

In the solution of coupled neutronics-T/H calculation, the temperature of clad, gap and fuel are necessary variables to solve the problem together with the moderator density and temperature. The solid temperature is connected to the coolant state through the wall temperature. Regardless from the surface material, the connection between a heated surface and the bulk is given by:

$$q'' = h\left(T_w - T_{bulk}\right). \tag{2.112}$$

Thus, for calculating the wall temperature is necessary to know the wall heat transfer coefficient. *h* depends on the boiling regimes defined in section 2.5.2. In general, the heat transfer coefficient is a function of several parameters:

$$h = h\left(Re, Pr, \mu, x, T_w, T_l \ldots\right). \tag{2.113}$$

The following sections describe the empirical correlations and the strategy used inside ESCOT to calculate the heat transfer coefficients for each boiling regime.

2.5.5.1 Single phase liquid

In most of simulated cases, ESCOT deals with single phase forced convection liquid. ESCOT chooses the wall heat transfer coefficient between the Dittus-Boelter [55] and Sparrow [56] correlations:

$$h = \max\left(0.023\frac{k_l}{D_h}\mathrm{Re}_l^{0.8}\,\mathrm{Pr}_l^{0.4}, 7.86\frac{k_l}{D_h}\right). \tag{2.114}$$

In this heat regime the bulk temperature coincides with the liquid one.

2.5.5.2 Single phase vapor

This case is rarely used by ESCOT but it has been implemented anyway. The correlation used for this heat regime follows:

$$h = \max\left(0.023\frac{k_v}{D_h}\mathrm{Re}_v^{0.8}\,\mathrm{Pr}_v^{0.4}, 0.07907\frac{k_g}{D_h}\mathrm{Re}_v^{0.6774}\,\mathrm{Pr}_v^{0.333}, 10\frac{k_g}{D_h}\right), \quad (2.115)$$

the code chooses between the maximum value between the one provided by the Dittus-Boelter [55] or Wong-Hochreiter [57] correlation or by imposing a Nusselt number of 10. In this regime, the bulk temperature coincides with the vapor one.

2.5.5.3 Saturated nucleate boiling

Since the subcooled boiling (SCB) is an intermediated and metastable heat transfer regime, the saturated nucleate boiling (SaNB) is treated before and the SCB will be explained using the SPL and the nucleate boiling (NB) conditions.

The approach adopted in ESCOT is the Chen one [58]. In his paper, Chen postulates a partition of the heat transfer in a convective (*fc*) component and a nucleate boiling (*nb*) one:

$$q" = \left(h_{fc} + h_{NB}\right)\left(T_w - T_{sat}\right). \quad (2.116)$$

ESCOT users can choose through an input card three different correlations: Thom [59], Jens-Lottes [60] and Chen. For what concerns Thom and Jens-Lottes derivations, the convective part is treated as SPL using the Dittus-Boelter correlation given in Eq. (2.114) while Chen developed a modified Dittus-Boelter correlation:

$$h_{fc} = 0.023\left(\frac{G(1-x)D_h}{\mu_l}\right)^{0.8}\mathrm{Pr}_l^{0.4}\,F_{Chen}, \quad (2.117)$$

the Chen's factor is defined as a function of the Martinelli's parameter:

$$\frac{1}{X_{tt}} = \left(\frac{x}{1-x}\right)^{0.9} \left(\frac{\rho_l}{\rho_g}\right)^{0.5} \left(\frac{\mu_g}{\mu_l}\right)^{0.1} \quad \text{and} \tag{2.118}$$

$$F = \begin{cases} 1.0 & if \ \dfrac{1}{X_{tt}} < 0.1 \\ 2.35\left(0.213 + \dfrac{1}{X_{tt}}\right)^{0.736} & \end{cases} . \tag{2.119}$$

The NB component has similar definitions for the Thom and Jens-Lottes correlations. Both correlations express the heat transfer coefficient in *W/*(*m*^{2}*K*) and depend on just the channel pressure (in *MPa*) and $T_w - T_{sat}$:

$$h_{NB} = \frac{10^6 \exp\left(\dfrac{p}{4.35}\right)}{515.29}\left(T_w - T_{sat}\right) \quad \text{Thom and} \tag{2.120}$$

$$h_{NB} = \frac{10^6 \exp\left(\dfrac{p}{1.55}\right)}{2.56}\left(T_w - T_{sat}\right)^3 \quad \text{Jens-Lottes.} \tag{2.121}$$

Chen's correlation uses the Forster-Zuber formulation of NB [61]. The heat transfer coefficient is calculated as:

$$h_{NB} = 0.00122\left(\frac{k_l^{0.79} c_{p,l}^{0.45} \rho_l^{0.49}}{\sigma^{0.5} \mu_l^{0.29} h_{fg}^{0.24} \rho_g^{0.49}}\right)^{0.8} \left(T_w - T_{sat}\right)^{0.4} \left[p(T_w) - p(T_{sat})\right]^{0.75} S \text{ ,} \tag{2.122}$$

in which:

$$p(T_w) = p_{sat}(T_w), \; S = \frac{1}{1 + 2.53 \cdot 10^{-6} \, \mathrm{Re}_*^{1.17}} \quad \text{and} \tag{2.123}$$

$$\mathrm{Re}_*^{1.17} = \left(\frac{G(1-x)D_h}{\mu_l}\right) F^{1.25} . \tag{2.124}$$

For the SaNB the bulk temperature is assumed to be equal to the saturated one.

2.5.5.4 Subcooled nucleate boiling

The SCB regime is intermediated and metastable heat transfer regime that occurs when the small bubbles are initially generated close to the heated wall. ESCOT adopts Collier's approach in the heat partition [62]. The force convection (*fc*) will only concern the liquid while the NB will only concern the bubble. Thus:

$$q''=h_{fc}\left(T_w-T_l\right)+\left(1-F_{gam}\right)h_{NB}\left(T_w-T_{sat}\right). \tag{2.125}$$

Both terms are calculated according to the equations provided in section 2.5.5.3 (in the case of Forster-Zuber $F = 1, x = 0$). The additional term multiplying the NB heat transfer coefficient considers the re-condensation effect. Part of the small bubbles in fact will condense back instantaneously. In particular:

$$F_{gam}=\max\begin{cases}\dfrac{h_{nb}\left(T_w-T_{sat}\right)-q''_{cond}}{h_{nb}\left(T_w-T_{sat}\right)}F_{SCB}\\ 0.01\end{cases}, \tag{2.126}$$

with:

$$F_{SCB}=\begin{cases}1.0\\ \max\begin{cases}\dfrac{h_{fg}}{h_{fg}+\left(h_{l,sat}-h_l\right)\dfrac{\rho_{l,sat}}{\rho_{v,sat}}}\\ 0.01\end{cases}\end{cases} \tag{2.127}$$

and the condensation heat transfer is defined as:

$$q''_{cond}=\max\begin{cases}q''_{HN}-h_{fc}\left(T_w-T_l\right)\\ 0\end{cases}. \tag{2.128}$$

The term contained inside Eq. (2.128) is taken from the Hancox-Nicoll correlation [63]:

$$q''_{HN} = 0.4 Re^{0.662} Pr\left(T_{sat} - T_l\right). \qquad (2.129)$$

For the solution of the conduction equation, the bulk temperature is required. In the SCB regime, the bulk temperature cannot be defined. However, following the definition of Collier's heat partition given in Eq. (2.125), it is possible to define:

$$T_{bulk} = \frac{h_{fc}}{h_{fc} + (1 - F_{gam})h_{nb}} T_l + \frac{\left(1 - F_{gam}\right)h_{nb}}{h_{fc} + \left(1 - F_{gam}\right)h_{nb}} T_{sat}\,. \qquad (2.130)$$

2.6 Solution of the conduction equation

ESCOT includes the capabilities for computing the temperature distribution of fuel rods. The heat balance equation for solids is defined as:

$$\frac{\partial\left[e\left(\vec{r},t\right)\right]}{\partial t} + \nabla\cdot\left(\vec{q}''\left(\vec{r},t\right)\right) = q'''\left(\vec{r},t\right), \qquad (2.131)$$

the energy term can be calculated as the product of three main terms:

$$e\left(\vec{r},t\right) = \rho\left(\vec{r},T\left(\vec{r},t\right)\right) c_p\left(\vec{r},T\left(\vec{r},t\right)\right) T\left(\vec{r},t\right), \qquad (2.132)$$

while the convection terms can be substituted with the Fourier's wall conduction law:

$$\vec{q}'' = -k\left(\vec{r},T\left(\vec{r},t\right)\right)\nabla\left(T\left(\vec{r},t\right)\right). \qquad (2.133)$$

The notation can be simplified removing the dependence from the density, c_p and the thermal conductivity:

$$\rho = \rho\left(\vec{r},T\left(\vec{r},t\right)\right),\ c_p = c_p\left(\vec{r},T\left(\vec{r},t\right)\right) \text{ and } k = k\left(\vec{r},T\left(\vec{r},t\right)\right) \qquad (2.134)$$

using Eqs. (2.132), (2.133) and (2.134) into Eq. (2.131):

$$\frac{\partial\left(\rho c_p T\right)}{\partial t} = \frac{\partial \rho}{\partial t} c_p T + \rho \frac{\partial c_p}{\partial t} T + \rho c_p \frac{\partial T}{\partial t} = \nabla\cdot\left(k \nabla T\left(\vec{r},t\right)\right) + q'''\left(\vec{r},t\right), \qquad (2.135)$$

together with its boundary conditions:

$$T\left(\vec{r},t_0\right)=T^*\left(\vec{r}\right)$$
$$\nabla T\left(\vec{r},t\right)=\nabla T\left(\vec{r}_0,t\right) \div T\left(\vec{r}_1,t\right)=T\left(\vec{r}_1,t\right), \qquad (2.136)$$

and by applying the chain rule for partial derivatives to express the time dependency of the density (ρ) and of expansion coefficient at constant pressure (c_p) in temperature:

$$\frac{\partial \rho}{\partial t}=\frac{\partial \rho}{\partial T}\frac{\partial T}{\partial t},\ \frac{\partial c_p}{\partial t}=\frac{\partial c_p}{\partial T}\frac{\partial T}{\partial t}$$
$$\frac{\partial\left(\rho c_p T\right)}{\partial t}=\left(\frac{\partial \rho}{\partial T}c_p T+\rho\frac{\partial c_p}{\partial T}T+\rho c_p\right)\frac{\partial T}{\partial t}, \qquad (2.137)$$

the final equation heat balance equation can be formulated as:

$$\left(\frac{\partial \rho}{\partial T}c_p T\left(\vec{r},t\right)+\rho\frac{\partial c_p}{\partial T}T\left(\vec{r},t\right)+\rho c_p\right)\frac{\partial T\left(\vec{r},t\right)}{\partial t}=\nabla\cdot\left(k\nabla T\left(\vec{r},t\right)\right)+q'''\left(\vec{r},t\right). \qquad (2.138)$$

The two following sections describe the employed equations of state used in the ESCOT source file and the adopted strategy for the solution algorithm.

2.6.1 Equations of state for the solid

This section summarizes the empirical correlations used for calculating the thermal conductivities and c_p of fuel and clad and the gap conductance. ESCOT uses the correlations taken from different fuel performance codes such as FRAPCON [64], BISON [65]. Moreover, the density of fuel and clad are considered constant in time thus: $\frac{\partial \rho}{\partial t}=0$.

2.6.1.1 Fuel equations of state

The fuel thermal conductivity expressed in *W/mK* is given as follow:

$$k_{fuel,95}^{UO_2} = \begin{pmatrix} A + a \cdot gad + BT + f(bu) + \\ + \left[1 - 0.9\exp\left(-0.04bu\right)\right] g(bu)h(T) \end{pmatrix}^{-1} + \\ + \frac{E}{T^2}\exp\left(-\frac{F}{T}\right) , \tag{2.139}$$

where:

$$\begin{aligned} A &= 0.0452 \\ a &= 1.1599 \\ gad &= weight\ fraction\ of\ Gd \\ B &= 2.46 \cdot 10^{-4} \\ E &= 3.50 \cdot 10^{+9} \\ F &= 16,361.0 \\ f(bu) &= 0.00187 \cdot bu \\ g(bu) &= 0.038 \cdot bu^{0.28} \\ h(T) &= \frac{1}{1 + 396.0\exp\left(-\frac{Q}{T}\right)} \\ Q &= 6380.0 \end{aligned} \tag{2.140}$$

and the temperature is given in *K* and the burnup in *MWd/kg$_U$*.

Small modifications on Eq. (2.139) are applied to calculate the thermal conductivity of MOX fuel:

$$k_{fuel}^{MOX} = \begin{pmatrix} A(x) + a \cdot gad + B(x)T + \\ + f(bu) + \left[1 - 0.9\exp\left(-0.04bu\right)\right] g(bu)h(T) \end{pmatrix}^{-1} + \\ + \frac{E}{T^2}\exp\left(-\frac{F}{T}\right) , \tag{2.141}$$

where the coefficient *A* and *B* depend on the oxygen to metal ratio:

$$x = 2 - \eta,\ \eta = \frac{N_{O_2}}{N_{met}}, \tag{2.142}$$

$$\begin{aligned} A(x) &= 2.85x + 0.035 \\ B(x) &= (7.15x + 2.86)\cdot 10^{-4}. \end{aligned} \tag{2.143}$$

c_p is instead calculated as follows [66]:

$$c_p(T) = \frac{K_1\theta^2 \exp\left(\frac{\theta}{T}\right)}{T^2\left[\exp\left(\frac{\theta}{T}\right) - 1\right]^2} + K_2 T + \frac{\eta}{2}\frac{K_3 E_D}{RT^2}\exp\left(-\frac{E_D}{RT}\right), \tag{2.144}$$

where:

$$\begin{aligned} R &= 8.3143\ \frac{J}{mol\ K} \\ \theta &= 535.285\ K \\ K_1 &= 296.7\ \frac{J}{kg\ K} \\ K_2 &= 2.43\cdot 10^{-2}\ \frac{J}{kg\ K}. \\ K_3 &= 8.745\cdot 10^{7}\ \frac{J}{kg} \\ E_D &= 1.577\cdot 10^{5}\ \frac{J}{mol} \end{aligned} \tag{2.145}$$

The derivative term is directly coded inside the source code as:

$$\begin{aligned} \frac{dc_p(T)}{dT} = {} & \frac{K_1\theta^2 \exp\left(\frac{\theta}{T}\right)\left\{\theta\left[1 + \exp\left(\frac{\theta}{T}\right)\right] + 2T\left[1 - \exp\left(\frac{\theta}{T}\right)\right]\right\}}{T^4\left[\exp\left(\frac{\theta}{T}\right) - 1\right]^3} + \\ & + K_2 + \frac{OM}{2}\frac{K_3 E_D\left(E_D - 2RT\right)}{R^2T^4}\exp\left(-\frac{E_D}{RT}\right) \end{aligned}. \tag{2.146}$$

ESCOT uses a constant value for the fuel density, $\rho_{fuel} = 10{,}412 kg/m^3$.

2.6.1.2 Clad equations of state

The clad thermal conductivity is calculated as a polynomial of order 3:

$$\begin{gathered} k_{clad} = A + BT - CT^2 + DT^3 \\ A = 7.51 \\ B = 2.09 \cdot 10^{-2} \\ C = 1.45 \cdot 10^{-5} \\ D = 7.67 \cdot 10^{-9} \end{gathered} , \tag{2.147}$$

while c_p uses a linear correlation with temperature [66]:

$$\begin{gathered} c_p = A + BT \\ A = 252.54 \\ B = 1.1474 \cdot 10^{-1} \end{gathered} \quad \text{and} \tag{2.148}$$

a constant derivative:

$$\frac{\partial c_p}{\partial t} = B .$$

ESCOT uses a constant value for the clad density, $\rho_{clad} = 6{,}600 kg/m^3$.

2.6.1.3 Gap conductance

The temperature dependent gap conductance is taken from the BISON code [65]. The gap heat transfer is modeled using the relation:

$$h_{gap} = h_{gas} + h_{rad} + h_{cont} , \tag{2.149}$$

where three main contributions are present: the gas conduction, the fuel-clad radiation and the pellet-clad contact interaction.

The gas contribution can be calculated as:

$$h_{gas}=\frac{k_{gas}}{\delta_{eff}}=\frac{k_{gas}(T)}{C_r\left(r_{fo}+r_{ci}\right)+d_g+\left(g_1+g_2\right)}, \tag{2.150}$$

where the numerator represents the gas thermal conductivity calculated as:

$$k_{gas}\left(T\right)=k_{gas}\left(T,\mathrm{x}_i\right)=\prod_i\left(k_{i,gas}(T)\right)^{x_i} \text{ and} \tag{2.151}$$

$$x_i=Molar\ Fraction$$

$$k_{i,gas}(T)=AT^{0.79}\cdot 10^{-4}=\begin{cases}15.80 & Helium\\ 1.97 & Argon\\ 1.15 & Krypton\\ 0.72 & Xenon\end{cases}, \tag{2.152}$$

while the denominator:

$$\begin{gathered}
d_g=r_0\ln\left(\frac{r_{ci}}{r_{fo}}\right)\approx r_{ci}-r_{fo}\\
g_1+g_2=A_{Lanning}\frac{\left(2-a_{mix}\right)}{a_{mix}}\frac{k_{gas}(T)\sqrt{T_{gap}}}{p_{gap}}\left(\sum_i\frac{x_i}{mol_i}\right)^{-0.5}\\
A_{Lanning}=0.375\left(\frac{8\pi}{9R}\right)^{0.5}\approx 0.2174\\
a_{mix}=a_{He}+\frac{\left(a_{Xe}-a_{He}\right)\left(M_{mix}-M_{He}\right)}{\left(M_{Xe}-M_{He}\right)}\\
a_{He}=0.425-2.3T_{gap}\cdot 10^{-4}\\
a_{Xe}=0.749-2.5T_{gap}\cdot 10^{-4}\\
C_r=3.2\\
\left(\rho_{fo}+\rho_{ci}\right)=2.8\cdot 10^{-6}m\Rightarrow average\ roughness
\end{gathered}\ . \tag{2.153}$$

The radiation contribution is expressed by considering the emissivity of fuel and clad:

$$h_{rad}(T) = \frac{\sigma\left(T_{fo}^4 - T_{ci}^4\right)}{\left(\frac{1}{\varepsilon_f} + \frac{1}{\varepsilon_c} - 1\right)\left(T_{fo} - T_{ci}\right)} = \frac{\sigma\left(T_{fo}^2 + T_{ci}^2\right)\left(T_{fo} + T_{ci}\right)}{\left(\frac{1}{\varepsilon_f} + \frac{1}{\varepsilon_c} - 1\right)}, \qquad (2.154)$$

ESCOT uses the following parameters:

$$\begin{aligned} \sigma &= 5.67036713 \cdot 10^{-8}\left[\frac{W}{m^2K^4}\right] \\ \varepsilon_c &= 0.3 \\ \varepsilon_f &= 0.7856 + 1.5263 T_{fo} \cdot 10^{-5} \end{aligned} \quad . \qquad (2.155)$$

Finally, for the contact term ESCOT assumes it equal to zero.

2.6.2 Solution Strategy and Implementation

ESCOT has implemented two main conduction solvers for the solution of Eq. (2.138). The first one solves the conduction equation for steady-state problems, thus:

$$\nabla \cdot \left(k \nabla T\right) = q''' \qquad (2.156)$$

while the second one solves the transient conduction equation. For both cases the equation has been integrated in the finite volume, the continuity between fluid and wall has been established according to Eq. (2.112) and a simple interpolation to calculate the center line temperature has been employed. The geometrical integration only concerned the radial variable, namely within the same axial mesh the temperature is solved assuming cylindrical symmetry.

For the transient solver, an additional discretization is employed in order to consider of the time dependency. ESCOT employs a Crank-Nicholson discretization method to predict the time variation of the fuel temperature. Fig. 2.7 shows the geometrical discretization of the fuel pin cell.

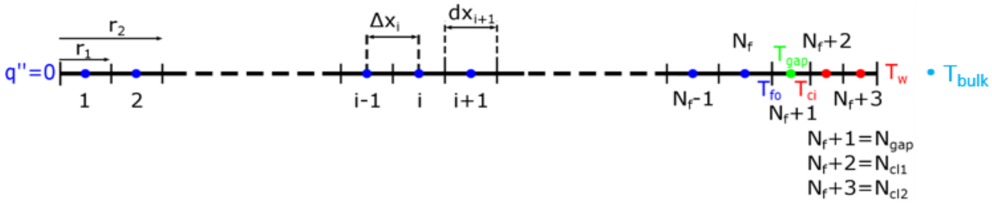

Fig. 2.7: radial discretization of the fuel pin for the solution of the conduction equation.

2.7 Critical Heat Flux

ESCOT cannot simulate post-critical heat flux conditions. To ensure that, two CHF models are implemented which will inform the user of crossing the ESCOT reliability limit. The first one is based on the CTF model [25] while the second one is based on the Groeneveld lookup tables [67]. The CTF scheme is presented inside Fig. 2.8.

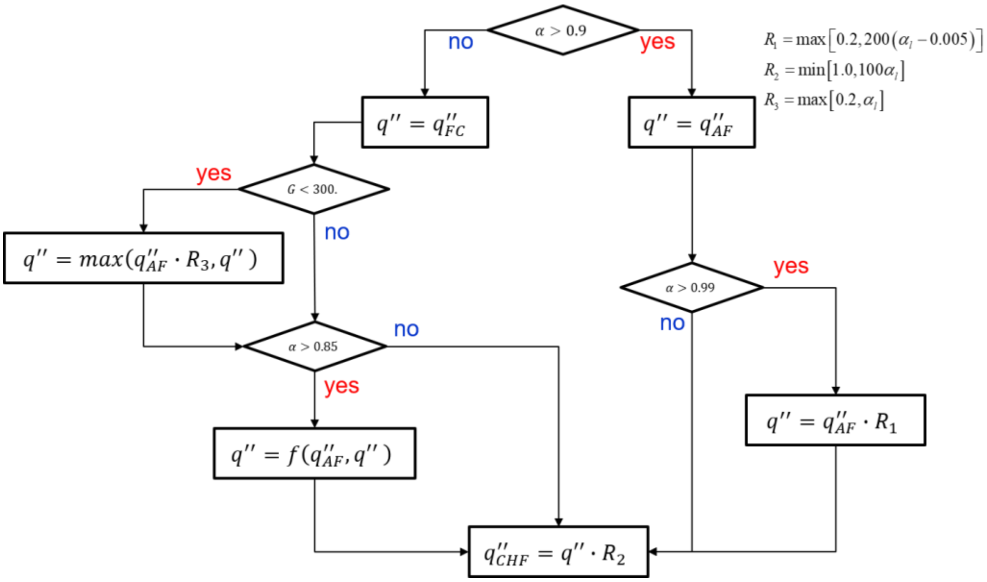

Fig. 2.8: critical heat flux scheme in the ESCOT code.

If the void fraction of the analyzed channel is smaller than 0.9, the first calculation of the CHF is performed according to the Biasi correlation [68]:

$$q_1'' = 2.764\cdot 10^7 \left(100D_h\right)^{-n} G^{-\frac{1}{6}}\left(1.468F\left(p\right)G^{-\frac{1}{6}} - x\right), \qquad (2.157)$$

$$q_2'' = 1.5048\cdot 10^7 \left(100D_h\right)^{-n} G^{-0.6} H\left(p\right)\left(1-x\right)$$

where:

$$F\left(p\right) = 0.7249 + 0.099p\exp\left(-0.032p\right)$$

$$H\left(p\right) = -1.159 + 0.149p\exp\left(-0.019p\right) + \frac{9p}{10+p^2} \quad \text{and} \qquad (2.158)$$

with the pressure given in *bar*. The code chooses the maximum of the two values unless the value of G is smaller than 300 $kg/(m^2s)$; in this case, only the first equation is used. In addition, if the condition on the mass flux is fulfilled, the CHF is calculated by choosing the maximum between the one given by Eq. (2.157) and the product between the factor R_3 and the annular flux critical heat flux given by Bjornard and Griffith [69]:

$$q_{AF}'' = 0.15\left(1-\alpha\right)h_{fg}\rho_g^{0.5}\left[g\sigma\left(\rho_f - \rho_g\right)\right]^{0.25} \quad \text{and} \qquad (2.159)$$

$$R_3 = \max\left(0.2, \alpha_l\right). \qquad (2.160)$$

After that, if the void fraction results bigger than 0.85, ESCOT ramps the CHF towards the annular flux film dryout as:

$$f\left(q'', q_{AF}''\right) = 20\left[q''\left(\alpha_l - 0.1\right) + q_{AF}''\left(0.15 - \alpha_l\right)\right]. \qquad (2.161)$$

Finally, the CHF is multiplied by the factor R_2:

$$R_2 = \min\left(1.0, 100\alpha_l\right). \qquad (2.162)$$

In the case of void fraction bigger than 0.9, CHF is calculated using Eq. (2.159) and in the case of almost full vapor conditions ($\alpha > 0.99$) an additional ramp R_1 is introduced:

$$R_1 = \max\left[0.2, 200\left(\alpha_l - 0.005\right)\right]. \tag{2.163}$$

2.8 Two phase validation of the ESCOT code

The validation and verification (V&V) phase of a code is fundamental to show what a code does and that the code works as advertised. Whereas verification tasks show that the mathematical equations are being solved correctly and were implemented in the code in a bug-free way, validation tasks demonstrate that the correct equations are being solved, resulting in a good agreement with experimental data. The comparison to experimental data is a necessary part of validation work.

The V&V process of the ESCOT code was begun by Lee [19] in his M.Sc. and completed subsequently [17], [19], [27]. For what concerns the validation process, the following benchmark problems have been simulated to validate ESCOT:

- Single phase unheated tests: CNEN 4*x*4 [70], WH 14*x*14 [71].
- Single phase heated tests: PNNL 2*x*6 [72].
- Two phase unheated tests: RPI air-water test [73].
- Two phase heated tests: GE 3*x*3 [74], PSBT Phase I, Exercise 2 [75].

All the performed tests are performed using the default input parameters unless differently specified and they are always accompanied by a comparison with experimental results and by code-to-code comparison with MATRA [23], CUPID [9] and/or CTF [25]. The entire validation process of the ESCOT code is detailed inside its V&V manual [76].

This manuscript contains only the validation results for the two phase flow conditions [27]. The following sections show the validation of two main phenomena, the turbulent mixing and void drift and the void distribution in bundle geometries.

2.8.1 RPI Air-water test

The intended purpose of this experiment was to investigate the fully developed two phase of distribution in a 2*x*2 rod array test section in order to furnish data for the validation of turbulent mixing and void drift by physically measuring the channel-wise outlet void fraction. The test facility includes a 914.4*mm* long unheated 2*x*2 rod bundle with an air-water mixture as the working fluid (see Fig. 2.9). With a bundle hydraulic diameter of 23.22*mm*, an *L/D* factor of 39 was calculated, leading to an expected fully-developed flow condition at the bundle outlet. Four 0.055*inch* thick 314 stainless steel tubes with 1.0*inch* outer diameter were used to simulate the fuel rods. The wall thickness insured a vibration-free environment during the experiment, and a lower tie plate provided support for the rods. No spacer grids were used in this experiment. Two different techniques were used to distribute the air into the bundle inlet, a sinter section and a mixing tee technique [73].

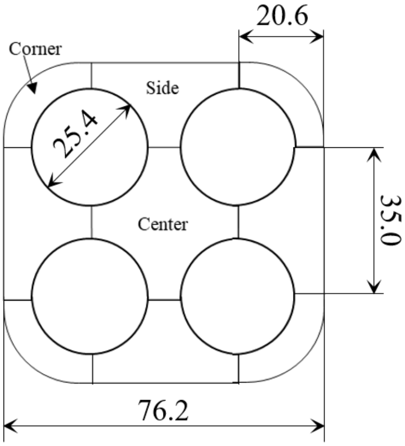

Fig. 2.9: scheme of the horizontal cross section of the RPI air-water test bundle.

The boundary conditions of these tests are provided inside Tab. 2.4. The ESCOT model consisted of 10 axial meshes and 9 channels. For this test, the Zuber and Findlay correlation for the void drift parameters have been used since the values of the inlet and outlet pressure are outside the range of validity of the Chexal-Lellouche one.

Tab. 2.4: boundary conditions for the RPI air-water validation test.

Case	v_{in} **[*m/s*]**	α_{in} **[%]**	**Inlet velocities [*m/s*]**		p_{in} **[Pa]**	p_{out} **[Pa]**
			Liquid	*Gas*		
1	0.451	20.4	0.569	0.984	142721.5	135821.5
2	0.451	32.8	0.674	1.344	146168.8	140598.8
3	0.451	46.1	0.840	1.906	156511.0	152106.0
4	0.903	23.6	1.185	1.399	208221.7	200843.4
5	0.903	37.5	1.448	1.956	232353.3	225.936.6
6	0.903	52.7	1.914	2.780	280616.6	274373.2

Fig. 2.10 shows the validation results. ESCOT matches the mixing tee experimental data better than the sinter section ones. Case 3 did not reach convergence. The activation of EVVD model shows a decrease of about 7 and 10% for the two different analyzed cases. Tab. 2.5 summarizes the results and provides a comparison with the CUPID code.

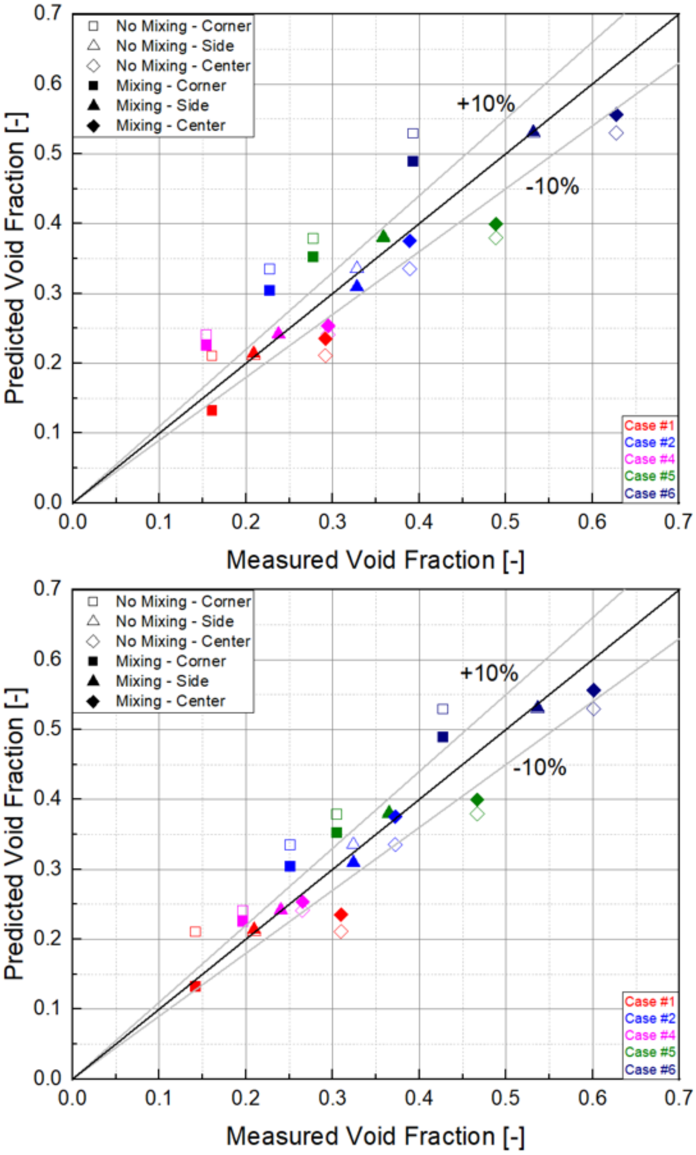

Fig. 2.10: validation results for RPI air-water test: Sinter section (*top*) and Mixing-tee (*bottom*).

Tab. 2.5: summary of the ESCOT validation results for RPI air-water test and comparison with CUPID.

Sinter Section		**No Mixing**			**Mixing**		
		Corner	Side	Center	Corner	Side	Center
ESCOT	Max [%]	57.11	5.85	27.54	47.32	6.21	19.25
	RMS [%]	42.80	2.94	20.10	31.83	4.02	14.42
CUPID	Max [%]	69.01	19.80	23.02	36.07	20.94	20.08
	RMS [%]	49.05	11.96	16.49	26.41	13.62	14.54
Mixing Tee		**No Mixing**			**Mixing**		
		Corner	Side	Center	Corner	Side	Center
ESCOT	Max [%]	49.47	4.03	31.78	21.79	4.49	23.97
	RMS [%]	32.70	2.50	18.33	15.66	3.03	13.09
CUPID	Max [%]	61.96	20.30	25.77	44.29	21.44	22.34
	RMS [%]	42.39	12.30	14.72	21.43	13.90	13.55

2.8.2 GE 3*x*3 test

Conducted at General Electrics in 1970, the GE 3*x*3 test is a classic experiment for assessing inter-subchannel mixing due to the fact that mass flux and quality measurements could be made for individual subchannel types at the outlet section. A 3*x*3 heated tube geometry was used in a BWR-like simulation with General Electric (GE) rods [74].

The radial and axial geometry of the bundle is shown in Fig. 2.11 with all the necessary sizes to simulate the test. The axial and radial power profiles were uniform for all of these test cases. The same bundle was used for all the tests. Bundle power, flow rate and inlet subcooling was varied between different experimental cases as shown in Tab. 2.6. Average pressure of the experiments was set to 6.9*MPa*, so for every case the outlet pressure for 6.848MPa. Subchannel measurements were taken to determine the specifics of coolant flow through the three different types of subchannels. The target parameters were the channel-wise outer mass fluxes and outer enthalpies (in the form of thermodynamic quality Eq. (2.4)). Six spacer grids were positioned at 50.8, 355.6, 660.4, 965.2, 1270.0 and 1574.8mm from the bottom of the heated length. For this specific analysis, ESCOT has employed localized form loss coefficients for corner, side and center (0.3360, 0.1629 and 0.1504).

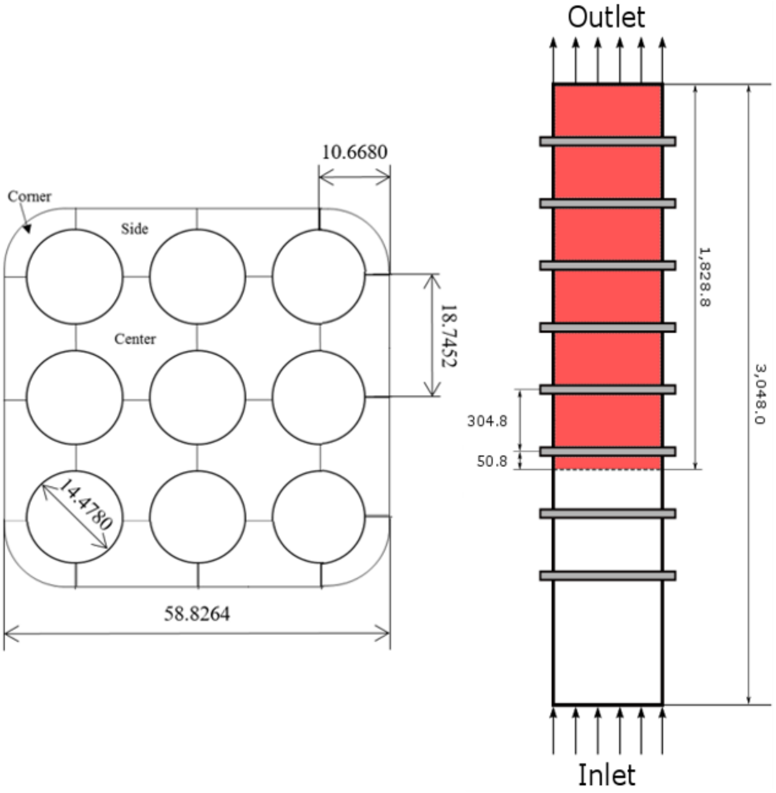

Fig. 2.11: radial and axial schemes of the GE 3x3 test section.

Tab. 2.6: boundary conditions for the GE 3*x*3 validation test.

Test Series	**Power [*kW*]**	**G [kg/m^{2}s]**	**Inlet subcooling [*kJ/kg*]**
2B2	532	718.80	914.35
2B3	532	725.58	1010.20
2B4	532	725.58	1140.30
2D1	1064	732.37	660.40
2D3	1064	732.37	974.20
2C1	532	1437.61	1130.40
2C2	532	1448.46	1181.80
2E1	1064	1464.73	931.70
2E2	1064	1464.73	1039.40
2E3	1064	1437.61	1197.00
2G1	1596	1451.17	739.30
2G2	1596	1464.73	823.40
2G3	1596	1451.17	924.00

The ESCOT model consisted of 72 equally-spaced axial meshes and 12 channels. For this test, the mixing factor was reduced to $\beta = 0.007$, the same value CTF uses for simulating this test [77].

Results of this validation test are shown in Fig. 2.12 and summarized in the Tab. 2.7 and Tab. 2.8. It turned out that ESCOT and CTF have comparable error behaviors in the prediction of the target parameters.

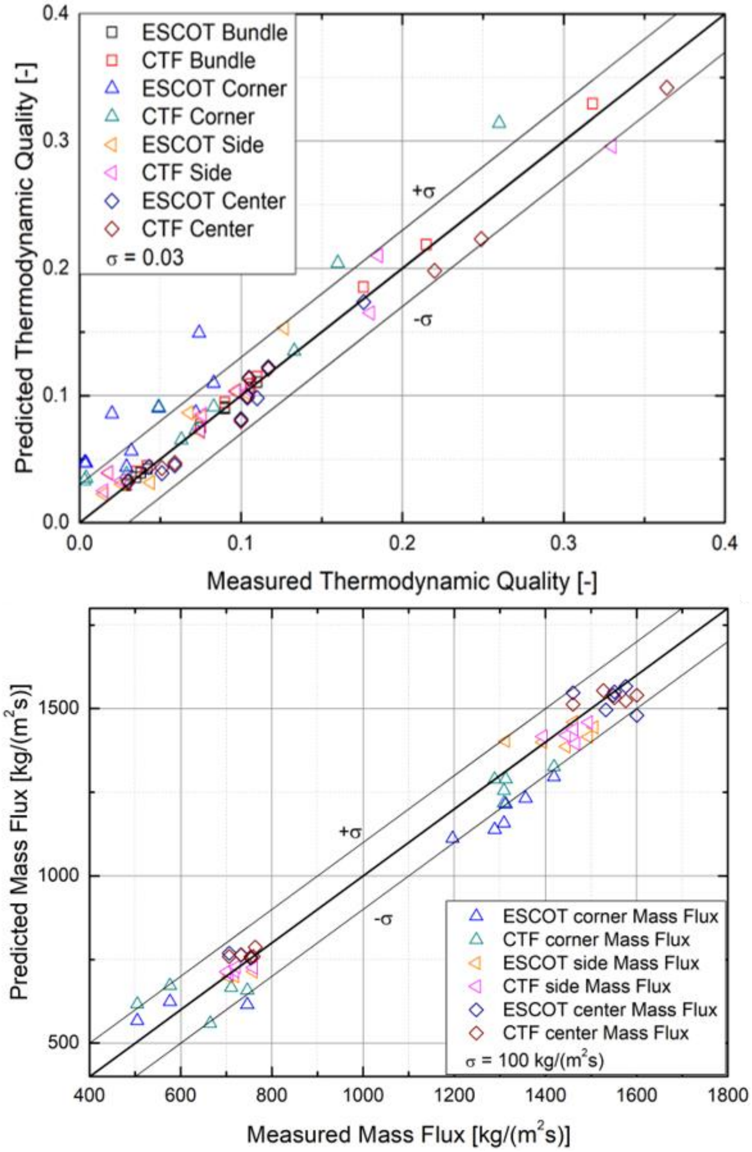

Fig. 2.12: results of the GE 3*x*3 validation test for both ESCOT and CTF: thermodynamic quality (*top*) and mass flux (*bottom*).

Tab. 2.7: summary of the GE 3*x*3 test results of the thermodynamic quality for ESCOT and CTF.

		Thermodynamic Quality			
		Bundle	Corner	Side	Center
ESCOT	Max.	0.001	0.066	0.022	0.009
	RMS	0.001	0.036	0.011	0.010
CTF	Max.	0.011	0.054	0.034	0.026
	RMS	0.006	0.029	0.016	0.015

Tab. 2.8: summary of the GE 3*x*3 results test results of the mixture mass flux for ESCOT and CTF.

		Mixture Mass Flux		
		Corner	Side	Center
ESCOT	Max [%]	17.62	6.88	8.73
	RMS [%]	10.87	4.14	4.64
CTF	Max [%]	22.11	4.80	7.37
	RMS [%]	11.45	2.48	3.53

2.8.3 PSBT Phase I, Exercise 2

The PWR Subchannel and Bundle Test (PSBT) experiments include both single channel and rod bundle geometries as well as steady-state and transient operating conditions [75]. PSBT specifications organize the experiments into two phases with subcategories called exercises.

- Phase I: Void Distribution Benchmark
    - Exercise 1: Steady-state single subchannel benchmark.
    - Exercise 2: Steady-state bundle benchmark.
    - Exercise 3: Transient bundle benchmark.
    - Exercise 4: Pressure drop benchmark.
- Phase II: DNB Benchmark
    - Exercise 1: Steady-state fluid temperature benchmark.
    - Exercise 2: Steady-state DNB benchmark.
    - Exercise 3: Transient DNB benchmark.

Tests from Phase I, Exercise 2 were used to validate ESCOT towards the void distribution in bundle geometries by measuring the average void fraction inside the four central subchannel at three different axial levels. Inside this Exercise the selected tests were Test Series 5, 6 and 7. The main differences between the test series are the axial power shape, constant for test series 5 and cosine-shaped for test series 6 and 7, and the radial power distribution. Three different types of spacer grids are used in the experiments: Mixing Vane (MV), No Mixing Vane (NMV) and Simple Spacer (SS). The form losses are equal respectively to 1.0, 0.7 and 0.4 and the thicknesses to 55.88, 38.10 and 12.80*mm*. Fig. 2.13 and Tab. 2.9 provide information about the test section and each test series.

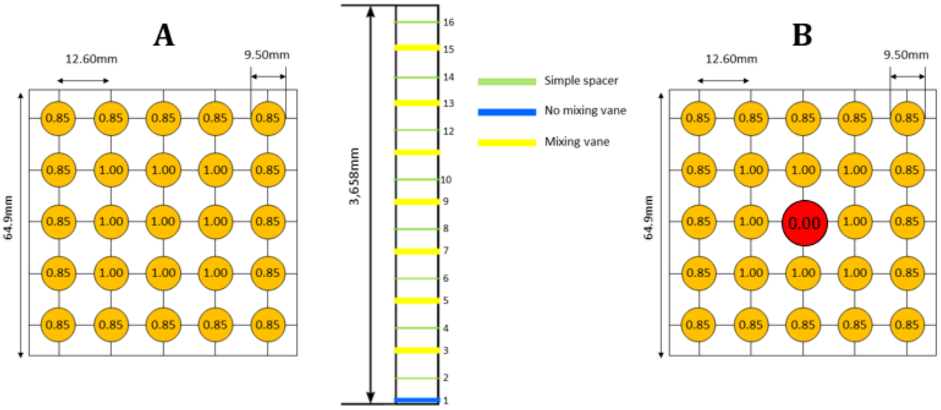

Fig. 2.13: radial and axial scheme of the PSBT Phase I - Exercise 2 test section.

Tab. 2.9: information of each test series of the PSBT Phase I, Exercise 2.

Item	**Data**		
Test Series	5	6	7
Radial Power	A	A	B
Axial Power	Uniform	Cosine	Cosine
# of heated Rods	25	25	24

Several test conditions with pressure changing between 4.9*MPa* and 16.5*MPa*, average power between 1.0 and 3.5*MW*, inlet temperature between 150 and 310*℃* and inlet mass flux between 2 and 11$kg/(m^2s)$. The boundary conditions are provided in detail in the V&V manual of ESCOT [76].

The ESCOT model consisted of 42 unstructured axial meshes and 36 channels for test series 5 and 6. For test series7 the number of axial unstructured meshes was increased up to 79.

The results of the three series are shown in Fig. 2.14. In general, a small over prediction at low void fraction is present both for ESCOT and CTF. Tab. 2.10 summarizes the errors against the experimental data for ESCOT and CTF.

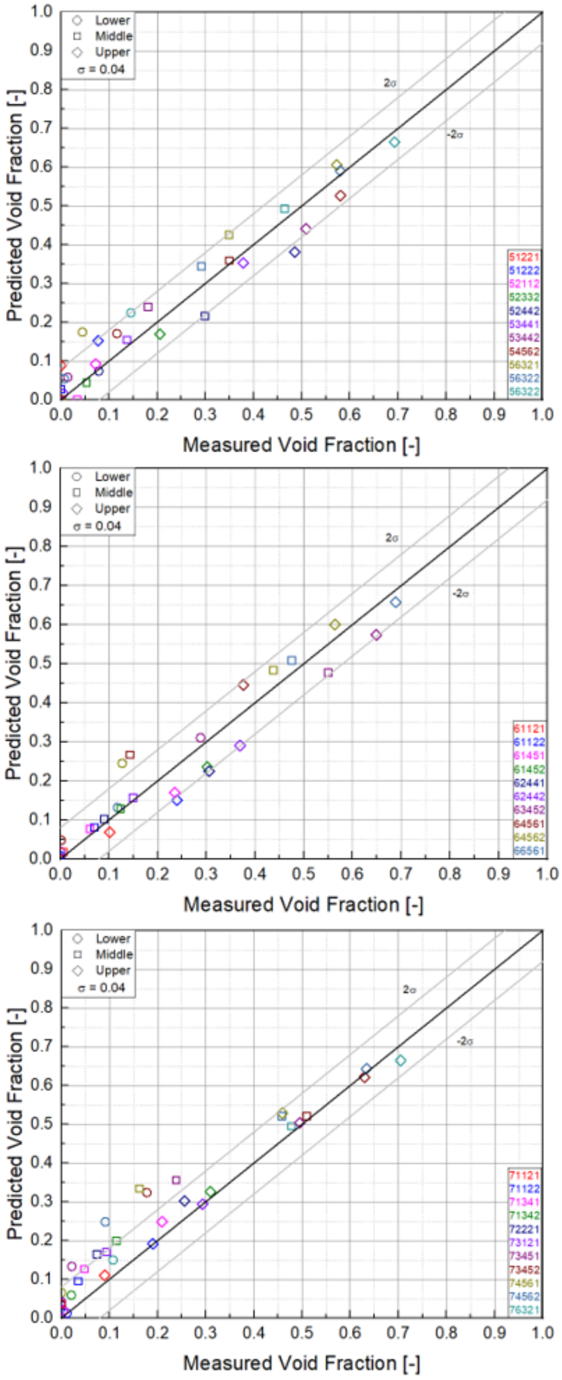

Fig. 2.14: results of the test series 5 (*top*), 6 (*middle*) and 7 (*bottom*) for PSBT Phase I, Exercise 2.

Tab. 2.10: summary of the errors for the PSBT Phase I, Exercise 2 for ESCOT and CTF.

		Series 5			
		Lower	Middle	Upper	Total
ESCOT	Max.	0.130	0.083	0.105	-
	RMS	0.052	0.045	0.057	0.052
CTF	Max.	0.109	0.106	0.113	-
	RMS	0.036	0.045	0.069	0.051
		Series 6			
		Lower	Middle	Upper	Total
ESCOT	Max.	0.118	0.124	0.157	-
	RMS	0.042	0.049	0.066	0.053
CTF	Max.	0.185	0.073	0.092	-
	RMS	0.065	0.046	0.057	0.057
		Series 7			
		Lower	Middle	Upper	Total
ESCOT	Max.	0.157	0.172	0.070	-
	RMS	0.079	0.085	0.032	0.069
CTF	Max.	0.081	0.137	0.077	-
	RMS	0.032	0.072	0.042	0.052

2.9 Parallelization Scheme

The initial version of ESCOT was hybrid parallelized, employing MPI for axial domain decomposition and OpenMP for the parallel loops, but this scheme is not the optimum one for a code which aims at solving T/H of nuclear reactor cores. Lee switched the parallel scheme to full MPI [17], [26]. Assembly or subassembly-wise domain decomposition shows satisfactory parallel performance of a subchannel code. Thus, ESCOT adopts the assembly-wise radial domain decomposition for MPI parallelization as shown in Fig. 2.15. Furthermore, the domain of ESCOT can be axially decomposed up to the number of axial planes. The radial-only decomposition forces the users to have a rigid and specific number of processors, which is one processor per assembly. The axial domain decomposition has more flexible choice for the number of processors. Therefore, thousands of processors are available for the parallel execution when both radial and axial domain decomposition are combined into a bidirectional decomposition which combines both schemes simultaneously. Fig. 2.16 shows an example of the applied parallelization topology applied in the ESCOT code. To solve the pressure correction and momentum equation the ghost cell approach has been fully implemented [26].

The full description, parallel performances and validation of the bidirectional domain decomposition are fully described in Lee Ph.D. thesis [17] and in here [26].

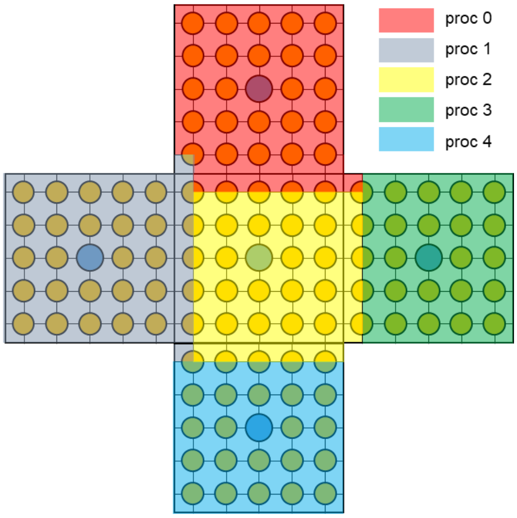

Fig. 2.15: example of assembly-wise domain decomposition for scalar variables.

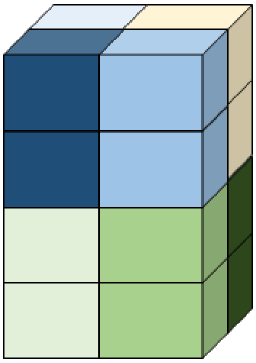

Fig. 2.16: example of bidirectional domain decomposition.

Chapter 3. Analysis of Steady-state Neutronics-Thermal/Hydraulics Coupled Calculations

The simulation of the entire core of light water reactors (LWR) with a realistic representation of the fuel constituents is now possible in a practical time span owing to the continued enhancements of the computing power and of the numerical methods. In DWCC, the integrated simulation of neutronics and T/H is essential to incorporate properly the thermal feedback effects. The primary solution of a neutronics-T/H coupled problem is the power distribution determined along with the distributions of the temperature, density, velocity and pressure of the coolant as well as the fuel temperature profiles. In order to resolve the thermal feedback effects, which induce nonlinear changes in the coefficients of the neutron transport equation, namely, the macroscopic cross sections, alternating calculations of the neutronics and T/H problems are carried out which can be regarded as a fixed-point iteration $\boldsymbol{x}^{(k+1)} = G(\boldsymbol{x}^{(k+1)})$. The traditional fixed-point solution approach was to repeat the alternating calculation in which the field equations are solved sequentially. For the enhancement of parallel computing efficiency, the tandem solution approach in which both field equations are solved simultaneously on different processors was also employed [8]. The former is regarded as the nonlinear Gauss-Seidel (GS) approach while the latter is the nonlinear Jacobi approach. The implementation of these two approaches is quite easy since it does not require any modification of the two solvers once each field information is exchanged through either an interface or a wrapper code. However, these two methods do not provide either unconditional stability and/or optimized convergence as noted in earlier works, see [78]. In general, a palliative and easy solution adopted for multiphysics calculations is the application of a smoothing factor ω (between 0.3 and 0.6):

$$\boldsymbol{x}^{(k+1)} = \left(1-\omega\right)\boldsymbol{x}^{(k+1)} + \omega\boldsymbol{x}^{(k)}. \tag{3.1}$$

Unfortunately, the choice of these factors results problem and user dependent. In this regard AA has the potential to remove the user and problem dependency in the choice of smoothing factors. In fact, AA-1 is essentially equivalent to a more sophisticated smoothing technique in which ω is calculated according to the AA algorithm.

Lee, in his Ph.D. dissertation [17], extended the use of the Anderson Acceleration [16] to full core problems and he concluded with four important outcomes:

- The sequential coupling scheme will always have a lower number of FPI than a tandem one because the tandem scheme can be almost fully decoupled into two separate sequential schemes,
- the tandem approach is less performant than the sequential one if the load balance of the coupled codes is not good enough,
- the application of AA improves the convergence and robustness of neutronics-T/H coupled problems (both sequential and tandem), and
- the solution of the accelerated and non-accelerated problems shows the same exact solution.

The fundamental idea of AA is to express the current solution during the FPI as a linear combination of the previous solutions, the coefficients of which are determined such that a properly defined residual is minimized. However, the main mathematical and physical reason why the AA improves the convergence of steady-state coupled analyses was not either discovered nor investigated. In this regard, a deep analysis was started to find the source of improvements. Poor convergence is some time due to the oscillatory behavior of the local solution around its converged value. This behavior can be originated from the overshooting effect that occurs when, during an iteration, the estimate of the solution at a point exceeds the reference solution [79], [80]. This behavior of the FPI is evident if the OPR1000 model core problem is solved by the nTRACER with its simple T/H module. The convergence of the local fission source to a flat source region (FSR) obtained at 4 different locations in the core is shown in Fig. 3.1. The four points represent different axial positions in a central assembly. It appears clearly the oscillatory behavior around the true solution regardless of the position. This oscillatory behavior, caused by overshooting, deteriorates the convergence of FPI scheme.

The overshooting effect can be also physically described by interpreting the evolution of the local fission source in Fig. 3.1.

- At iteration 4, the calculated ψ for top left FSR is bigger than the reference value. This high value induces an increase of the fuel temperature.
- The higher value of fuel temperature triggers a higher Doppler effect and a consequent decrease in the prediction of ψ at iteration 5.
- The value of ψ at iteration 5 induces a decrease of the fuel temperature which triggers a lower Doppler effect and a consequent increase in the prediction of ψ at iteration 6.
- The loop then restarts from the initial statement.

In this way, the combination of application of a Picard iteration algorithm and Doppler effect are the main reasons of poor robustness of coupled neutronics-T/H FPI based systems.

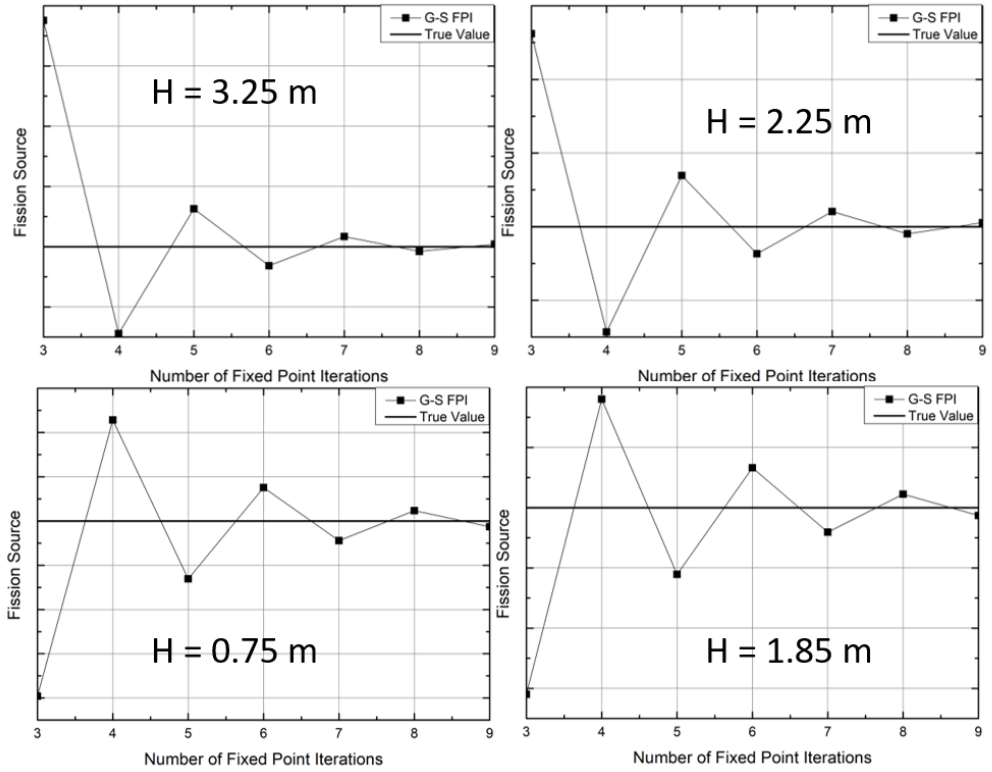

Fig. 3.1: oscillatory convergence of local fission source around the true solution at four different locations of the OPR1000 model core.

The following section describes the coupling system nTRACER/ESCOT in the case of sequential coupling since Lee showed that tandem approach merely wastes time [17] while section 3.2 presents the AA algorithm and its implementation. The analysis of the calculation results is displayed in section 3.3.

3.1 nTRACER/ESCOT coupled system

The two sets of governing equations are nonlinearly coupled and their decoupling is obtained by a modification of the GS-FPI scheme for two field variables as Fig. 3.2 shows.

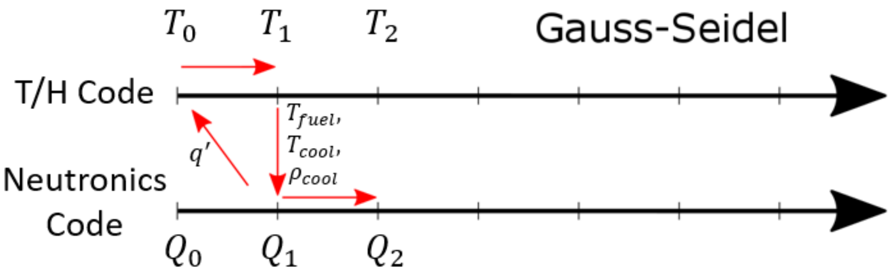

Fig. 3.2: Gauss-Seidel/sequential approach for the coupling scheme of neutronics-T/H.

Since the fuel temperature calculation can be further decoupled from the flow problem, there are in fact three main solvers in this solution scheme as:

- neutronics solver which determines the flux field, $\Phi = g_1\left(\rho_{cool}, T_{cool}, T_{fuel}\right)$,
- T/H solver which computes the coolant temperature and density fields, $\left[\rho_{cool}, T_{cool}\right] = g_2\left(q'''\left(\Phi\right)\right)$, and
- solid heat conduction solver which determines the fuel temperature field with the updated coolant temperature, $T_{fuel} = g_3\left(T_{cool}, q'''\left(\Phi\right)\right)$.

In the case of the Gauss-Seidel scheme, the solution vector does not contain the power since it is immediately used to estimate the T/H variables, namely:

$$\boldsymbol{x}_{GS}^{(k+1)}=\begin{bmatrix}\rho_{cool}^{(k+1)},T_{cool}^{(k+1)}\\ T_{fuel}^{(k+1)}\end{bmatrix}=\begin{bmatrix}g_2\left(q'''\left(g_1\left(\rho_{cool}^{(k)},T_{cool}^{(k)},T_{fuel}^{(k)}\right)\right)\right)\\ g_3\left(T_{cool}^{(k+1)},q'''\left(g_1\left(\rho_{cool}^{(k)},T_{cool}^{(k)},T_{fuel}^{(k)}\right)\right)\right)\end{bmatrix}. \tag{3.2}$$

This general scheme has been employed in the nTRACER code [29]. nTRACER is a DWCC code which employs the planar MOC solution based CMFD formulation in solving 3D neutron transport problems retaining subpin-level heterogeneity. For the axial solution, a simplified P_N kernel is used. nTRACER is highly parallelized with a hybrid approach using both MPI and OpenMP under the basic framework of axial domain decomposition [2]. nTRACER has its own simple T/H solver which solves the following steady-state 1D T/H equations for a closed flow channel at the level of pin or assembly and neglecting the pressure drop along the channel:

$$\begin{aligned}&\frac{\partial\rho(z)v(z)}{\partial z}=0\ \Rightarrow \rho(z)v(z)=const=\dot{m}_0\\ &\frac{\partial\rho(z)v(z)h(z)}{\partial z}=\cancel{\frac{\partial\left(\rho(z)v(z)\right)}{\partial z}}h(z)+\dot{m}_0\frac{\partial h(z)}{\partial z}=q'\,.\\ &\nabla\cdot\left(k\nabla T\right)+q'''=0\end{aligned} \tag{3.3}$$

The Picard based calculation flow of the neutronics and the T/H problems are depicted in Fig. 3.3. After the CMFD calculation, the T/H module is executed to provide the new distributions of ρ_{cool}, T_{cool}, T_{fuel} which are then used to update the microscopic and macroscopic cross sections. The planar MOC calculations are performed with the new macroscopic cross sections. Note that the macroscopic cross sections are given ringwise within a fuel pellet, that are determined properly with the updated fuel temperature profiles. To increase the fidelity of nTRACER analyses, the improvement of the T/H solution module was necessary. Thus, nTRACER and ESCOT have been coupled.

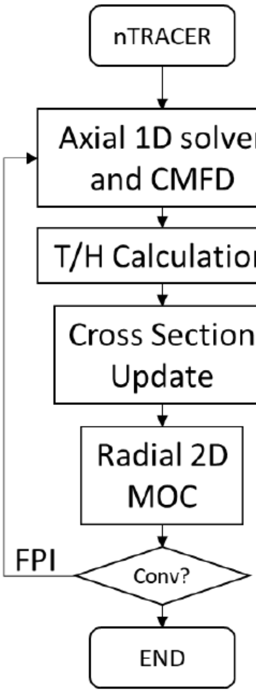

Fig. 3.3: overall calculation flow in nTRACER.

nTRACER and ESCOT have different parallelization schemes, in order to use both codes in their optimum parallel scheme, a wrapping system was necessary. The wrapper code (parent process) uses the MPI capability of spawning two child processes and manages the exchange of information between the two codes by creating three sub-communicators: two parent-child communicators and one child 1 – child 2 inter-communicator. Fig. 3.4 schematizes the system. First, the parent process initializes nTRACER and ESCOT; then, the nTRACER code starts its calculation according to the flowchart presented inside Fig. 3.3 while the ESCOT code stands by. When the neutronics simulation reaches the T/H calculation point, nTRACER sends directly the power and burnup to ESCOT through the inter-communicator and waits in standby for the T/H variables. With the updated power

ESCOT proceeds and calculates the T/H fields; once ESCOT has converged, the new distributions of ρ_{cool}, T_{cool}, T_{fuel} are sent to the wrapper which reorders them and sends them back to nTRACER.

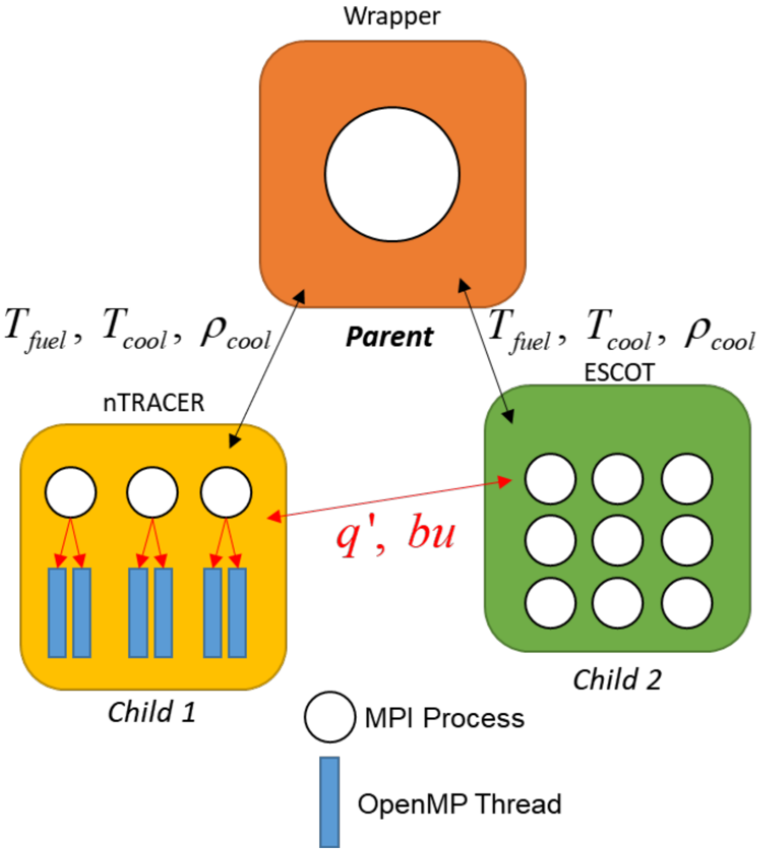

Fig. 3.4: nTRACER and ESCOT wrapping system for running both codes at full performances.

In the ESCOT standalone calculation, the convergence is checked through the use of four parameters: the mass and energy balances (< 0.02%), and the change of stored mass and stored energy between two time-steps (< 0.1%) [38]. Those conditions must be all met at the same time. In the coupled execution of nTRACER/ESCOT instead, it is not necessary to fully converge the ESCOT code at each FPI. In this regard, an additional ESCOT convergence criterion based on the reduction ratio of the stored mass is introduced as:

$$\frac{\Delta M^{(n)}}{\Delta M^{(0)}} < 0.02 . \tag{3.4}$$

In general, the ESCOT convergence behavior for coupled simulations follows Eq. (3.4) for the initial FPIs (3 to 4) while for the next iterations the convergence is reached according to the standalone rules.

3.2 Anderson Acceleration

Originally, Anderson proposed this acceleration method to solve coupled sets of singular, nonlinear integral equations related to the kinetic theory of gases [16]. Subsequently, Fang et al. [81] and Walker et al. [82] realized that the same numerical method could be used to accelerate the convergence of nonlinear Picard iterations. The idea of the method is to approximate the solution at the $(k + 1)^{th}$ iteration as a linear combination obtained from a proper number m of previous iterations. The coefficients of the linear combination representing the solution $\boldsymbol{x}^{(k+1)}$ are calculated by minimizing the square norm of the linear combination of the previous residual vectors $\boldsymbol{f}$ as described in Algorithm 3.1. As already mentioned, the index m represents the number of previous solutions to be used in the linear combination and specifies the order of the algorithm denoted by Anderson Acceleration-m (AA-m). The original algorithm contains a damping factor β which has been here taken equal to 1.

Non-truncated AA for linear problems is essentially equivalent to the Generalized Minimum Residual Method (GMRES) but it is not a good substitute [82], [83]. In some way, AA can be seen as an extension of GMRES to complex nonlinear problems.

The following sections describe the algorithm, its derivation and the implementation in the nTRACER code.

Algorithm 3.1: Anderson Acceleration method, general algorithm.

```
Algorithm. Anderson Acceleration
Given $\boldsymbol{x}(0)$ and $m \geq 1$,
set $\boldsymbol{x}(1) = g(\boldsymbol{x}(0))$.
while (conv)
    Set $m_k = \min(m,k)$ and
    calculate $g(\boldsymbol{x}^{(k)})$.
    Set $\boldsymbol{f}^{(k)} = g(\boldsymbol{x}^{(k)}) - \boldsymbol{x}^{(k)}$;
    set $F^{(k)} = [\boldsymbol{f}^{(k-m_k)}, \ldots, \boldsymbol{f}^{(k)}]$.
    Determine $\boldsymbol{\alpha}^{(k)} = \left[\alpha_0^{(k)}, \ldots, \alpha_{m_k}^{(k)}\right]^T$ which solves:
        $\min_{\boldsymbol{\alpha}^{(k)}} \|F^{(k)}\boldsymbol{\alpha}^{(k)}\|_2$, with $\sum_{i=0}^{m_k} \alpha_i^{(k)} = 1$.
    Calculate:
        $\boldsymbol{x}^{(k+1)} = (1-\beta)\sum_{i=0}^{m_k} \alpha_i^{(k)} \boldsymbol{x}^{(k-m_k+i)} + \beta \sum_{i=0}^{m_k} \alpha_i^{(k)} g(\boldsymbol{x}^{(k-m_k+i)})$
end
```

3.2.1 Undamped Anderson Acceleration algorithm

The key point of the method is the solution of the constrained least-square problem:

$$\min_{\alpha^{(k)}=\left[\alpha_0^{(k)},\ldots,\alpha_{m_k}^{(k)}\right]^T} = \left\|F^{(k)}\boldsymbol{\alpha}^{(k)}\right\|_2 \quad \text{with} \quad \sum_{i=0}^{m_k} \alpha_i^{(k)} = 1. \tag{3.5}$$

According to Walker et al. [82] and An et al. [84], the best way to solve the problem of Eq. (3.5) is by transforming it into an unconstrained least-square problem. By defining,

$$\Delta \boldsymbol{f}^{(i)} = \boldsymbol{f}^{(i+1)} - \boldsymbol{f}^{(i)} \quad \text{with} \quad i = k - m_k, \ldots, k-1, \tag{3.6}$$

and

$$\tilde{F}^{(k)} = \left[\Delta \boldsymbol{f}^{(k-m_k)}, \ldots, \Delta \boldsymbol{f}^{(k-1)} \right], \tag{3.7}$$

the least-square problem is then transformed to the following one:

$$\min_{\boldsymbol{\gamma}^{(k)} = \left[\gamma_0^{(k)}, \ldots, \gamma_{m_k-1}^{(k)}\right]^T} = \left\| \boldsymbol{f}^{(k)} - \tilde{F}^{(k)} \boldsymbol{\gamma}^{(k)} \right\|_2, \tag{3.8}$$

where $\boldsymbol{\alpha}$ and $\boldsymbol{\gamma}$ are related as follows:

$$\alpha_i = \begin{cases} \gamma_0 & i = 0 \\ \gamma_i - \gamma_{i-1} & 1 \le i \le m_k - 1 \\ 1 - \gamma_{m_k-1} & i = m_k \end{cases} \tag{3.9}$$

and

$$\gamma_i = \sum_{j=0}^{i} \alpha_j \quad \text{with} \quad i = 0, 1, \ldots, m_k. \tag{3.10}$$

The solution vector at the $(k+1)^{th}$ iteration is then given by,

$$\boldsymbol{x}^{(k+1)} = g(\boldsymbol{x}^{(k)}) - \sum_{i=0}^{m_k-1} \gamma_i^{(k)} \left[g(\boldsymbol{x}^{(k-m_k+i+1)}) - g(\boldsymbol{x}^{(k-m_k+i)}) \right]. \tag{3.11}$$

Actually, Eq. (3.11) can be further simplified as:

$$\boldsymbol{x}^{(k+1)} = g\left(\boldsymbol{x}^{(k)}\right) - \tilde{G}^{(k)} \boldsymbol{\gamma}^{(k)}, \tag{3.12}$$

where $\Delta \boldsymbol{g}^{(i)}$ and $\tilde{G}^{(k)}$ are defined as:

$$\Delta \boldsymbol{g}^{(i)} = g(\boldsymbol{x}^{(i+1)}) - g(\boldsymbol{x}^{(i)}) \quad \text{for} \quad i = k - m_k, \ldots, k-1, \tag{3.13}$$

$$\tilde{G}^{(k)} = \left[\Delta \boldsymbol{g}^{(k-m_k)}, \ldots, \Delta \boldsymbol{g}^{(k-1)} \right]. \tag{3.14}$$

The undamped AA algorithm with unconstrained least-square problem is shown in Algorithm 3.2.

The last task that remains to tackle is the solution of the least-square problem represented by Eq. (3.8). In this regard, the matrix $\tilde{F}^{(k)}$ of Eq. (3.7) can be *QR* factorized as:

$$\tilde{F}^{(k)} = Q^{(k)}R^{(k)} = \left[\hat{Q}^{(k)}\bar{Q}^{(k)}\right]\cdot\begin{bmatrix}\hat{R}^{(k)}\\ 0\end{bmatrix}, \tag{3.15}$$

where:

$$\begin{gathered}\tilde{F}^{(k)} \in \mathbb{R}^{n\times m_k}, Q^{(k)} \in \mathbb{R}^{n\times n}, R^{(k)} \in \mathbb{R}^{n\times m_k}\\ \hat{Q}^{(k)} \in \mathbb{R}^{n\times m_k}, \hat{R}^{(k)} \in \mathbb{R}^{m_k\times m_k}, \bar{Q}^{(k)} \in \mathbb{R}^{n\times(n-m_k)},\end{gathered} \tag{3.16}$$

and n represents the dimension of the solution vector $\boldsymbol{x}$. Finally, the least square problem for the iteration k can be re-written as:

$$\begin{aligned}\gamma &= \min_{\gamma}\left\|\boldsymbol{f} - \tilde{F}\gamma\right\|_2 = \min_{\gamma}\left\|\boldsymbol{f} - QR\gamma\right\|_2 = \min_{\gamma}\left\|Q^T\boldsymbol{f} - R\gamma\right\|_2 =\\ &= \min_{\gamma}\left\|\begin{pmatrix}\hat{Q}^T\\ \bar{Q}^T\end{pmatrix}\boldsymbol{f} - \begin{pmatrix}\hat{R}\\ 0\end{pmatrix}\gamma\right\|_2 = \min_{\gamma}\left\|\begin{pmatrix}\hat{Q}^T\boldsymbol{f} - \hat{R}\gamma\\ \bar{Q}^T\boldsymbol{f}\end{pmatrix}\right\|_2 = \quad .\\ &= \min_{\gamma}\left\|\left(\hat{Q}^T\boldsymbol{f} - \hat{R}\gamma\right)\right\|_2\end{aligned} \tag{3.17}$$

The AA algorithm is then applied to the vector $\boldsymbol{x}_{GS}$ given by Eq. (3.2). The form of the FPI vector differs from the one used in previous works [12], [15], in fact it only contains the three groups of T/H variables. A detailed description of the implementation strategy is provided in a report by Walker [85].

Algorithm 3.2: Anderson Acceleration method, undamped algorithm with unconstrained least-square problem.

```
Algorithm. Undamped Anderson Acceleration
Given $\boldsymbol{x}^{(0)}$ and $m \geq 1$,
set $\boldsymbol{x}^{(1)} = g(\boldsymbol{x}^{(0)})$.
while ($conv$)
    Set $m_k = min(m,k)$ and
    calculate $g(\boldsymbol{x}^{(k)})$.
    Set $\boldsymbol{f}^{(k)} = g(\boldsymbol{x}^{(k)}) - \boldsymbol{x}^{(k)}$;
    set $\tilde{F}^{(k)}$ and $\tilde{G}^{(k)}$ according to Eqs. (3.7) and (3.14).
    Determine $\boldsymbol{\gamma}^{(k)} = \left[\gamma_0^{(k)}, \ldots, \gamma_{m_k-1}^{(k)}\right]$ which solves:
        $\min_{\gamma^{(k)}} \left\| \left( \boldsymbol{f}^{(k)} - \tilde{F}^{(k)} \boldsymbol{\gamma}^{(k)} \right) \right\|_2$.
    Calculate:
        $\boldsymbol{x}^{(k+1)} = g\left(\boldsymbol{x}^{(k)}\right) - \tilde{G}\boldsymbol{\gamma}^{(k)}$
end
```

3.2.2 Implementation

The method presented in Algorithm 3.2 is applied once the T/H solver has updated the distributions of coolant density, coolant temperature and fuel temperature. After the first T/H calculation, the necessary vectors and matrices are initialized and the elements of the first solution, namely the distributions of the aforementioned T/H field variables are stored in the vector $\boldsymbol{x}^{(1)} = g(\boldsymbol{x}^{(0)})$. The entries of the solution vector $\boldsymbol{x}^{(1)}$ are hence normalized to their respective maximum value to keep the algorithm stable. Then the neutronics and T/H calculations are repeated once more without applying the AA since there is no previous solution yet. The subsequent steps are thus performed as shown in Algorithm 3.2.

Initially, $g(\boldsymbol{x}^{(k)})$ is set to the new T/H solution obtained by the solver. The new residual is then obtained as $\boldsymbol{f}^{(k)} = g(\boldsymbol{x}^{(k)}) - \boldsymbol{x}^{(k)}$ and the difference $\Delta\boldsymbol{f}^{(k)} = \boldsymbol{f}^{(k+1)} - \boldsymbol{f}^{(k)}$ is stored in a two dimensional array $\tilde{G}^{(k)}$ which has the size (m, n) where n is the number of the T/H variables. After that, the matrix $\tilde{F}^{(k)} = Q^{(k)}R^{(k)}$ in Eq. (3.15) is computed from $\tilde{F}^{(k-1)}$ by adding a column to the right and shifting the others to the left. In this way, the acceleration can be applied immediately from the second iteration. When $m_{k\text{-}1} = m$, the first column on the left of $\tilde{F}^{(k\text{-}1)}$ must be deleted [85]. The update of $Q^{(k)}R^{(k)}$ is then performed according to a single modified Gram-Schmidt sweep [85]. Finally, the solution of Eq. (3.17) is performed using backward substitution and the new T/H fields can be updated according to Eq. (3.12).

In the parallel execution of nTRACER/ESCOT, the AA calculations are performed on the single processor occupied by the parent process since the size of the vector is limited to:

$$m \cdot n = m \cdot \Big(\underbrace{2 \cdot n_{pin} \cdot n_z}_{\substack{\text{Coolant vars.} \\ (\rho_{cool}, T_{cool})}} + \underbrace{n_{pin} \cdot n_z \cdot n_{mesh}}_{\substack{\text{Fuel Conduction} \\ \text{Points}}} \Big), \tag{3.18}$$

where n_{pin} is the number of fuel pins, n_z is the number of axial planes and n_{mesh} is the number of meshes used by fuel conduction solver.

The wrapper code receives the ρ_{cool}, T_{cool}, T_{fuel} distributions from ESCOT; calculates $\boldsymbol{\gamma}^{(k)}$ and determines $\boldsymbol{x}^{(k+1)}$; and sends the T/H field variables to the neutronics solver which updates the cross sections and proceeds with the 2D MOC.

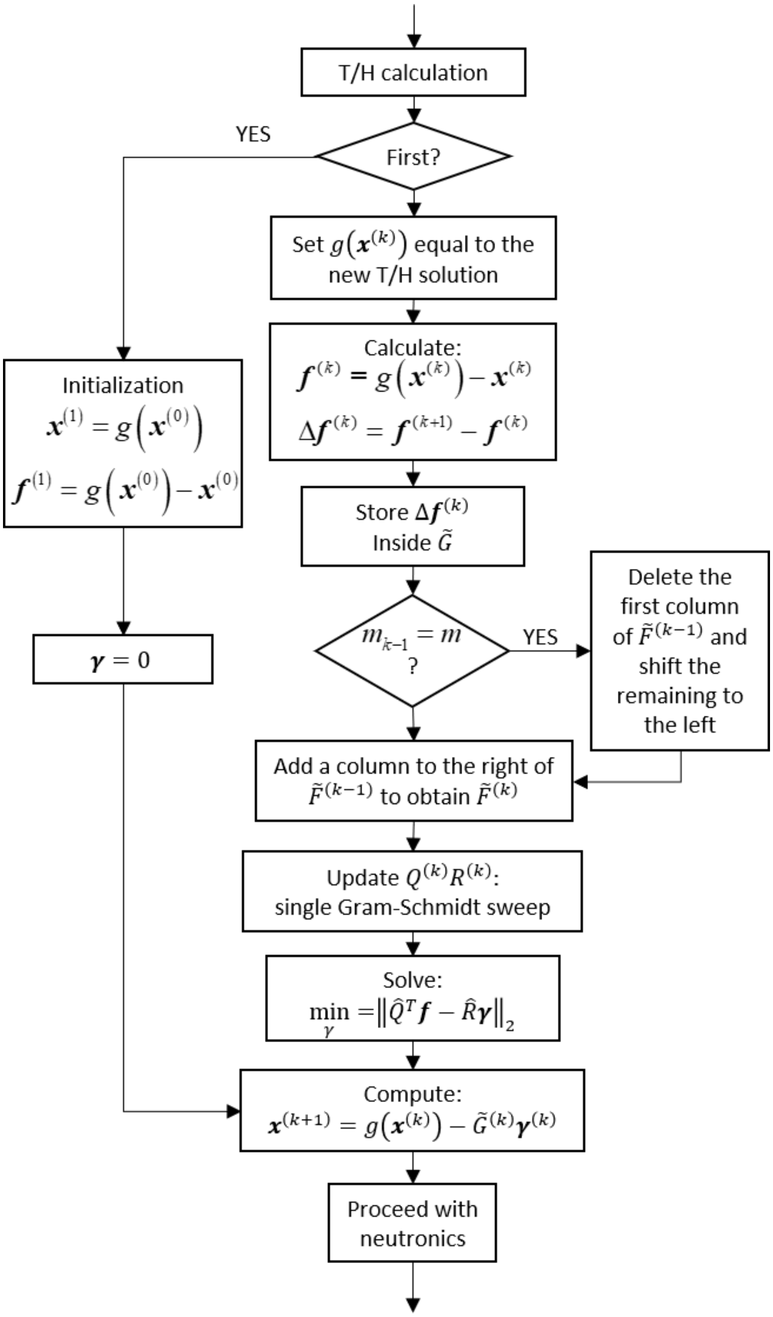

Fig. 3.5: Anderson Acceleration flowchart adopted inside the nTRACER code for the neutronics-T/H calculation.

3.3 Assessment of the Anderson Acceleration performances

In order to properly assess the acceleration performance of AA-*m* implemented in nTRACER, a variety of neutronics-T/H coupled problems spanning from a set of 3D reduced problems to realistic core problems, have to be examined. The set of reduced problems involves the calculation of single assembly (SA), checker-board (CB) and a minicore as shown in Fig. 3.6. All the material composition used in this problem are referring to fuel assemblies of the Korean OPR1000 reactor whose rated electrical power is 1,000 MW. The set of actual core problems concerns the simulation of the OPR1000, APR1400 and BEAVRS [86] reactor cores. Note that APR1400 is the new generation Korean PWR whose rated electrical power is 1,400 MW. The main characteristics of these three cores are given in Tab. 3.1.

The main objective of the reduced analysis is to show eventual pros and cons of the acceleration technique. Thus, the internal simple T/H module of nTRACER is used for the reduced problems.

Three main fission source errors can be defined as indicator of the convergence state. The fission source true error is defined as:

$$\varepsilon_{k+1} = \frac{\left\| \psi^{(k+1)} - \psi^{*} \right\|_2}{\left\| \psi^{*} \right\|_2}, \tag{3.19}$$

where ψ is the fission source vector and the superscript * denotes the true solution, which can be obtained by imposing very tight convergence criterion and then stored to estimate of the error of the intermediate fission source vector generated after each iteration.

The use of this error estimate allows to distinguish the true number of FPIs (TFPI) from the actual number of FPIs (AFPI). The number of TFPIs represents the number of the alternating calculations of neutronics and T/H to converge the true error while the AFPIs is the number of iterations for the following fission source pseudo error to be reduced below the desired convergence criterion:

$$\tilde{\varepsilon}_{k+1} = \frac{\left\|\psi^{(k+1)} - \psi^{(k)}\right\|_2}{\left\|\psi^{(k+1)}\right\|_2} . \tag{3.20}$$

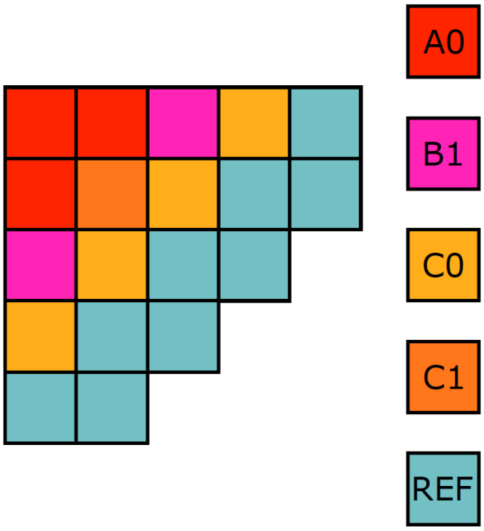

Fig. 3.6: radial map of the minicore used for the reduced analysis of the Anderson Acceleration scheme.

Tab. 3.1: characteristics parameters of the cores used for the actual reactor problems.

Item	OPR1000	APR1400	BEAVRS
Power [MW_{th}]	2,815	3,983	3,410
Number of FA	177	241	193
FA Type	CE 16x16	CE 16x16	WH 17x17
Gd_2O_3 wt. [%]	4.0	8.0	-

The fission source pseudo error showed in Eq. (3.20), represents the difference between the fission source calculated after and before a MOC sweep. The difference between two fission sources after the MOC sweep can be defined as:

$$\overline{\overline{\varepsilon}}_{k+1} = \frac{\left\|\psi^{(k+1)} - \psi_0^{(k)}\right\|_2}{\left\|\psi^{(k+1)}\right\|_2}, \tag{3.21}$$

where $\psi_0^{(k+1)}$ represents the fission source calculated after the previous iteration MOC. To help the reader, Fig. 3.7 shows the position where each ψ is calculated onto the nTRACER flowchart. The error defined in Eq. (3.21) is not used in neutronics code but it is useful for the sake of this study.

Those results are also published here [87].

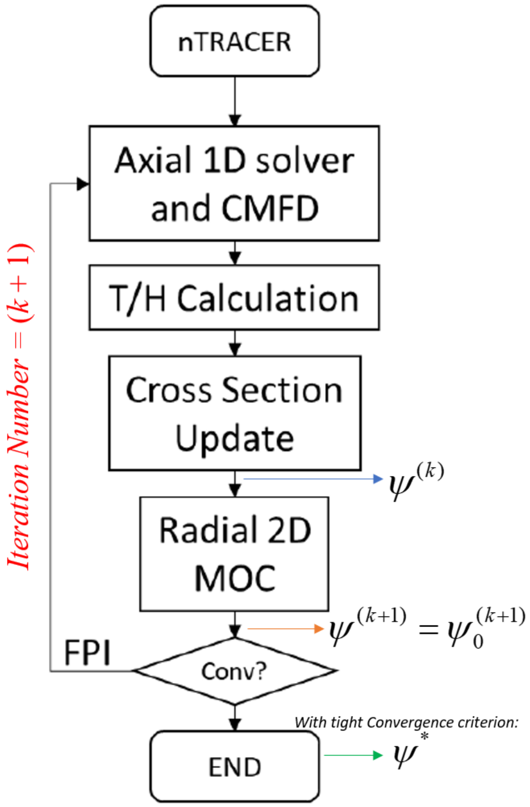

Fig. 3.7: position of the different types of fission sources used to compute the three different kinds of errors.

The reference solution is obtained by imposing a convergence criterion of $\varepsilon = 5 \cdot 10^{-9}$ on the fission source pseudo error. Since obtaining a reference with such a tight convergence for the actual core problems is excessively time consuming, the convergence check for the second set of problems is done by using only the pseudo error.

The execution of the nTRACER/ESCOT coupled cases here reported were carried out on a LINUX cluster which has the following specifications:

- # of computing nodes: 27,

- CPU per node: 2 Intel Xeon E5-2640 v3 having 8 cores of 2.8 GHz each, and
- Interconnection: Intel Omni-path Infiniband EDR (58Gbps).

3.3.1 Reduced problems

The first assessment of AA is performed for the assemblies A0, B1, C0 and C1 of the OPR1000 model while the second assessment is for the CBs consisting of B1 & A0, B1 & C0, C1 & A0 and C1 & C0. Finally, the third concerns the minicore shown in Fig. 3.6. Note that the alphanumeric assembly ID represents the enrichment while the numeric ID is for distinction in gadolinia loading. The coupled calculations were carried out using the nTRACER internal T/H solver with the equilibrium xenon option. For the minicore, the boron concentration was set to 400*ppm*.

The convergence is monitored using the true error. The convergence criterion of 10^{-3} is used to determine the TFPIs which amounts to the fission source pseudo error of about 10^{-5} as shown later. If the true error criterion is met earlier than the pseudo error criterion, additional iterations are performed. Additionally, the eigenvalue convergence criterion was set equal to10^{-6}. For every problem, three calculations are performed with m ranging from 0 to 2, namely AA-0, AA-1 and AA-2. In fact, higher values of m were not necessary because the FPI converges within 5 to 9 iterations when AA is used. Note that AA-0 is the original GS FPI. The results of the reduced problems are shown in Tab. 3.2 and Tab. 3.3 for the eigenvalues and the number of iterations, and in Fig. 3.8, Fig. 3.9 and Fig. 3.10 for the error behaviors.

Except for the B1 assembly case, the eigenvalue error with respect to the reference is less than 5*pcm*. The maximum error in the axially integrated 2D power distribution is only 0.03% for all the cases. As shown in Tab. 3.3, several cases show a drastic decrease from AA-0 in the number of AFPI and it is even higher in case of TFPI. For some cases the number of iterations is reduced by a factor of two.

It is noted in several cases that the pseudo error does not meet its convergence criterion even though the true error does. For example, the true error of the AA-2 case for B1 converges after 7 iterations resulting in the reduction of the number of FPIs by a factor of two from AA-0. The pseudo error, however, does not meet its convergence criterion so that two more iterations are necessary as shown in Fig. 3.8 with a dashed line. A similar behavior is visible in Fig. 3.9 which is for C1A0 (*top*) and C1C0 (*bottom*) checker-boards, and also in Fig. 3.10 which is for the minicore. The accelerated cases reveal a steep reduction in true error within two consecutive iterations, but the pseudo error cannot catch that because the change between two iterations is large. In practical cases, however, the true solution is not available. Thus, it would be necessary to either loosen the convergence criterion or to change the convergence estimator when AA is applied.

Finally, the Anderson Acceleration is a better technique than the use of relaxation factors because it does not require any input data. In particular, AA-1 can be seen as a relaxation method; the algorithm generates γ online by minimizing the residuals of the FPI vector and adjusts the value accordingly providing a proper relaxation factor for the analyzed problem. Fig. 3.11 shows the evolution of γ_1 for the case of the assembly B1 simulated with AA-1.

Tab. 3.2: eigenvalues of the true solution, AA-0, AA-1 and AA-2 calculations of the reduced models.

	TRUE	**AA-0**	**AA-1**	**AA-2**
	k-eff	k-eff (diff)	k-eff (diff)	k-eff (diff)
A0	1.08921	1.08920 (-1)	1.08922 (1)	1.08921 (0)
B1	1.14501	1.14501 (0)	1.14491 (-10)	1.14491 (-10)
C0	1.30662	1.30661 (-1)	1.30663 (1)	1.30664 (2)
C1	1.13309	1.13309 (0)	1.13309 (0)	1.13309 (0)
B1A0	1.11477	1.11477 (0)	1.11478 (1)	1.11478 (1)
B1C0	1.23582	1.23583 (1)	1.23579 (-3)	1.23578 (-4)
C1A0	1.10788	1.10789 (1)	1.10790 (2)	1.10790 (2)
C1C0	1.22858	1.22857 (-1)	1.22855 (-3)	1.22853 (-5)
Mini Core	0.99981	0.99982 (1)	0.99984 (3)	0.99983 (2)

Tab. 3.3: number of true and actual FPI for the reduced problems.

	AA-0	**AA-1**		**AA-2**	
	FPI	TFPI (GAIN)	AFPI (GAIN)	TFPI (GAIN)	AFPI (GAIN)
A0	5	5 (0)	5 (0)	5 (0)	5 (0)
B1	12	9 (3)	9 (3)	7 (5)	9 (3)
C0	15	7 (8)	8 (7)	8 (7)	8 (7)
C1	18	8 (10)	8 (10)	9 (9)	9 (9)
B1A0	8	6 (2)	7 (1)	6 (2)	6 (2)
B1C0	14	6 (8)	7 (7)	7 (7)	8 (6)
C1A0	8	6 (2)	7 (1)	7 (1)	7 (1)
C1C0	15	7 (8)	7(8)	7 (8)	8 (7)
Mini Core	10	7 (3)	7 (3)	6 (4)	7 (3)

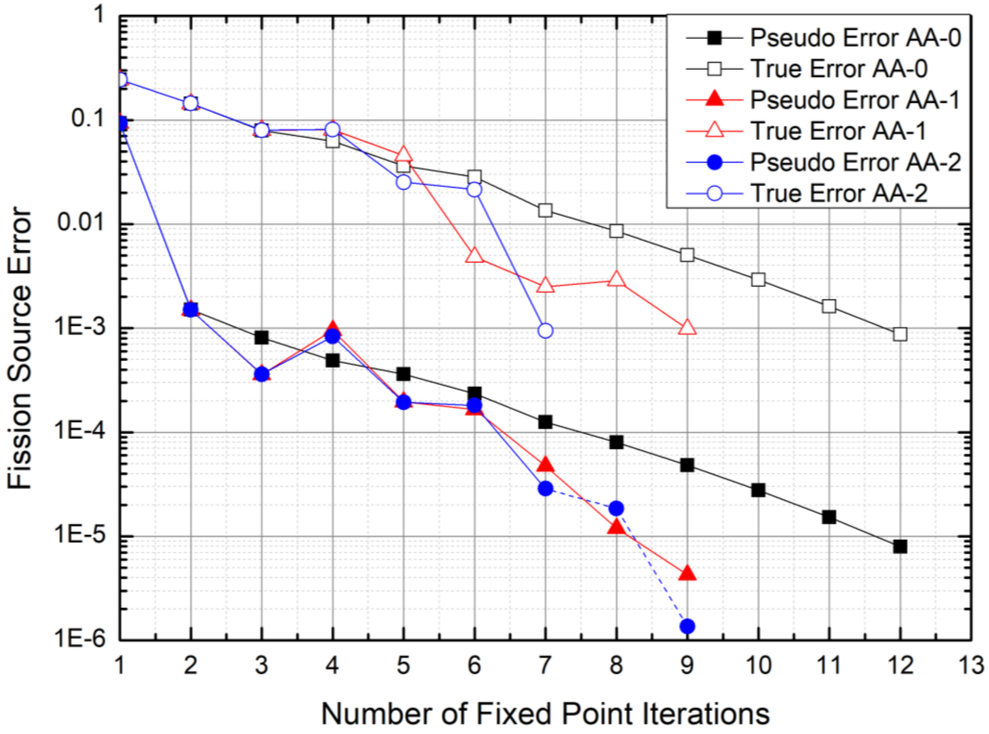

Fig. 3.8: fission source error reduction behavior for B1.

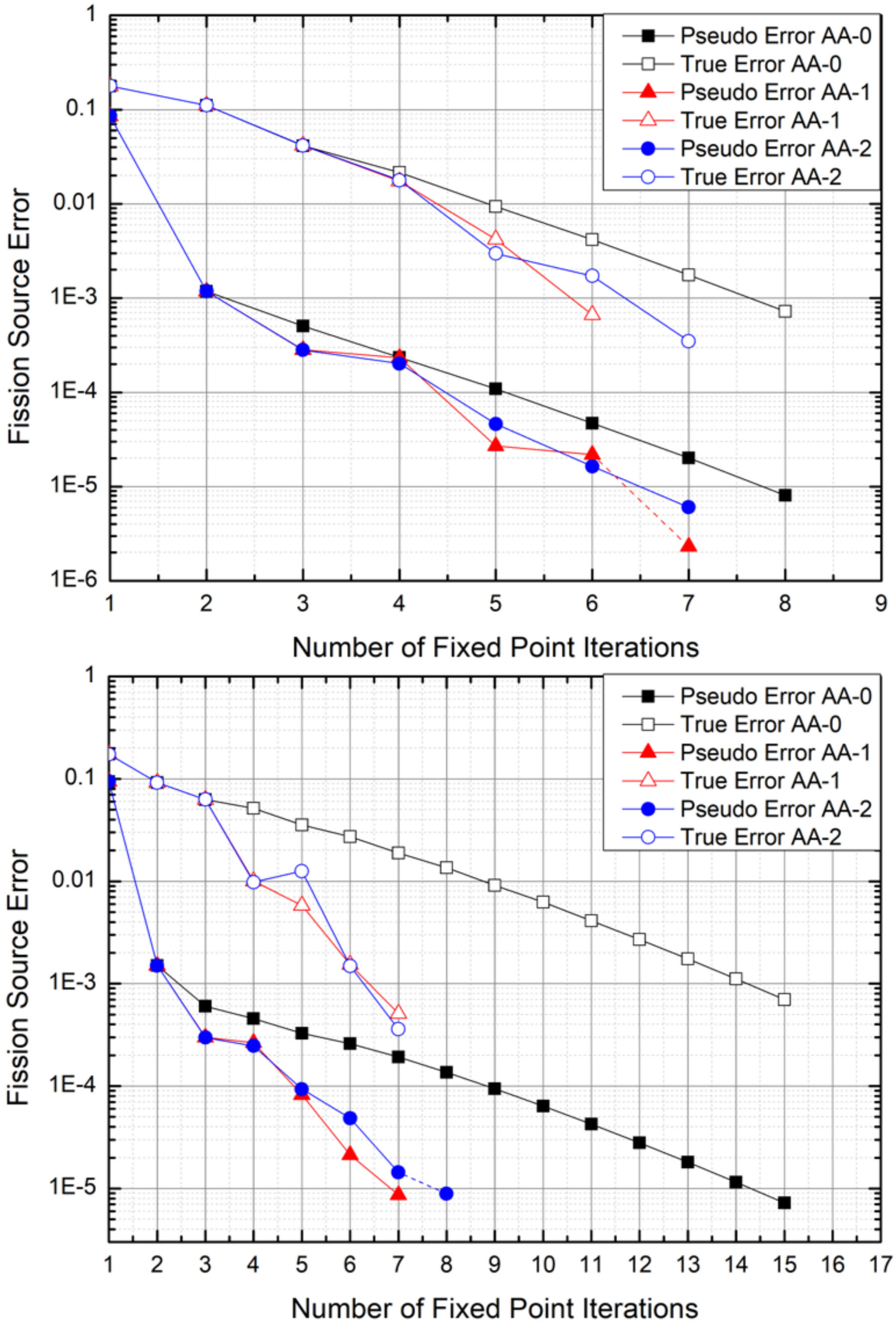

Fig. 3.9: fission source error reduction behavior for the checker-board problems C1A0 (*top*) and C1C0 (*bottom*).

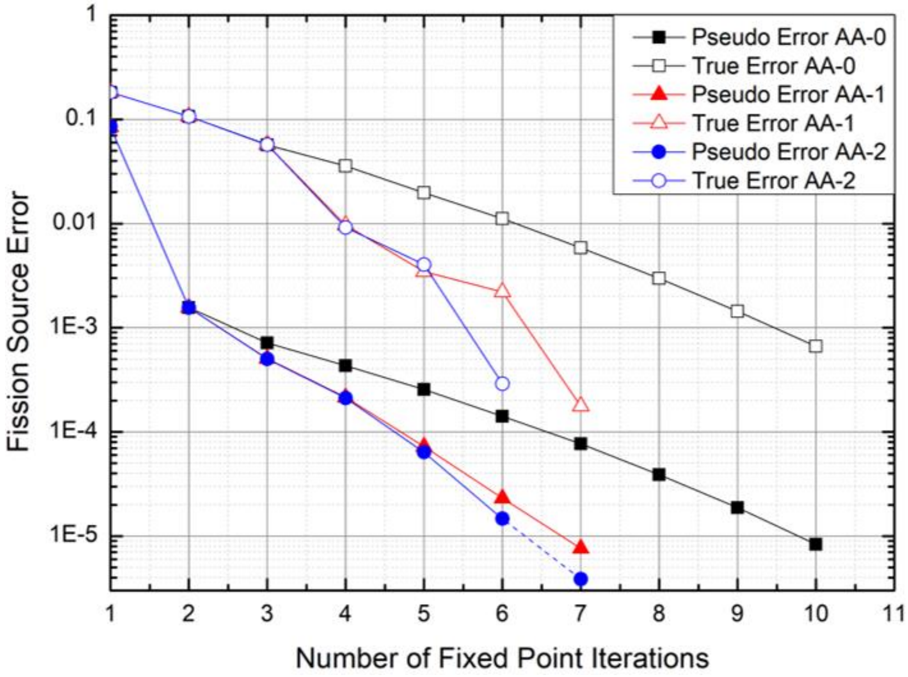

Fig. 3.10: fission source error reduction behavior for the minicore.

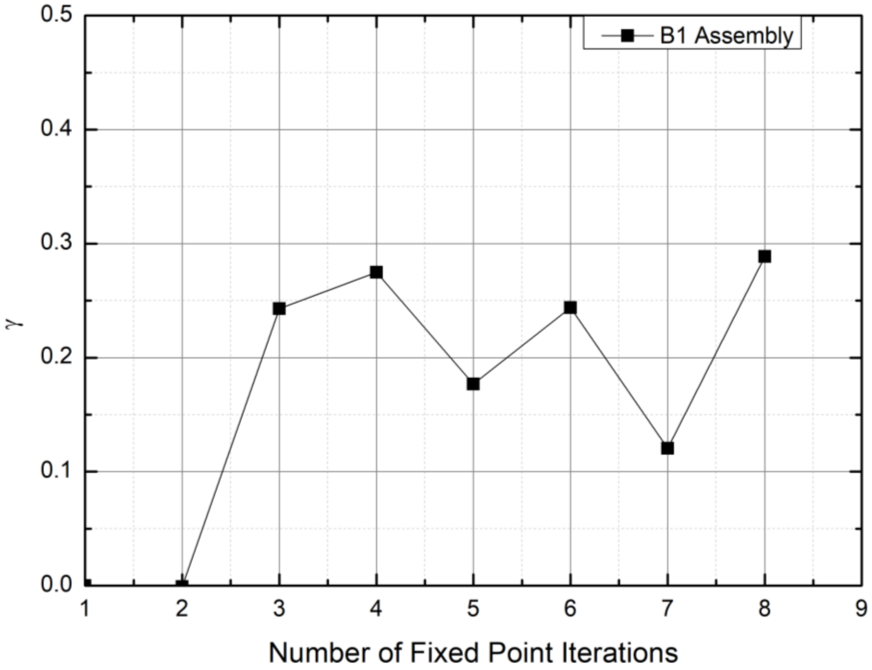

Fig. 3.11: evolution of γ_1 with the number of FPIs for the single assembly B1.

The last task to solve is represented by answering to the reason why the true error value results two order of magnitude bigger than the pseudo error (see Fig. 3.8, Fig. 3.9 and Fig. 3.10) while the distance between two successive values of the fission source in Fig. 3.1 is bigger than the distance between the current fission source and its true solution. The reason can be explained by plotting for that specific calculation (OPR1000 full core calculation with simple T/H) the error defined in Eq. (3.21), in fact the error between two entire FPI results ($\bar{\bar{\varepsilon}}$) bigger than the true error.

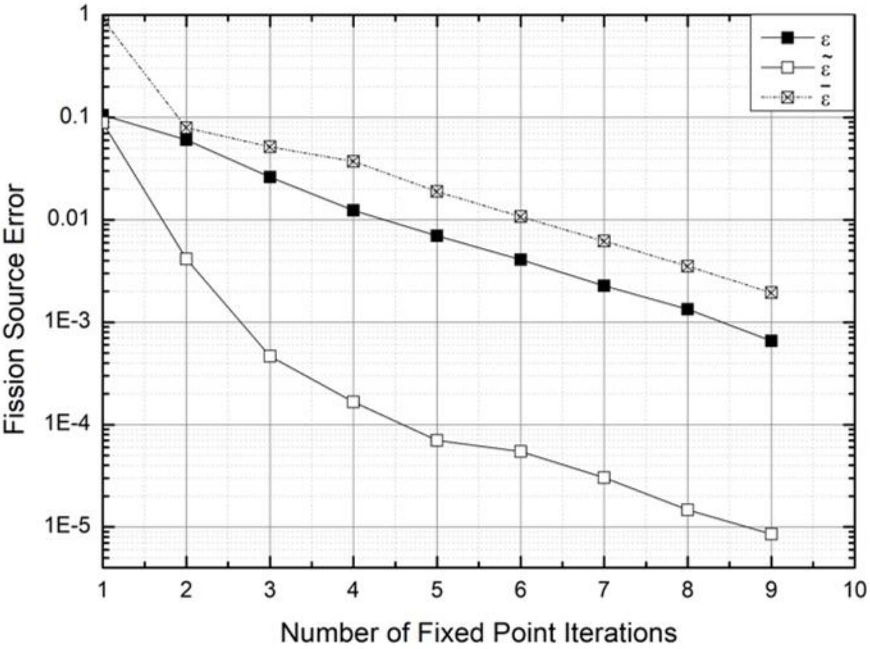

Fig. 3.12: evolution of the three types of error for the OPR1000 quarter core.

3.3.2 Actual core problems

Accurate prediction of cross-flow, mixing effects, spacer-grid effects, fuel temperature and possible presence of local void fraction is necessary to faithfully model the coolant flow in the core of a nuclear reactor. This can be done by using the ESCOT T/H module. Thus, the coupled analyses for the actual core problems are done with the nTRACER/ESCOT code. However, for the sake of comparison, these problems have been also examined with the simple internal T/H module. The following chapters describe the core analysis performed in case of simple feedback and depletion calculations.

3.3.2.1 Simple feedback calculation

Three cores are analyzed: OPR1000, APR1400 and BEAVRS. For BEAVRS two power levels corresponding to 75% and 100% of the nominal value are examined. The coupled calculations were carried out searching the critical boron concentrations (CBC) and with the equilibrium xenon option.

The CBCs and the number of FPIs obtained with AA-0, AA-1 and AA-2 for the four analyzed cases are given in Tab. 3.4. The CBCs show negligible differences and the number of AFPIs for the accelerated cases is always smaller than the non-accelerated ones. It is noted that the root means square (RMS) and maximum (MAX) differences in the axially integrated 2D power distribution do not exceed 0.02% and 0.05% for the nTRACER standalone cases and for the nTRACER/ESCOT cases. The fission source pseudo error reduction behaviors are shown in Fig. 3.13 for the OPR1000 core obtained with nTRACER standalone (*top*) and with nTRACER/ESCOT (*bottom*). Similar plots are given in Fig. 3.14 for the BEAVRS core at full power.

In order to check the fundamental factors for the better convergence noted in the reduced and actual core problems, the oscillatory behavior in fission source convergence that might happen at 3 ~ 4 FPIs are examined. It is observed for AA-0 of both OPR1000 and BEAVRS full power case by the changed slope at Iteration 5 in Fig. 3.13 and at Iteration 4 in Fig. 3.14. Note that almost the same values are registered for the fission source pseudo error at Iterations 5 and 6 of OPR1000 and 4 and 5 of BEAVRS full power for both nTRACER standalone and nTRACER/ESCOT. This means that the solution varies too much between those iterations. This is the result of overshooting [79], [80]. This behavior is not observed for the accelerated cases because the oscillations are absorbed by the use of the smoothing factors which do not allow large variations of the solution between two successive iterations. In fact, the changes in slope of the fission source pseudo error after Iteration 5 for OPR1000 (or 4 for BEAVRS) do not appear for AA-1 or AA-2. The changes in slope are avoided and convergence is met earlier with AA-*m*. The oscillations observed in the local fission source noted in Fig. 3.1 disappear as shown in Fig. 3.15. Note that the overshooting does not appear with AA-1 and AA-2 thanks to the smoothening effect of AA so that the convergence can be reached earlier.

Not all the calculated problems have presented overshooting of the solution with oscillations around the reference. In fact, the reduction of FPI number is not the same for all the examined cases as Tab. 3.4 shows for the APR1400 or for BEAVRS simulated at 75% of the nominal power.

Tab. 3.4: critical boron concentrations and number of Fixed-Point iterations for the actual core cases

Case		**AA-0**		**AA-1**		**AA-2**	
		CBC	FPIs	CBC	FPIs	CBC	FPIs
OPR1000	nTRACER	751.3	9	751.2	6	751.3	6
	nTRACER/ESCOT	753.6	8	753.7	6	753.6	7
APR1400	nTRACER	819.9	6	819.9	5	819.9	5
	nTRACER/ESCOT	822.1	6	822.1	5	822.1	5
BEAVRS 75%	nTRACER	671.1	7	671.1	6	671.1	6
	nTRACER/ESCOT	672.4	7	672.5	6	672.5	6
BEAVRS 100%	nTRACER	630.9	9	631.0	6	631.0	6
	nTRACER/ESCOT	632.6	8	632.8	7	632.6	6

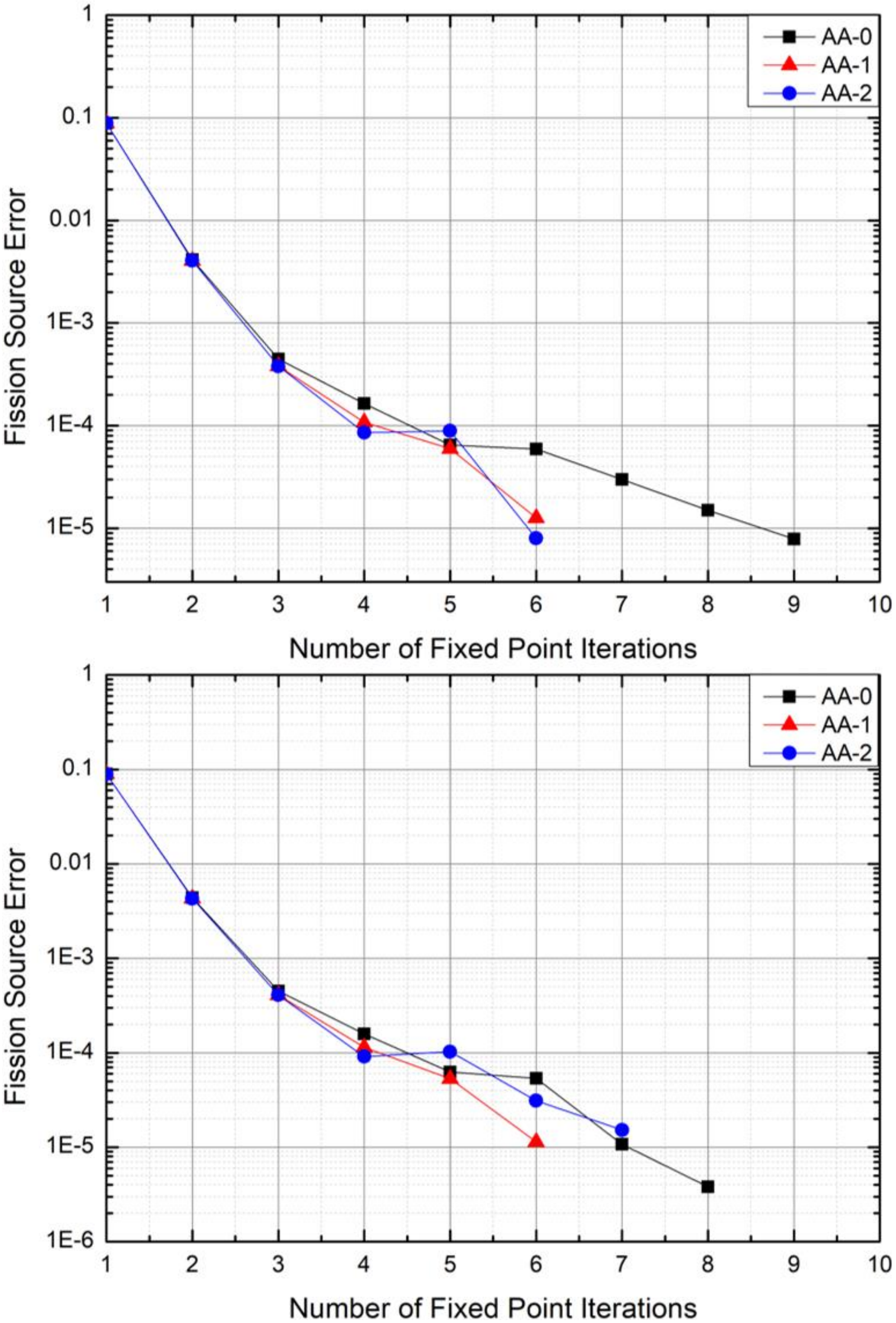

Fig. 3.13: fission source pseudo error behavior for the OPR1000 core obtained with nTRACER standalone (*top*) and nTRACER/ESCOT (*bottom*).

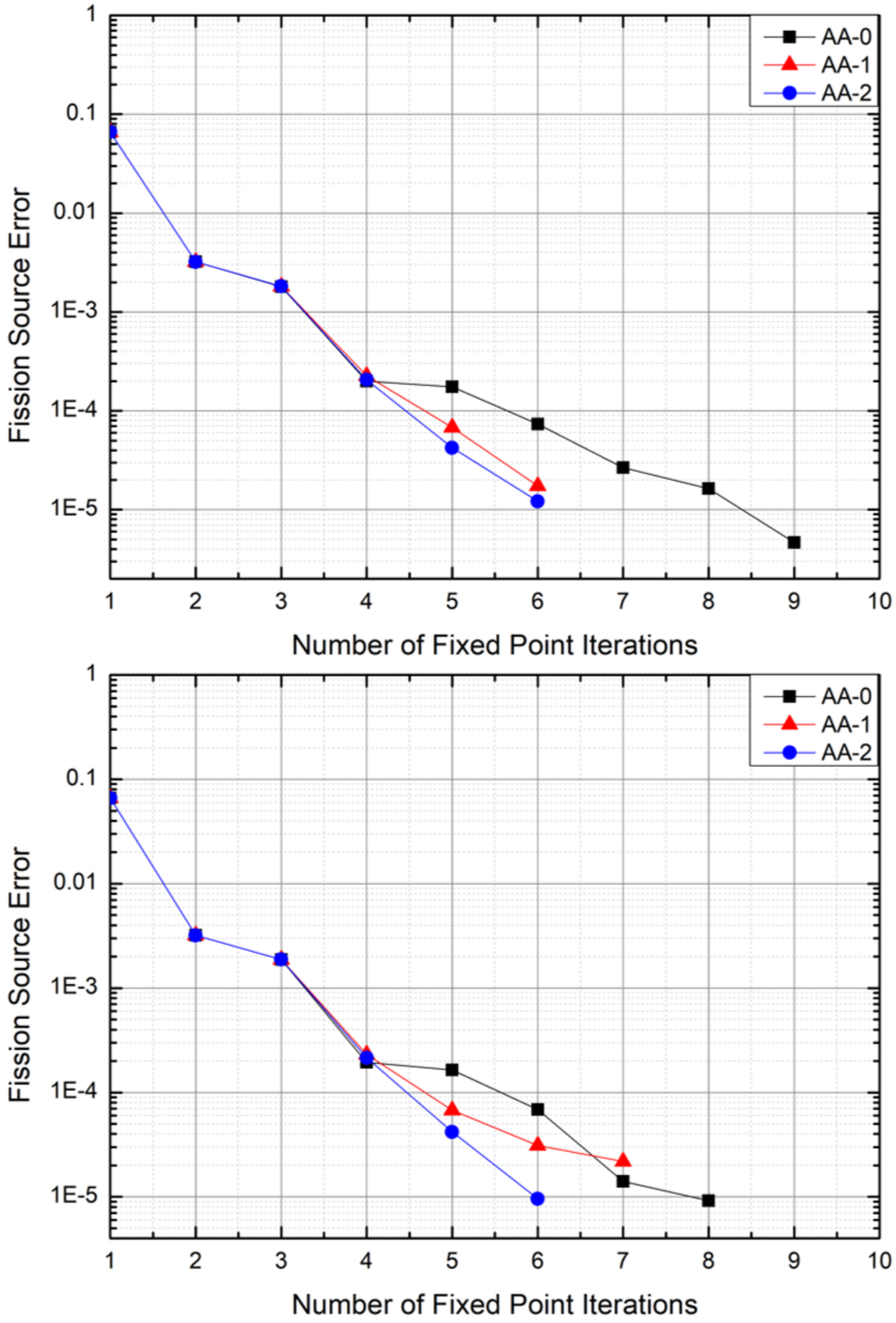

Fig. 3.14: fission source pseudo error behavior for the BEAVRS-100% core obtained with nTRACER standalone (*top*) and nTRACER/ESCOT (*bottom*).

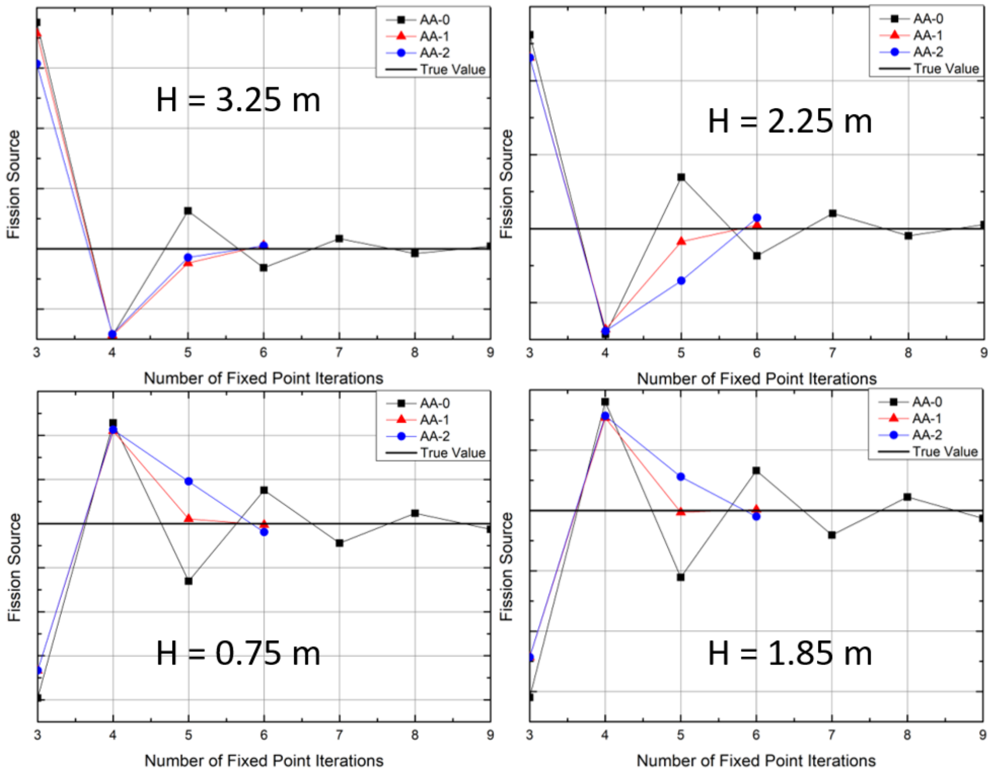

Fig. 3.15: convergence behavior of four fission source values around the reference solution for the OPR1000 core.

The reduction in FPIs yields less computing time. The average time to complete a full FPI iteration is about 8 minutes for nTRACER standalone and about 9 minutes for nTRACER/ESCOT calculations. The fewer number of FPIs is responsible for a significant computing time saving as shown in Tab. 3.5 in which the total computing times are listed for the four core cases. In the case of nTRACER standalone calculation for OPR1000 the time reduction moving from AA-0 to AA-1 or AA-2 is about 20 minutes which is almost one third of the total computing time.

Tab. 3.5: total calculation time of the four reactor cores simulated both with nTRACER standalone and nTRACER/ESCOT.

Case		AA-0	AA-1	AA-2
OPR1000	nTRACER	60	40	40
	nTRACER/ESCOT	63	45	53
APR1400	nTRACER	50	41	41
	nTRACER/ESCOT	53	45	45
BEAVRS 75%	nTRACER	53	47	47
	nTRACER/ESCOT	59	53	53
BEAVRS 100%	nTRACER	70	49	48
	nTRACER/ESCOT	70	62	55

3.3.2.2 Depletion calculations

Depletion analyses can be seen as different FPI problems for each different burnup step. Thus, Lee [17] recommended to reset the residuals of AA every time the fuel composition changes. However, the benefits obtained by the application of smoothing factors led to start analyzing the effect of non-resetting the residuals of the AA.

In order to investigate this, three burnup calculations taken from the model of the OPR1000, two checker-boards and the minicore depicted in Fig. 3.6, have been analyzed employing the same acceleration level AA-2 and nTRACER standalone. In one case the acceleration was reset every time the fuel composition has changed while in the other one AA has never been reset.

The calculation conditions for this initial assessment were: 10 burnup steps (up to $7MWd/kg_U$) and predictor-corrector methodology. In every calculation the xenon equilibrium option was activated. The calculation of the minicore burnup was performed in boron search mode. The evolution of the eigenvalue for checker-boards C1C0 (*top*) and C1A0 (*bottom*) are shown in Fig. 3.16 while Fig. 3.17 shows the boron letdown curve for the minicore. The differences in eigenvalue are below

10*pcm* and 0.5*ppm*. Thus, there is not loss of accuracy in case of no-reset of AA.

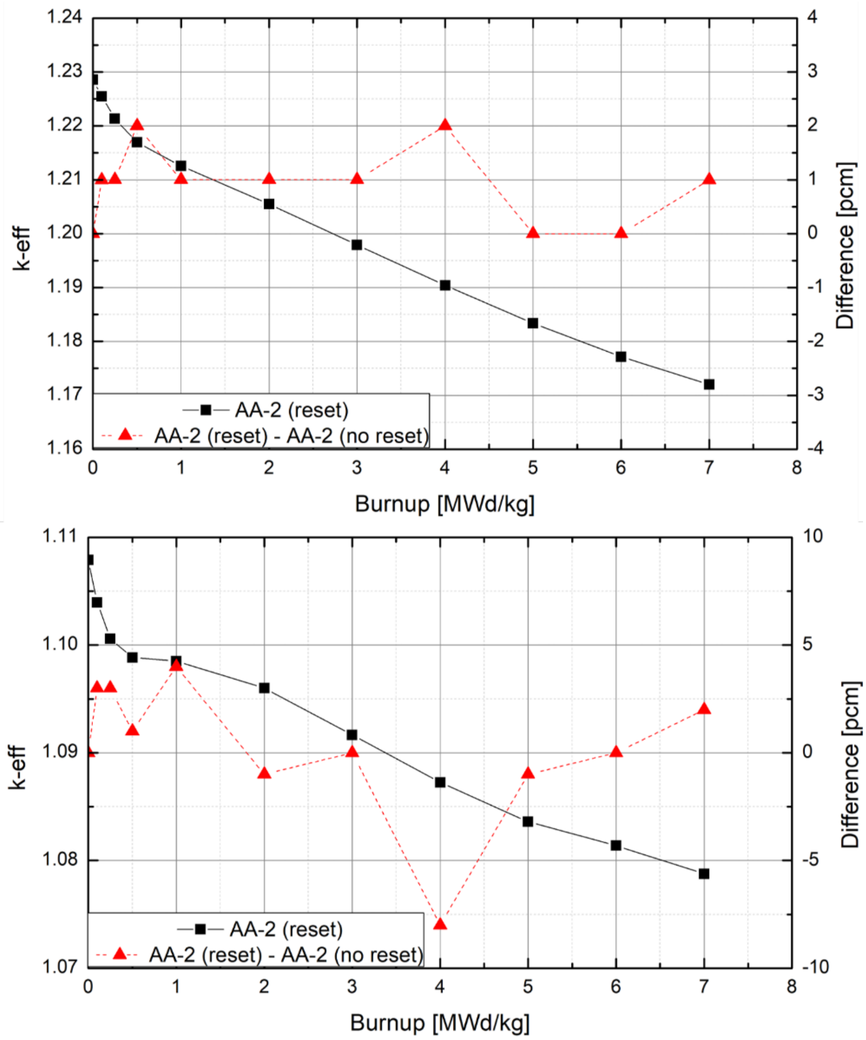

Fig. 3.16: evolution of *k-eff* with burnup for AA-2 with reset and difference in *pcm* from AA-2 reset and AA-2 no-reset for C1C0 (*top*) and C1A0 (*bottom*) checkerboards.

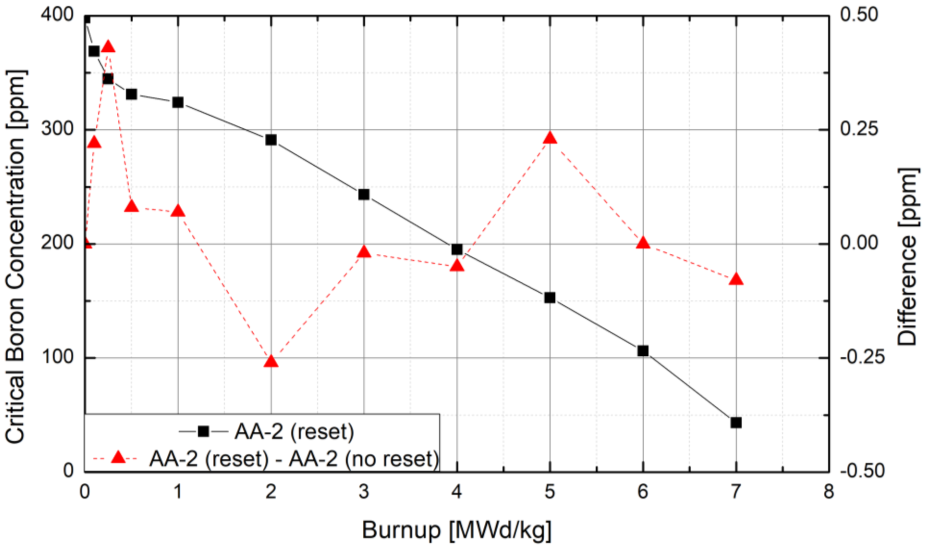

Fig. 3.17: Critical Boron Concentration with burnup for the minicore problem and the difference in CBC from AA-2 reset for the AA-2 no-reset case.

The lack of reset led to a global decrease of the total number of iterations (predictor + corrector) which yielded a decrease in calculation time. Fig. 3.18 and Fig. 3.19 show that if AA is not reset the total number of FPI can decrease. For these three simulated cases the total number of iterations reduced by about 17% retaining the accuracy. Thus, the following core analysis will be performed employing the non-reset of AA.

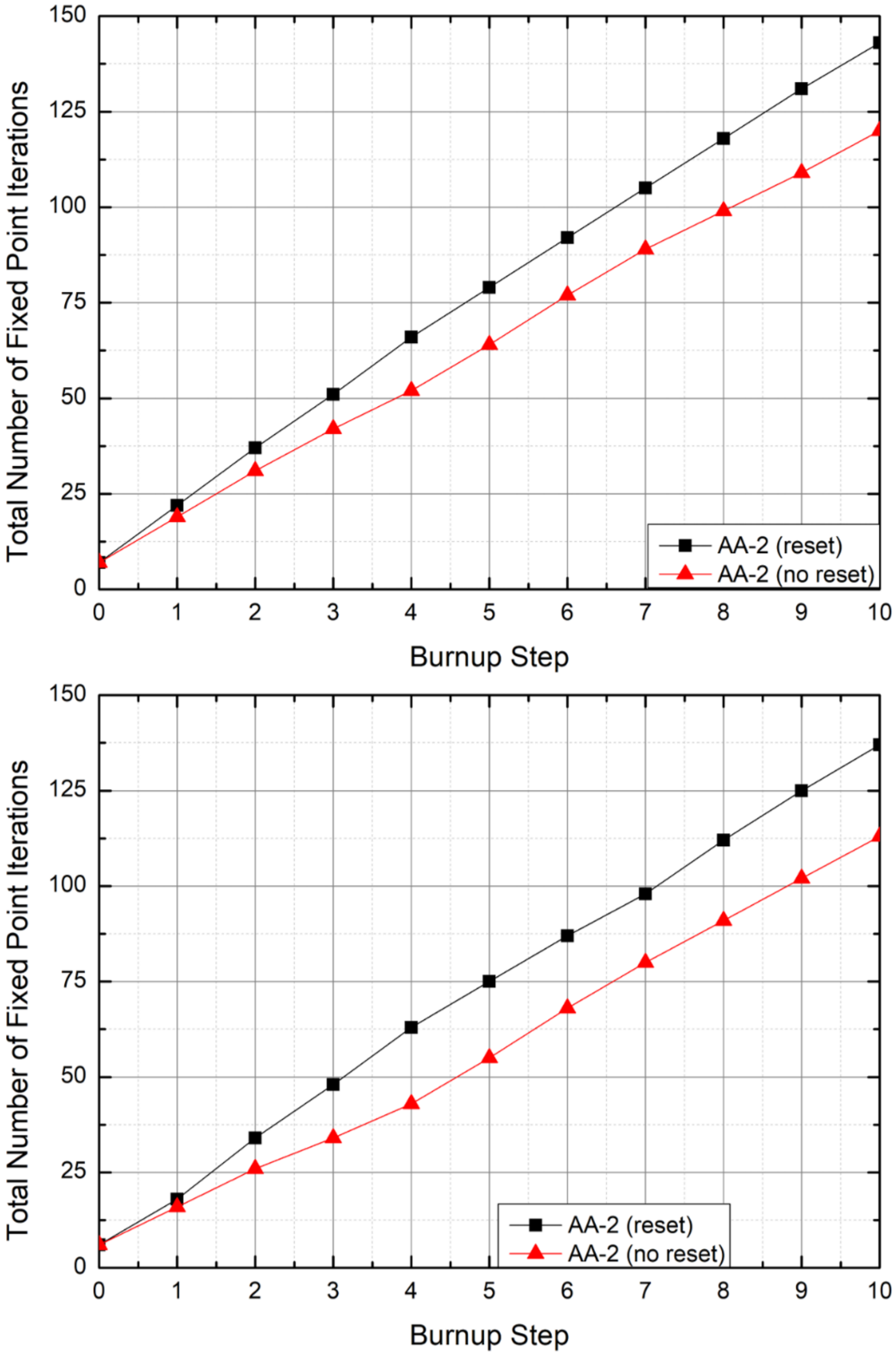

Fig. 3.18: total number of FPI for the depletion analyses, checker-boards C1C0 (*top*) and C1A0 (*bottom*).

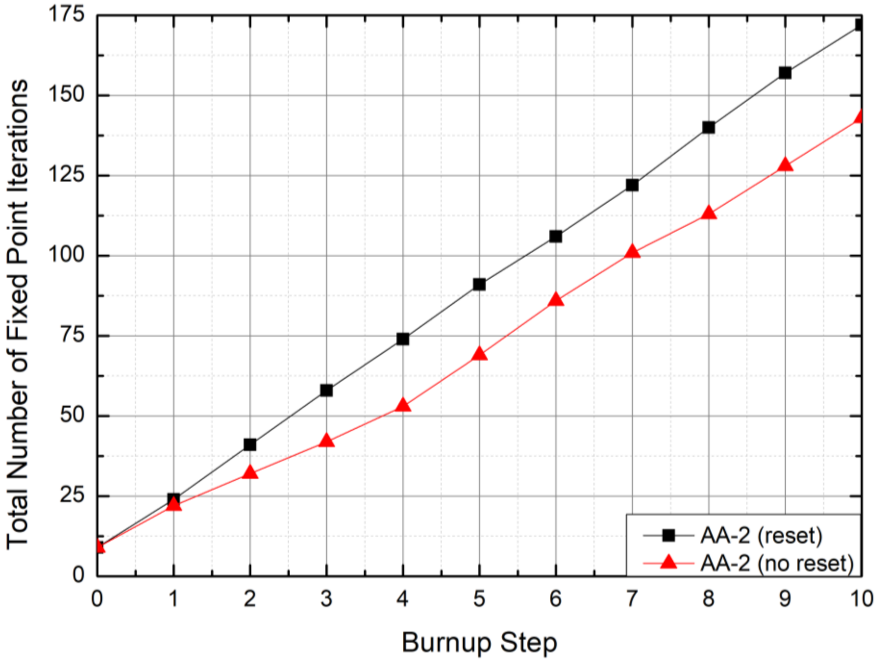

Fig. 3.19: total number of FPI for the depletion analyses of the minicore.

A depletion calculation was performed for OPR1000 to examine AA performance over core burnup in this case using nTRACER/ESCOT with the predictor-corrector methodology. The core depletion was done for Cycle 1 employing 16 burnup steps. It turned out that the CBC difference between the different AA-*m* cases does not exceed 0.8*ppm* throughout the cycle as shown in Fig. 3.20 and that the 2D axially integrated power distributions agree within 0.04%. Fig. 3.21 provides the trend of the number of AFPIs for the three cases (*top*) and the gain in FPIs at each burnup step (*bottom*). Both AA-1 and AA-2 drastically reduce the total number of FPIs from 283 of the non-accelerated case to 224 for AA-1 and 213 for AA-2, yielding an average FPI gain of 4 or 5 and a maximum of 10 for some steps. To a such reduction in the number FPIs, it corresponds a cut of about 20%~25% in the computational load.

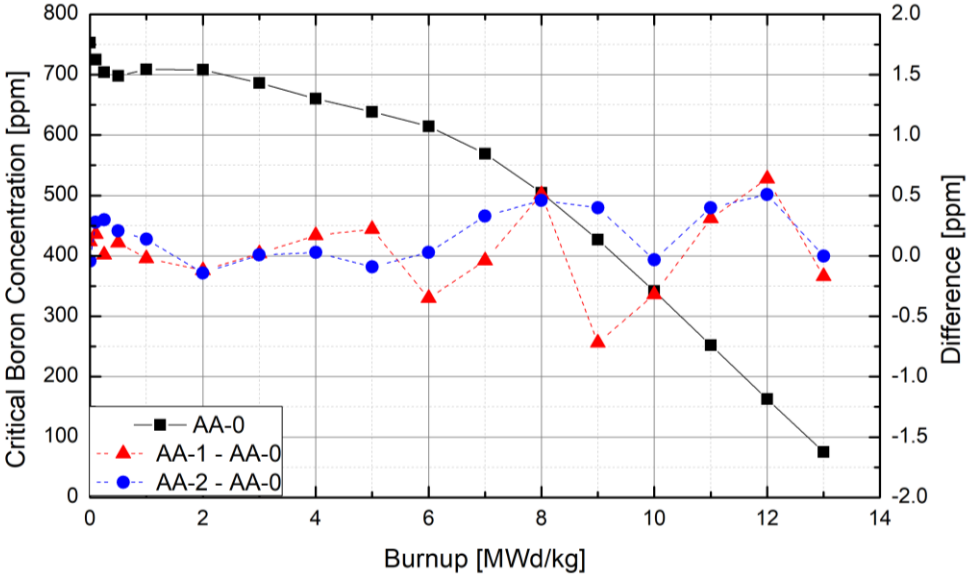

Fig. 3.20: Critical Boron Concentration with core burnup for the OPR1000 problem and the difference in CBC from AA-0 for the AA-1 and AA-2.

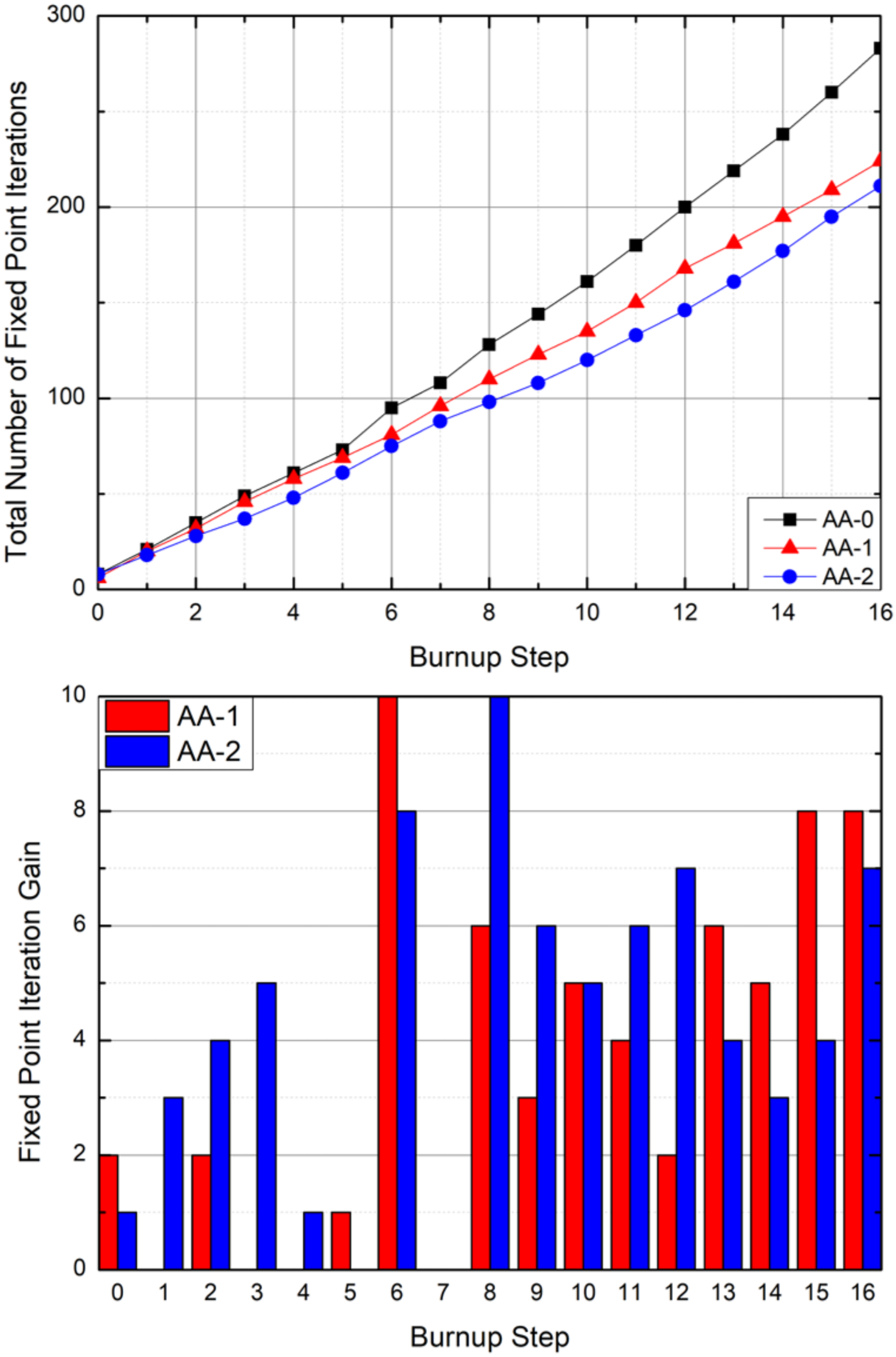

Fig. 3.21: total number of FPIs (top) and total FPI Gain (bottom) for the 1 year depletion calculation of the OPR1000 core.

The depletion calculation time for the OPR1000 core with AA-0 was 2 days 9 hours and 24 minutes (283 FPI). After the application of the acceleration technique with no-rest, this time dropped by 20% for AA-1 and 26% for AA-2. The average time to complete a single depletion step (predictor plus corrector) decreased from 170 minutes of the non-accelerated case to 135 and 126 minutes for AA-1 and AA-2, respectively.

Chapter 4. Analysis of Transient Neutronics-Thermal/Hydraulics Coupled Calculations

The achieved high computing capabilities have eased the computational burden of DWCC. However, the computational resources required for transient DWCC design analyses are still limited and the two-step method with spatial and energy refinement is still essential in industry practical applications.

The traditional two-step core calculation method has been using assembly homogenized group constants (GC) in the analyses of LWRs cores for more than 30 years. This method generates sufficiently accurate pin power distribution results when combined with the pin power reconstruction technique. However, with the enhancement of the computing technology in the recent years, the industrial demand for core analyses with higher accuracy has increased. This led to the rapid development of pin-by-pin core analysis codes like Bamboo [4] or SPHINCS [5], shifting the assembly level core calculation to the pin level core simulation. Moreover, the application of advanced parallelization techniques allows to provide a fast yet accurate solution of transient analyses too.

The nodal methods, which have been conventionally employed in the assembly-wise core analyses, have not shown effectiveness in terms of computing time for pin level core analyses yet. In order to achieve practical computing performance, the FDM has been suggested as a solution. However, the limitation of FDM is that the neutron flux within a pin is assumed to be constant and that the discretization error results still too high compared to nodal methods which employ higher order polynomials or exponentials. In other words, to get an accurate FDM solution intra pin meshes are crucial to alleviate the simplification introduced by linearizing derivative operators. This limitation has been recently overcome by the introduction of specially generated pin homogenized GCs and by carrying out the core analysis with SP_3 method. The results generated from FDM based on SP_3 method agree well with the transport reference solution when the super-homogenization (SPH) factors corrected with the leakage feedback method (LFM) are employed to reproduce the transport calculation results [88].

Transient coupled analyses usually deal with RIA. In general, the types of scenario can be split in two categories according to the velocity of the involved feedback: fast (or prompt) and slow (or delayed) transients. For what concerns fast scenarios such as control rod ejection, the coolant status is generally less important than the fuel temperature one. In fact, in this type of events all the important T/H phenomena occur inside the fuel rod and a refined solver for the moderator would only burden the computational time without providing additional important information. The benefit of using ESCOT rises when simulating slow scenarios, such as loss of power/mass flow, turbine trip or MSLB, because of the enhanced presence of large asymmetry, mixing phenomena or boundary condition variation in rapid times.

In order to optimize the pin level solution and to obtain maximized benefits, the transient coupling of the ESCOT code has been performed with a pin-by-pin FDM SP_3 based code with the final objective of simulating the MSLB scenario administered by Ivanov et al. [22] under the umbrella of the NEA/OECD.

The following section briefly describes the neutronics code employed in the solution of coupled transient scenarios. Section 4.2 details the coupling strategy used to connect the two codes while section 4.3 describes the analysis of the NEA/OECD

MSLB benchmark, with particular focus onto the Exercise II.

4.1 Simplified P_3 based neutronics solver

In order to simulate a reactor core using 3D SP_3 equations, a methodology called direct calculation with multi-level CMFD acceleration has been explored and successfully developed by Hwang J. T. in his M.Sc. dissertation [21] to solve transient problems with high computing efficiency retaining the accuracy.

In this methodology, the 3D problem is decomposed into multiple pin-wise 1D FDM problems along the axial direction. Since the problem of 1D FDM can be solved directly by the forward/backward substitution, the feasible performance in terms of computing time is achieved with limited resources. Also, with axially fine mesh structure, the fission distribution along the axial direction is more accurately calculated. The direct calculation is then coupled with two levels of 3D CMFD acceleration. The first one is the application of pin level CMFD acceleration based on SP_3 equations while the second one is the application of assembly-level 3D CMFD acceleration based on diffusion theory (P_1). The code has its own simplified T/H module which is for closed channel and implies no pressure drops. Fig. 4.1 shows the calculation flow of the code for the steady-state (*top*) and transient (*bottom*) cases. In case of transient calculations, a conditional update has been implemented for a small variation of the transport cross section (default value $\Delta\Sigma_{tr} / \Sigma_{tr} > 0.1\%$).

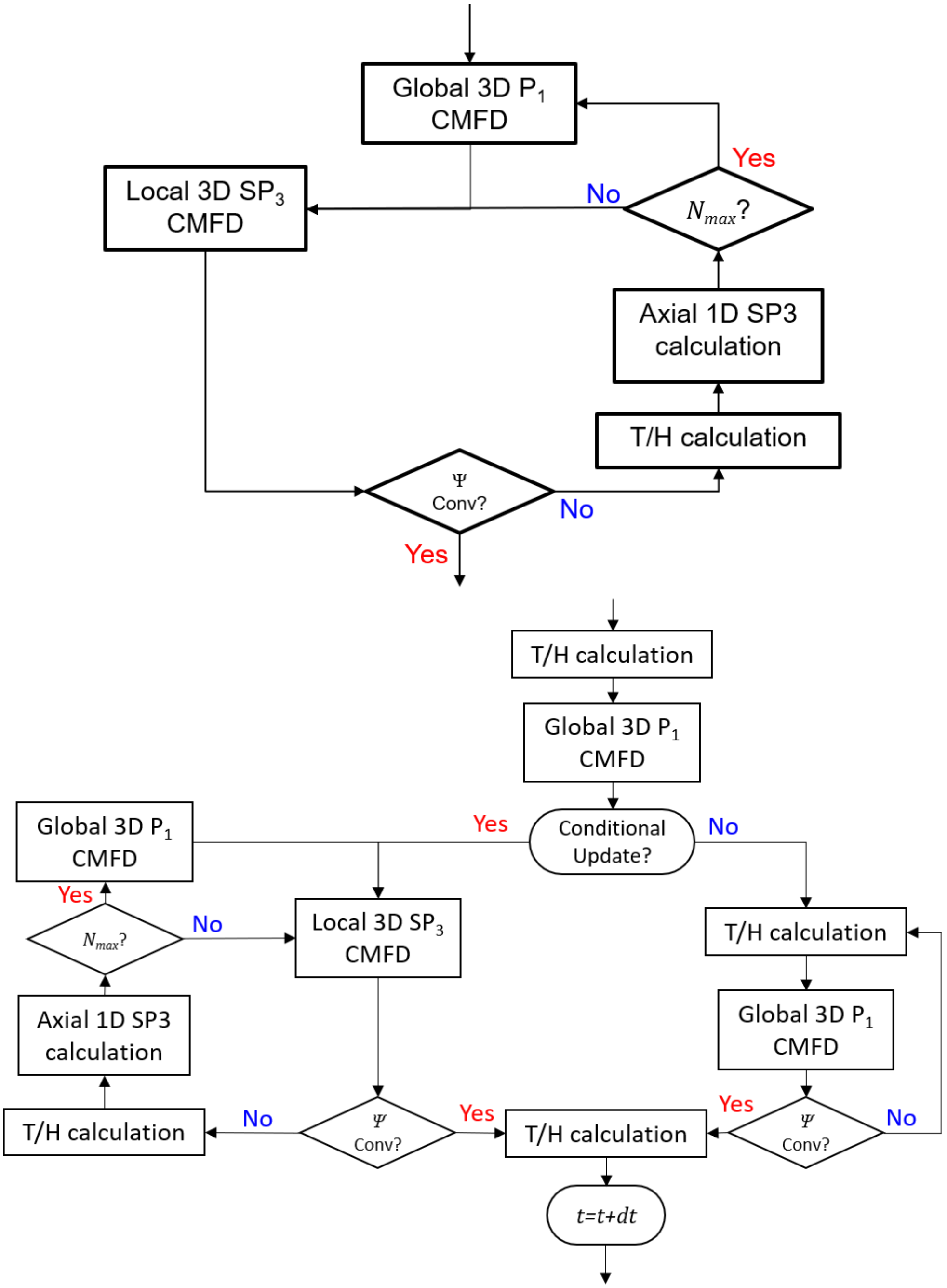

Fig. 4.1: calculation flow for the 3D/1D based SP$_3$ code, steady-state (*top*) and transient (*bottom*).

The code is highly parallelized with MPI. In particular, the calculation of the local and global 3D CMFD is parallelized following the basic scheme of axial domain decomposition while the axial solution is radially parallelized.

A more detailed description of the employed models, the verification, the parallel scheme and performances is provided in Hwang J. T. M.Sc. thesis [21].

4.2 Transient neutronics-T/H coupling

ESCOT and the neutronics transient solver introduced in the previous subsection have been directly coupled since they share the same parallelism (they are both MPI parallelized). In order to use both codes at their best, the MPI capability of splitting the communicator is employed. In this way, the ESCOT code can run using the assembly-wise domain decomposition scheme while the neutronics performs its calculation with planar-wise decomposition. Fig. 4.2 details the general scheme of the applied parallelization topology.

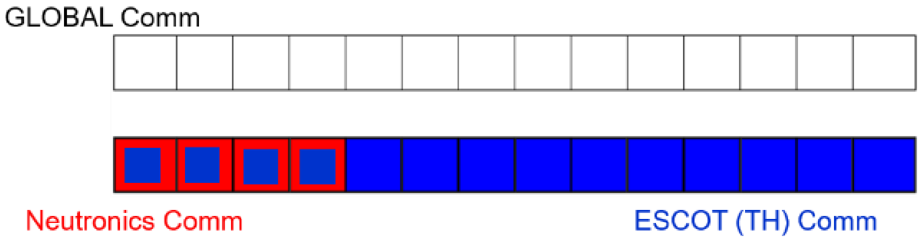

Fig. 4.2: coupling topology between the neutronics solver and the ESCOT code.

Moreover, the parameters necessary to have a complete solution of a coupled neutronics-T/H problem are: the power, the fuel temperature, the moderator temperature and the moderator density. In the transient coupling, the moderator properties change slower than the fuel temperature. Therefore, for transient coupled calculations, the FPI problem within the same time-step can be solved by only calculating the fuel temperature and by performing the entire ESCOT T/H calculation after the fission source has converged and just before starting the new time-step.

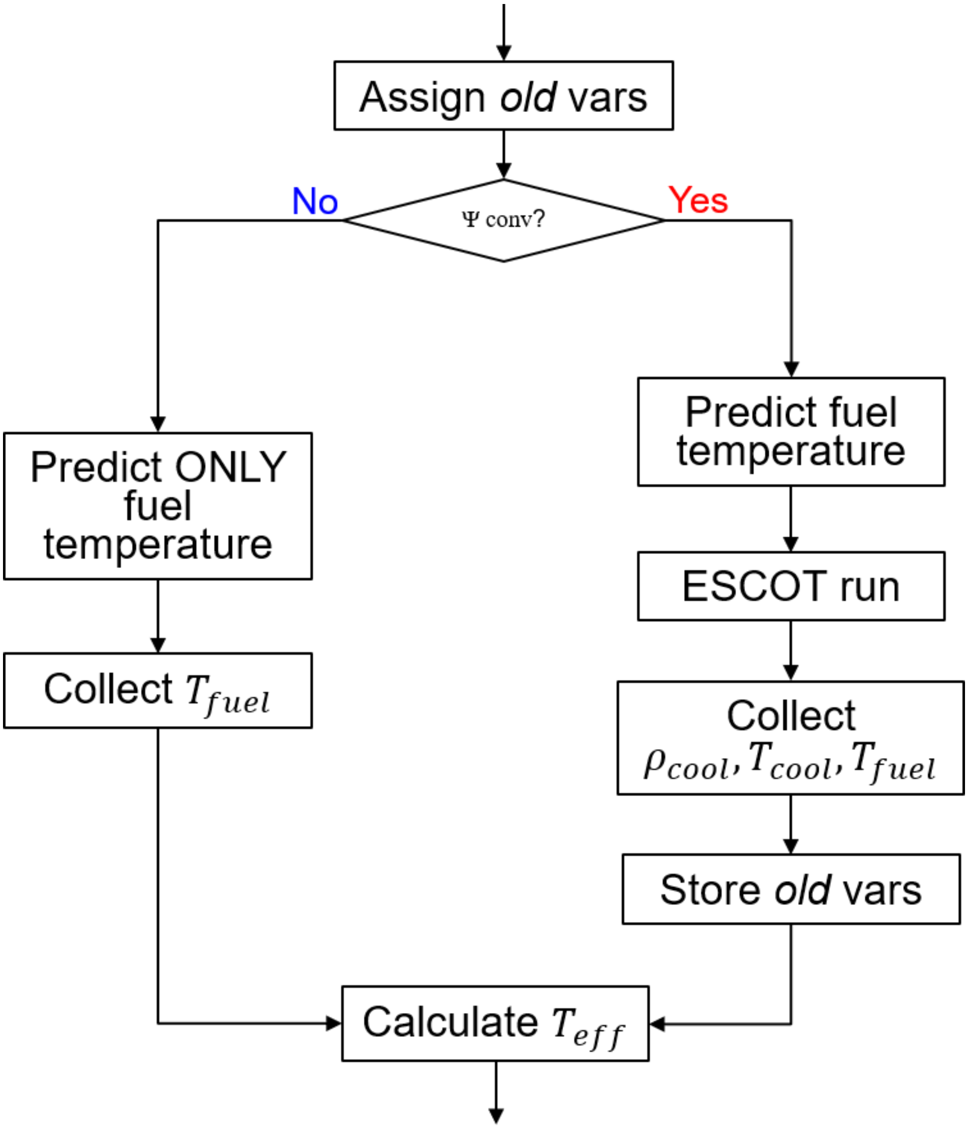

Fig. 4.3: ESCOT coupling interface for transient solutions.

4.3 Analysis of the NEA/OECD MSLB benchmark

The main steam line break (MSLB) accident postulated in PWR safety analyses involves a considerable reduction of the inlet coolant temperature of one side of the reactor core which causes a considerable asymmetry in the radial flow conditions. Because of this asymmetry, the positive reactivity feedback effect introduced by the decrease of the coolant temperature appears non-uniform. Additionally, a stuck rod on the cold side is considered during the reactor SCRAM for conservatism in the analysis.

The Nuclear Energy Agency of the Organization for Economic Cooperation and Development administered a three-exercise benchmark problem in order to assess the numerous coupled neutronics-T/H codes. The first and second exercise correspond to the standard design methodology [22]. Initially, the reactor primary system is simulated using point kinetics and the boundary conditions of to the core are stored. Then, a more refined neutronics-T/H solver for just the core is employed using the previously stored boundary conditions. Historically, the simulation of this accident is performed at the end of cycle (EOC) when the moderator temperature reactivity coefficient (MTC) is very close to zero (or slightly positive) the CBC is almost null. In general, the results for the first exercise are return-to-power and criticality while for the second exercise, using the stored set of BCs, the return-to-power and criticality do not occur. The NEA/OECD MSLB benchmark added a third analysis in which the system code and the refined core solver had to be coupled and the entire scenario had to be simulated all together [22].

This section is devoted to the solution of the Exercise II which deals only with the core level phenomena and does not require system modeling since a set of time-dependent boundary conditions is provided by the benchmark administrators. The next section describes the MSLB scenario in a general way providing the global behavior of a two-loop PWR core while section 4.3.2 shows the solution of the Exercise II of the NEA/OECD MSLB benchmark.

4.3.1 Description of the scenario

A two-loop PWR scheme is shown inside Fig. 4.4 together with the sign of rupture in one of the loops.

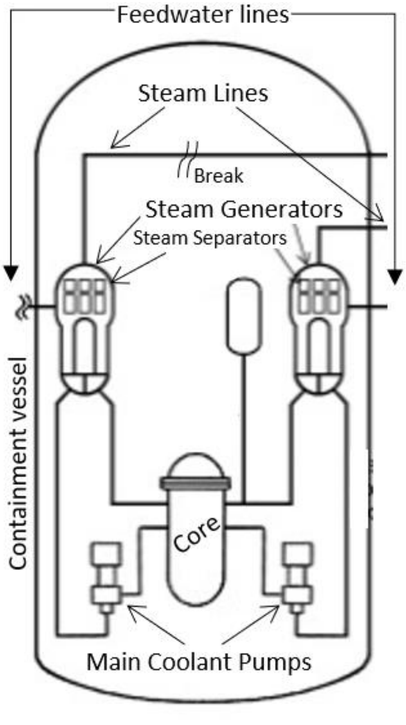

Fig. 4.4: two-loop PWR primary system diagram with one steam line rupture.

When this scenario occurs, the first reaction of the primary side is an almost instantaneous exchange of heat to respond to the blowdown of the broken secondary side. This event triggers a depressurization of the primary loop. This pressure wave travels at speed of sound in the primary loop and provokes a fast decrease in moderator density which induces an initial decrease of the core power. With a delay of 3-5 seconds, the chilled water that has initially decreased its temperature to absorb the rapid evaporation of the secondary side reaches the reactor core and the power starts to grow back up because of the insertion of positive reactivity caused by a lower moderator temperature. Then, the high core power signal starts the SCRAM. Fig. 4.5, Fig. 4.6 and Fig. 4.7 show the trend of the two sides core outlet pressure and inlet coolant temperature, the core power and reactivity evolution. Being one of the control rod stuck out, the power may increase up and have the so called return-to-power if the SCRAM worth is not big enough to balance the subcritical source multiplication. After 50-60 seconds, the secondary side of the steam generator dries out and the temperature of the primary side coolant temperature (the broken side) starts to grow up again as Fig. 4.6 shows around 57*sec* with a consequent delayed insertion of negative reactivity in the core as Fig. 4.18 shows after about 60*sec*.

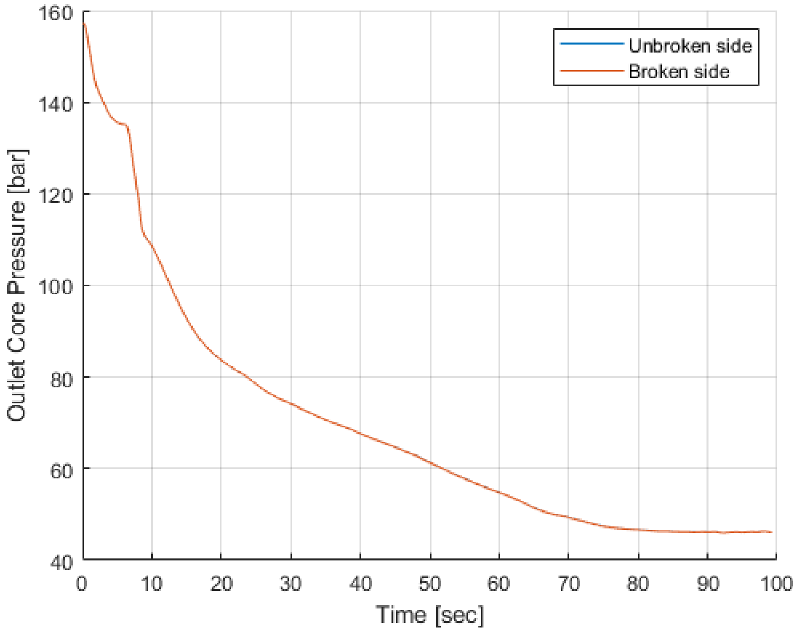

Fig. 4.5: average outlet pressures for both sides of the reactor core.

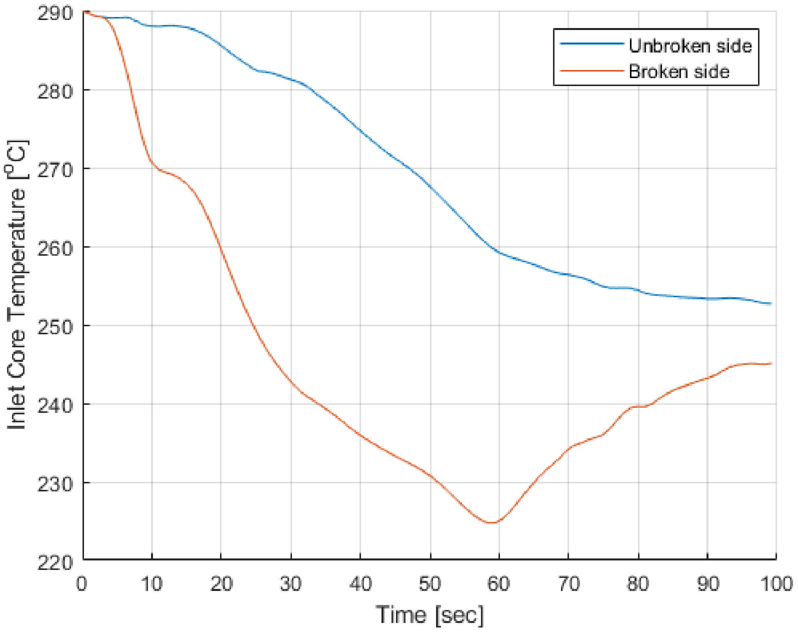

Fig. 4.6: average inlet coolant temperature for both sides of the reactor core.

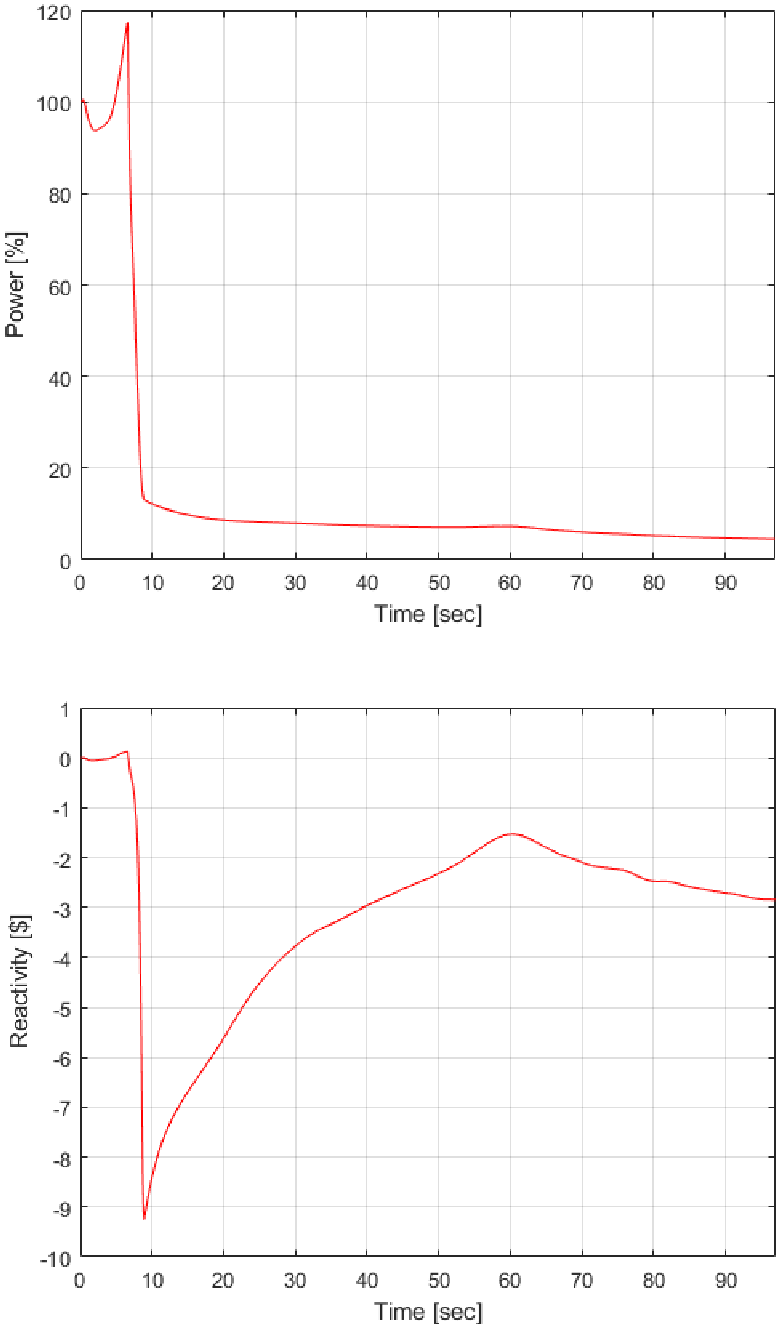

Fig. 4.7: general power (*top*) and reactivity (*bottom*) evolution during the MSLB scenario.

4.3.2 Solution of the NEA/OECD MSLB benchmark exercise II

The reactor core used for the MSLB Benchmark is based on the same model of the Three Mile Island one, with 241 assemblies of which 177 are 15*x*15 FA and a total power of 2,772MW_{th}. Two sets of eighteen boundary conditions (BC) at 171 time-steps were provided for inlet temperature, inlet mass flow and outlet pressure according to the radial mapping provided inside Fig. 4.8.

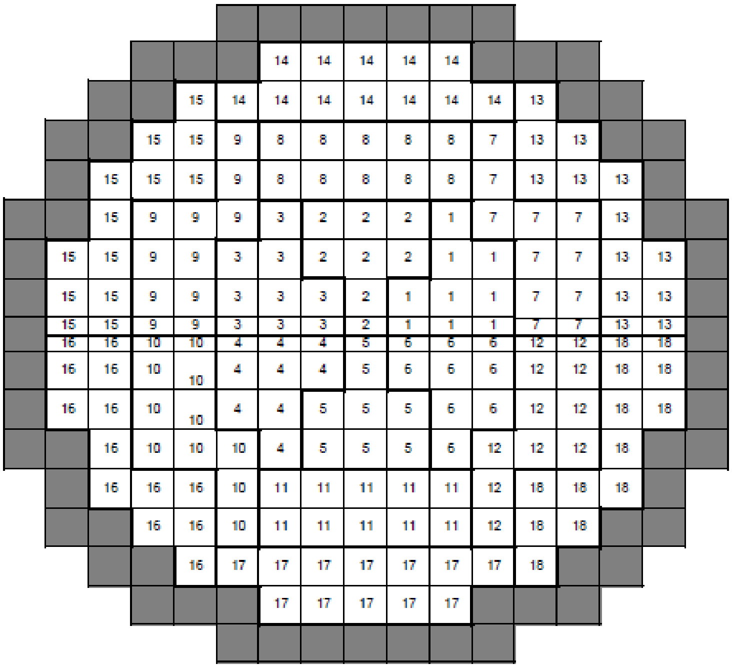

Fig. 4.8: radial mapping for the 18 core sectors.

The simulation of this transient covers a time of about 100 seconds. In this simulation, the reactor trip occurs at 6.65 seconds with a speed of 155.71*cm/sec*. The core model has eight banks of control rods of which seven are explicitly modeled with a specific cross section file (1 to 7), while the last bank is modeled implicitly. As previously mentioned, one rod on the cold side is stuck out during this calculation (steady-state and transient). Its position is provided inside Fig. 4.9 which also shows the radial mapping of the eight control rod banks. The initial position of every control rod bank is fully extracted except bank 7 which is 90% withdrawn.

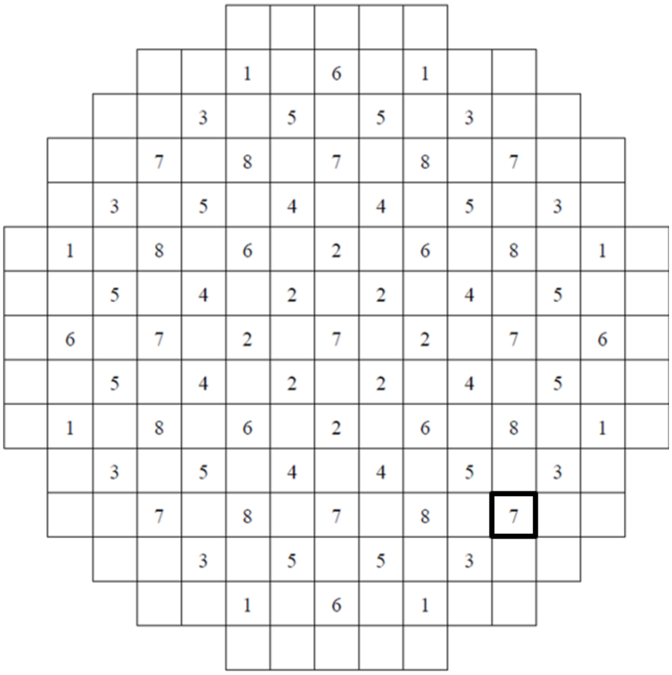

Fig. 4.9: radial mapping of the eight control rod banks.

Together with the sets of BCs, one set of 438 unrodded and two sets of 195 rodded compositions were also provided to solve this problem. These sets of cross sections (XS) were calculated assuming the core at 650 Effective Full Power Days, 5*ppm* of boron and thirty branches including five effective fuel temperature points and six moderator density points.

These two combined sets of BCs and XSs will be called *No Return-to-power* (NoRP) and *Return-to-power* (RP). In the first case, the fission power is expected to diminish to zero after the SCRAM while in the second one the return of fission power is expected.

In order to assess the two XSs library files, the calculation of the SCRAM worth was in order. This parameter is defined as a combination of two hot zero power (HZP) eigenvalues:

$$\frac{dk}{k}\left[\%\right] = \frac{k_{ARI} - k_{ARO}}{k_{ARI}k_{ARO}} \cdot 100\,, \tag{4.1}$$

where *ARI* stands for *All Rod In* and *ARO* for *All Rod Out*. In case of the *ARI* the stuck rod is left blocked out of the core. The results are shown inside Tab. 4.1 together with a comparison with MASTER/COBRA and with the hot full power (HFP) *k-eff* calculated for the initial steady-state conditions [89]. The eigenvalue calculated with 3D1D/ESCOT was 1.00647 while for MASTER/COBRA was 1.00721. The difference is mainly due to a better nodalization of the of the neutronics and the T/H, while a difference of 0.35% in the SCRAM worth was found in the case of Return-to-power (-3.37% and -3.02%). In addition, the SCRAM worth for the NoRP case was also computed and resulted equal to -4.84%.

Tab. 4.1: summary of the steady-state parameters for the analysis of the Exercise II.

Code	**No Return-to-power**		**Return-to-power**	
	SCRAM Worth *dk/k* [%]	HFP k-eff	SCRAM Worth *dk/k* [%]	HFP k-eff
3D1D/ESCOT	-4.84	1.00647	-3.37	1.00647
MASTER/COBRA 18 Channels	-	-	-3.02	1.00723

The following two sections describe the analysis of the two sets of BC and XS. A comparison between the global tendency of power and reactivity will be shown in the RP case with a previous analysis performed with MASTER/COBRA [89]. This benchmark problem was formulated to validate assembly-wise solvers but here a pin-wise solver is used to analyze the scenario. Thus, the sets of XSs provided in the benchmark have been assigned assembly-wise while the feedbacks have been calculated pin-wise. The number of axial meshes was kept equal to the one recommended in the benchmark $Z = 26$. Some of the calculation conditions in which this analysis has been performed are provided inside Tab. 4.2.

Tab. 4.2: summary of the calculation conditions for the NEA/OECD MSLB benchmark Exercise II

Time-step size [sec]	0.1
# of Time-steps	970
Ψ convergence criterion	10^{-6}
Conditional Update [%]	0.1
Decay Heat Model	Dunn Model [90]
# of MPI processes	177 (26 planes / 177 FA)

4.3.2.1 No return-to-power

The first analysis concerned the set of BCs and XSs which must not trigger any return of fission power. The evolution of power and reactivity are shown inside Fig. 4.10 and Fig. 4.11. The fission power after the SCRAM does not grow up and it slowly diminishes until it becomes practically zero around 100*sec*. However, the presence of a stuck rod produces a reactivity increase after the SCRAM but in this case the SCRAM worth is high enough to avoid return-to-power and criticality.

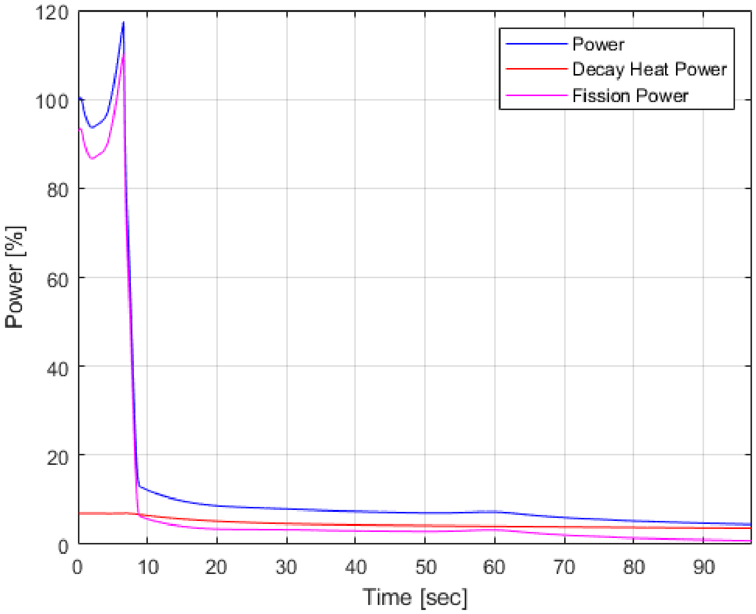

Fig. 4.10: evolution of total, fission and decay heat power during the transient for the NoRP case.

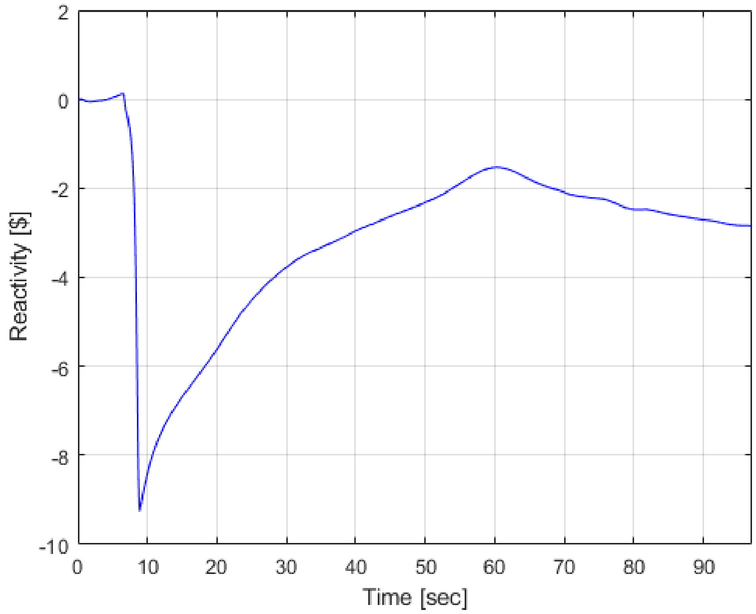

Fig. 4.11: evolution of the reactivity during the transient for the NoRP case.

The main advantage of this analysis is that is conducted at pin level. In fact, access to intra-assembly information was not possible before but now the pin-by-pin 2D axially integrated power is accessible as well as the coolant temperature distribution. Fig. 4.12, Fig. 4.13 and Fig. 4.14 show the 2D axially integrated power for three important time-steps, the initial one, the one just before the reactor trip and the one corresponding to the maximum reactivity level after the SCRAM. The strong asymmetry introduced by the stuck rod is clearly shown by Fig. 4.14.

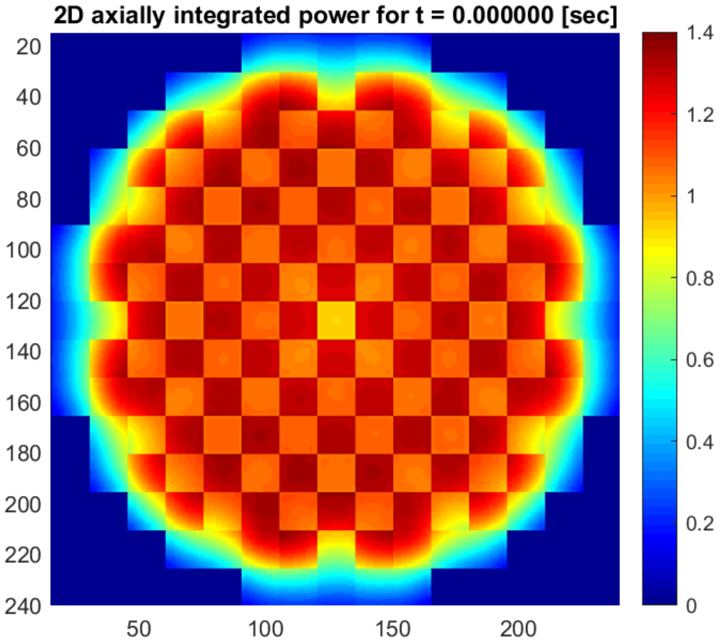

Fig. 4.12: 2D axially integrated power for the NoRP case at 0.0*sec*.

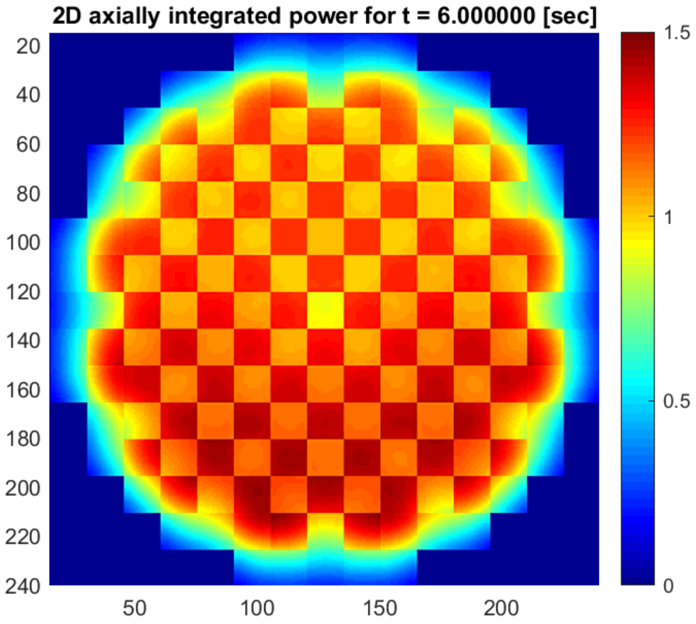

Fig. 4.13: 2D axially integrated power just before the SCRAM (t = 6.0*sec*) for the NoRP.

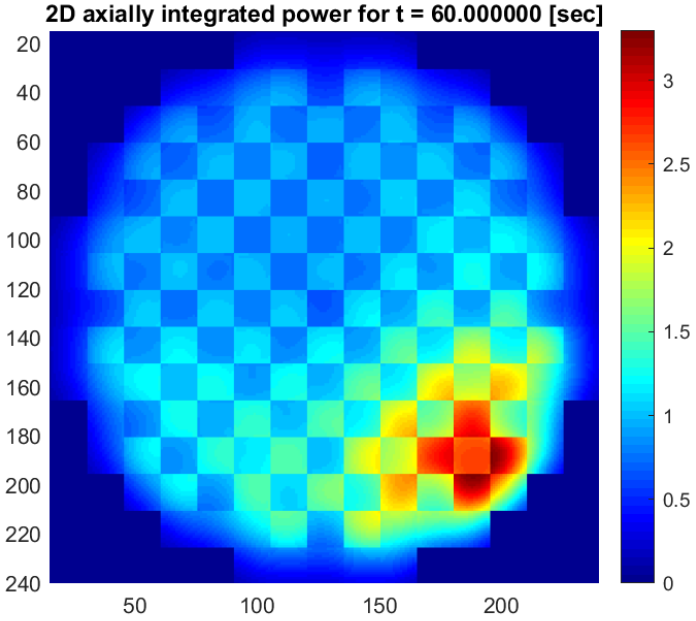

Fig. 4.14: 2D axially integrated power at the instant of maximum reactivity after the SCRAM (t = 60.0*sec*) for the NoRP case.

Moreover, the coolant temperature is depicted in Fig. 4.15, Fig. 4.16 and Fig. 4.17 for the same time-steps. In particular, the mixing effects for the two halves of the core are constrained to only the central assemblies and do not spread towards the others. The good design of the SCRAM system clearly shows that the power around the stuck rod does not trigger a higher increase of the coolant temperature.

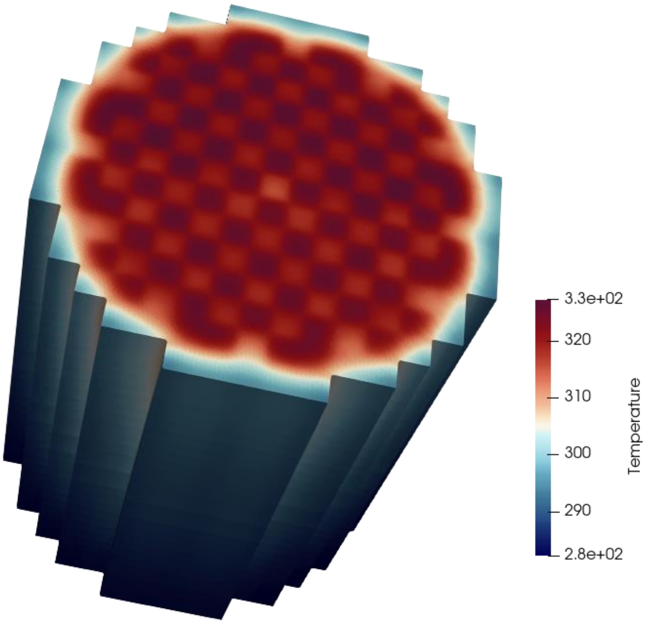

Fig. 4.15: coolant temperature distribution at $t = 0.0sec$ for the NoRP case.

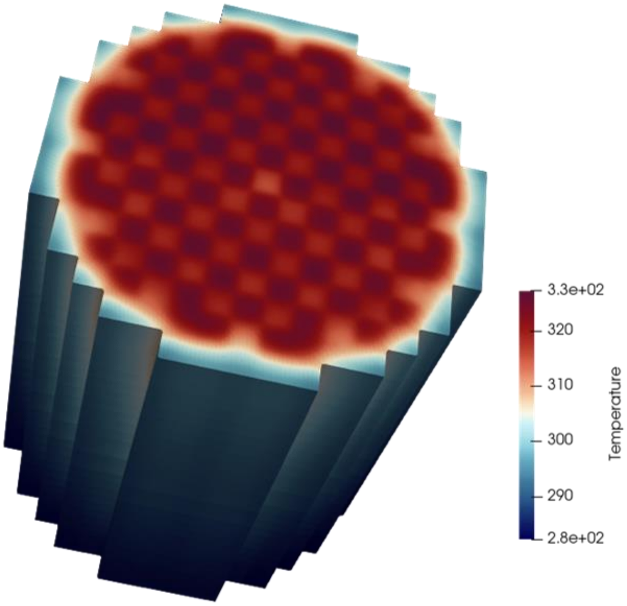

Fig. 4.16: coolant temperature distribution at $t = 6.0sec$ (just before the SCRAM) for the NoRP case.

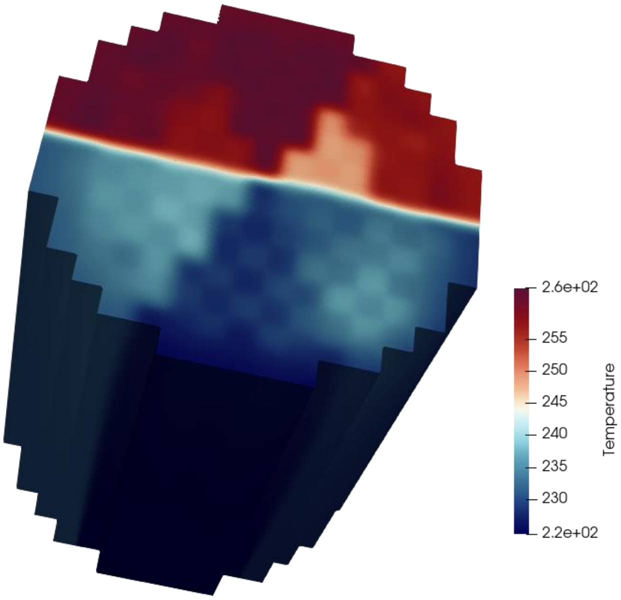

Fig. 4.17: coolant temperature distribution at $t = 60.0sec$ (the instant in which the reactivity is maximum after the SCRAM) for the NoRP case.

4.3.2.2 Return-to-power

As previously mentioned, this case has been used to verify the accuracy of this new solver, the evolution of the global variables has been compared with a solution obtained with MASTER/COBRA in which the assembly-wise solution was computed [89] and with the official statistical analysis performed by the benchmark administrators [91]. The power and reactivity trends match well with the ones calculated with MASTER/COBRA as Fig. 4.18 shows. Furthermore, the power calculated by the pin level solvers goes outside the statistical error given by the by the benchmark administrators between 20*sec* and 70*sec* (see Fig. 4.19). It turned out that the maximum return-to-power for 3D1D/ESCOT occurs at 57.800*sec* with a registered value of 30.9% while for MASTER/COBRA occurs at 57.790*sec* with a measured value of 32.9%; the maximum reactivity after the reactor trip reached -0.06 at 55.900*sec* while the calculated one with MASTER/COBRA was -0.03 at 55.475*sec*. The two main reasons why these differences occur can be found in:

- a higher SCRAM worth of the pin level solver,
- a better interpretation of the mixing with a consequent higher coolant temperature, and
- a better nodalization of the neutronics and T/H.

Another important safety parameter is shown in Fig. 4.20 which depicts the evolution of the minimum DNB ratio (MDNBR), calculated using both the default option of ESCOT and the Groeneveld lookup tables (see section 2.7), normalized to the steady-state values (2.35 and 2.92). During the entire scenario, the MDNBR always remains above 2.

The return-to-power can be clearly seen in Fig. 4.21. In this case, the fission power after the reactor trip does not disappear but it increases (return-to-power) until a maximum value which occurs with a small delay respect to the minimum inlet temperature. However, in this simulated case the return-to-criticality is averted. This behavior can be described by the source subcritical multiplication phenomenon. A summary of the global parameters and a comparison between the two analyses is provided inside Tab. 4.3.

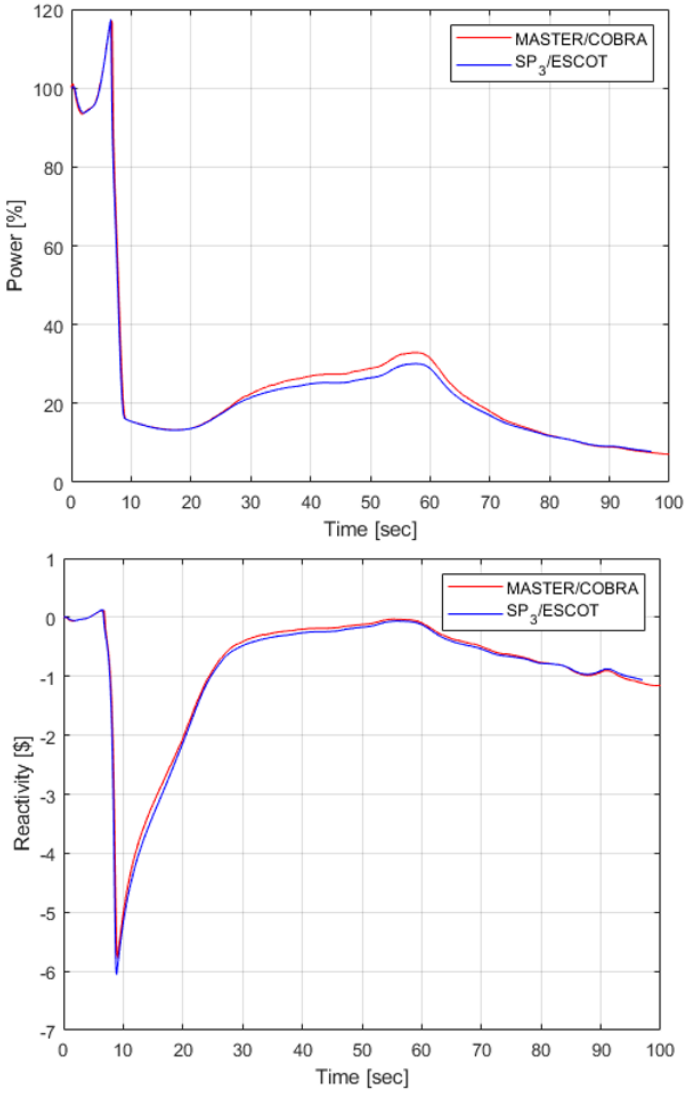

Fig. 4.18: evolution of power (*top*) and reactivity (*bottom*) during the transient calculated with MASTER/COBRA and the 3D/1D SP$_3$ code coupled with ESCOT.

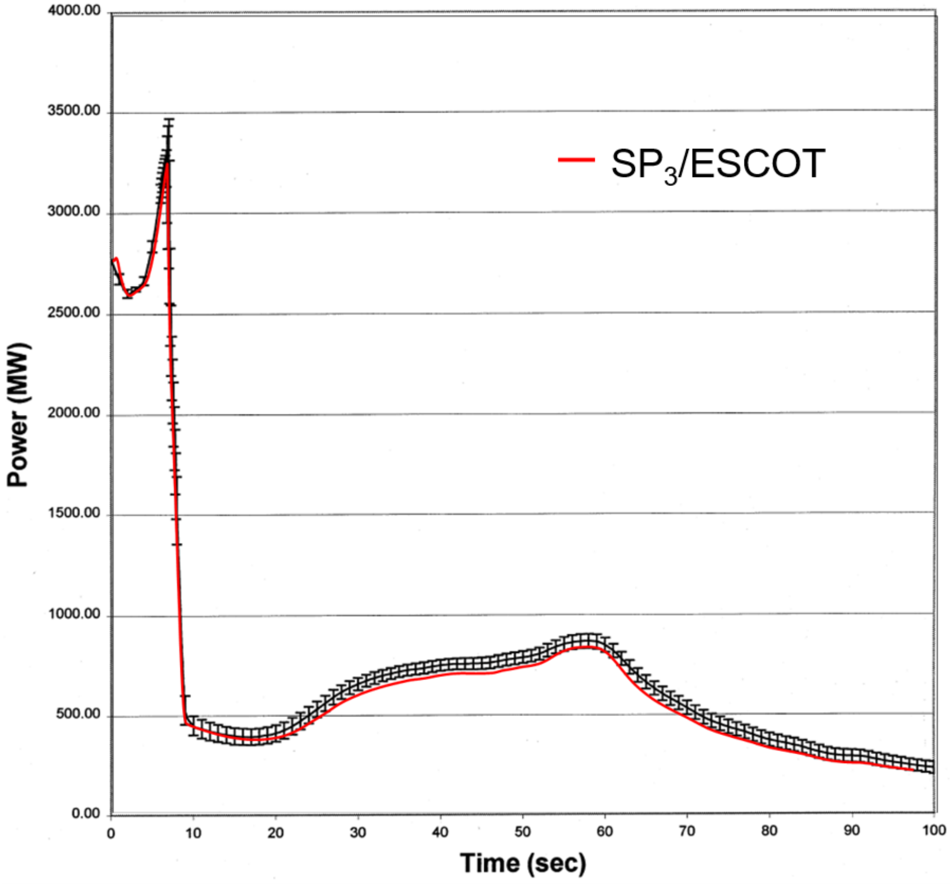

Fig. 4.19: comparison of the total reactor power evolution between the one provided by the benchmark administrators [91] and the one calculated by the pin-by-pin solver.

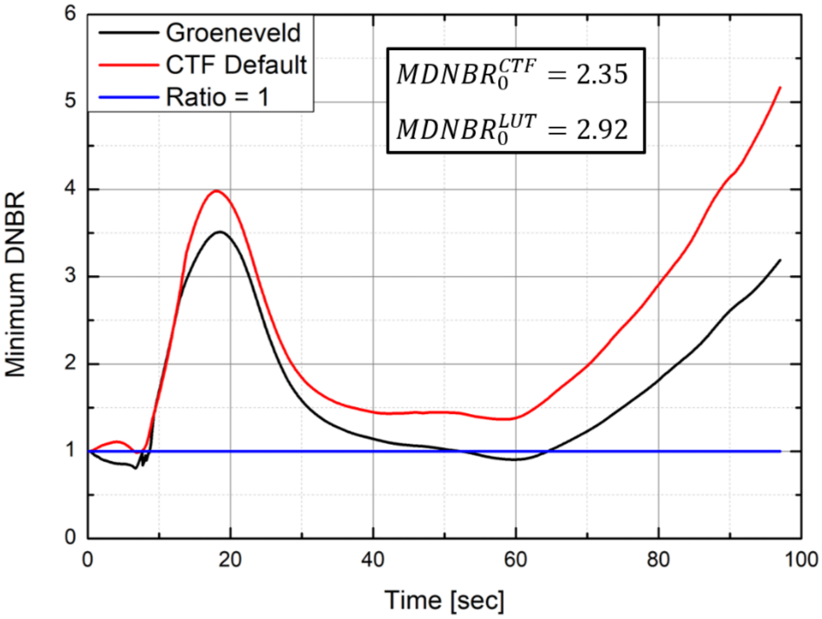

Fig. 4.20: evolution of the normalized MDNBR for the RP cases applying the CTF scheme and the Groeneveld lookup tables for the calculation of the CHF.

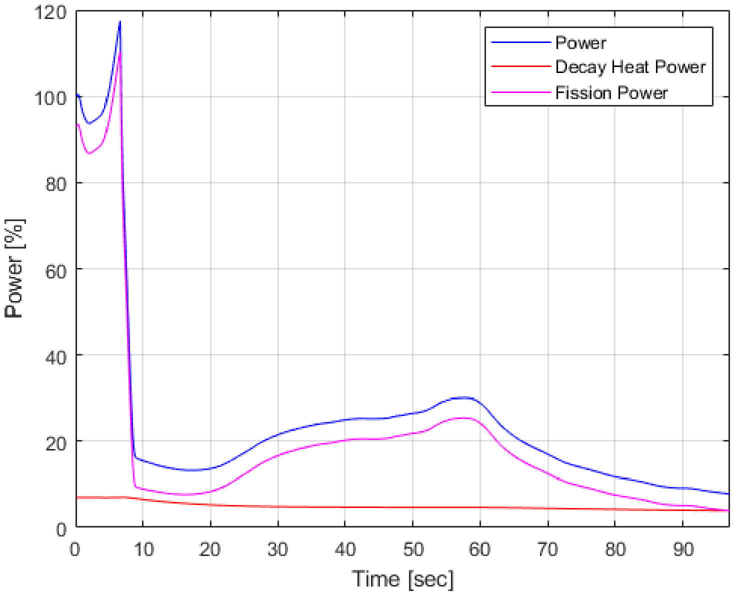

Fig. 4.21: evolution of total, fission and decay heat power during the transient for the NoRP case.

Tab. 4.3: summary of the global parameter for the RP case and comparison with MASTER/COBRA.

	3D1D/ESCOT	MASTER/COBRA
Time of MAX. Return-to-power [sec]	57.800	57.790
MAX. Return-to-power [%]	30.90	32.90
Time of MAX. Reactivity after the SCRAM [sec]	55.900	55.475
MAX. Reactivity after the SCRAM [$]	-0.06	-0.03
Power at 97.0 seconds [%]	7.80	7.55

As it was done for the NoRP, the intra-pin distribution of 2D axially integrated power and the coolant temperature maps are here plotted together with the coolant density. In addition, cropped maps of coolant temperature and density are in order to better show the high asymmetry introduced in this calculation. The steady-state power map is plotted in Fig. 4.22. Fig. 4.23 depicts the power map just before the reactor trip ($t = 6.0sec$) while the power distribution at the maximum return-to-power instant is shown in Fig. 4.24 (t = 58.0sec). The maximum pin power at 58.0sec is above 3.5.

In addition, the assembly-wise power provided by the benchmark administrator at the time of maximum return-to-power is shown inside Fig. 4.25 [91]. The difference between the pin-wise power and the assembly-wise power is very high for assemblies that contain a high power gradient. The absolute difference between the power calculated by the 3D1D/ESCOT and the one found inside the work of Taylor et al. [91] is depicted inside Fig. 4.26. The maximum and minimum difference correspond to 127% and -119% and they are located inside a peripheral assembly next to the stuck. This assembly, in fact, contains a big flux gradient since the top internal side is in contact with the highest flux pins while the outermost pins face the radial reflector and *i.e.* a lower neutron flux.

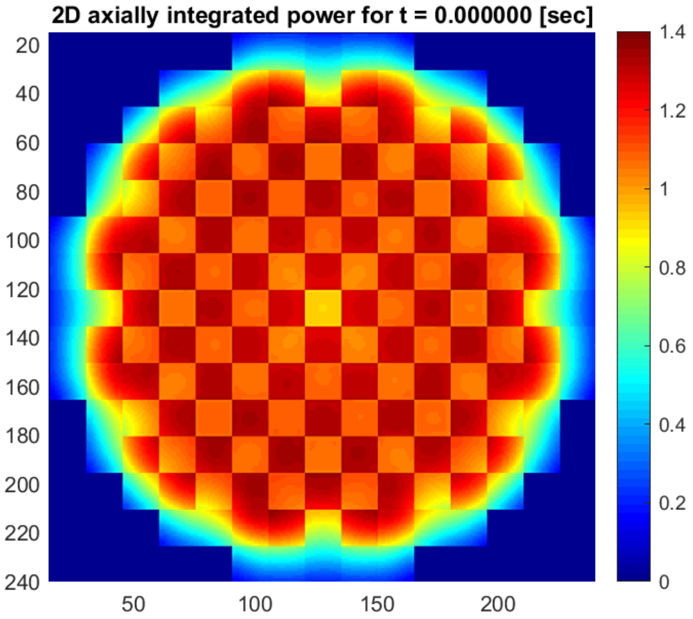

Fig. 4.22: 2D axially integrated power at t = 0.0*sec* for the RP case.

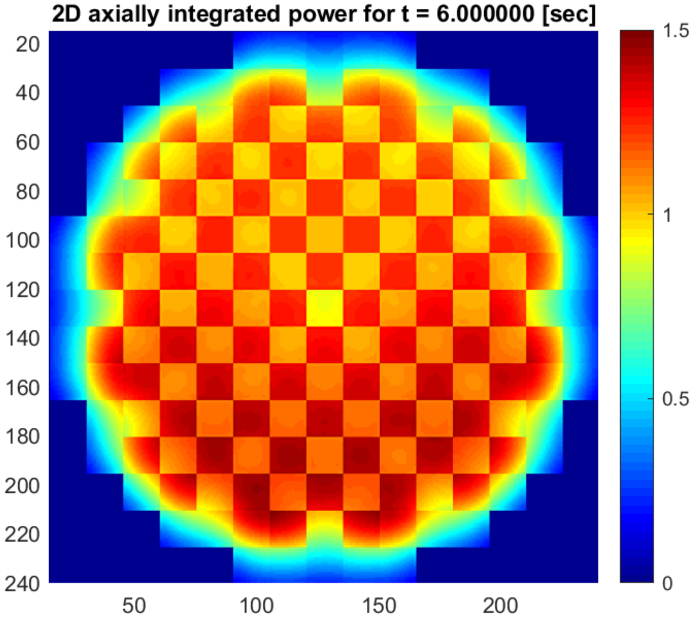

Fig. 4.23: 2D axially integrated power at t = 6.0*sec* (just before SCRAM) for the RP case.

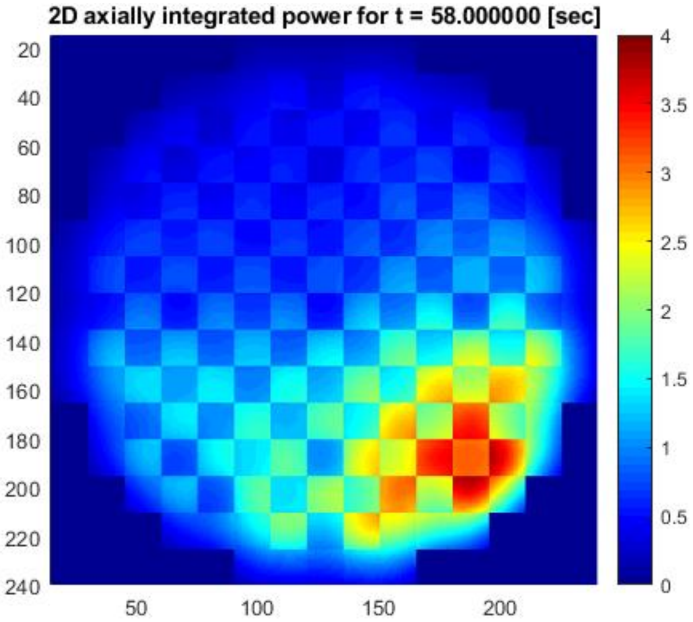

Fig. 4.24: 2D axially integrated power just before the maximum return-to-power instant (t = 58.0*sec*) for the RP case.

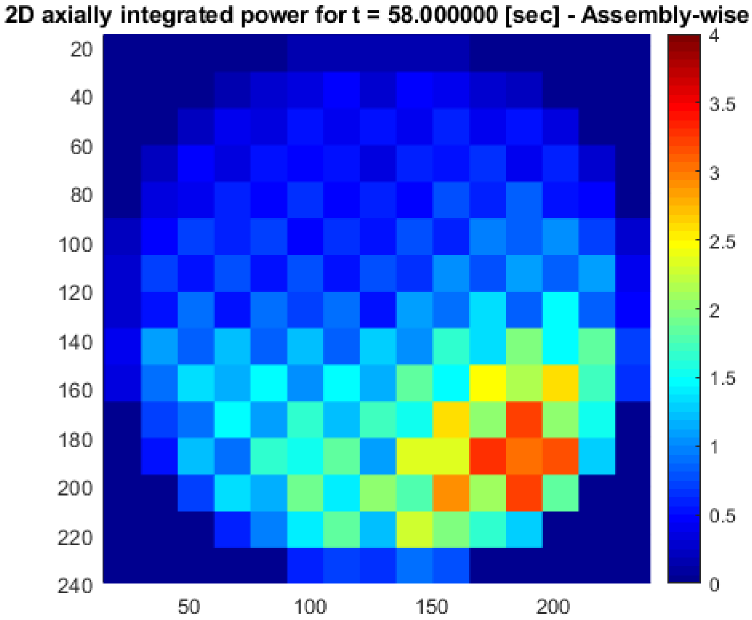

Fig. 4.25: assembly-wise 2D axially integrated power at the instant of maximum return-to-power (t = 58.0*sec*) [91].

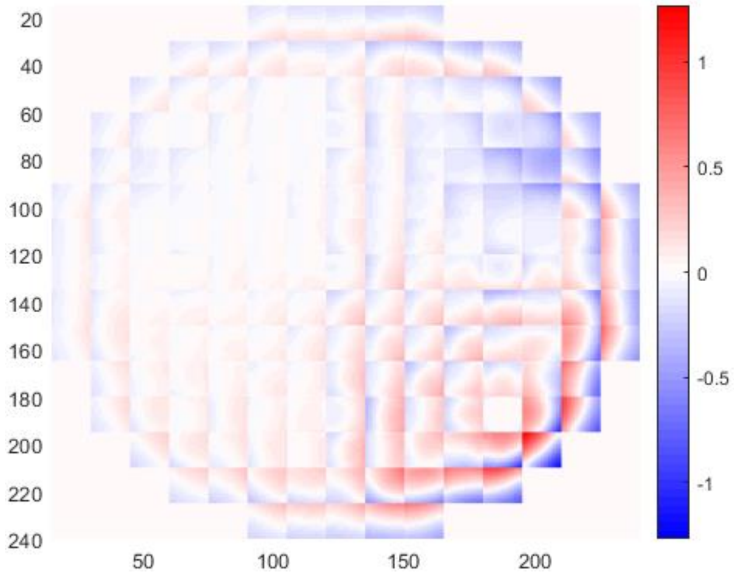

Fig. 4.26: absolute difference between the 2D axially integrated power calculated with 3D1D/ESCOT and the one provided by the benchmark administrators in [91] at t = 58.0*sec*.

The outlet coolant temperature at the beginning of the transient is shown inside Fig. 4.27 while Fig. 4.28 illustrates the coolant outlet temperature just before the SCRAM (t = 6.0*sec*). However, these two pictures do not differ that much from the ones previously shown for the analysis of the NoRP case since the control rods are almost fully withdrawn and the main difference (*i.e.* the SCRAM worth) do not interfere.

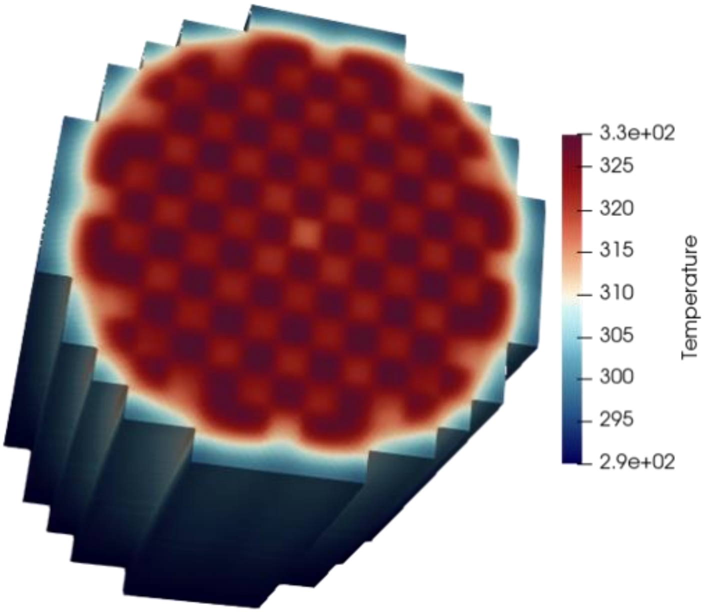

Fig. 4.27: coolant temperature distribution at t = 0.0*sec* for the RP case.

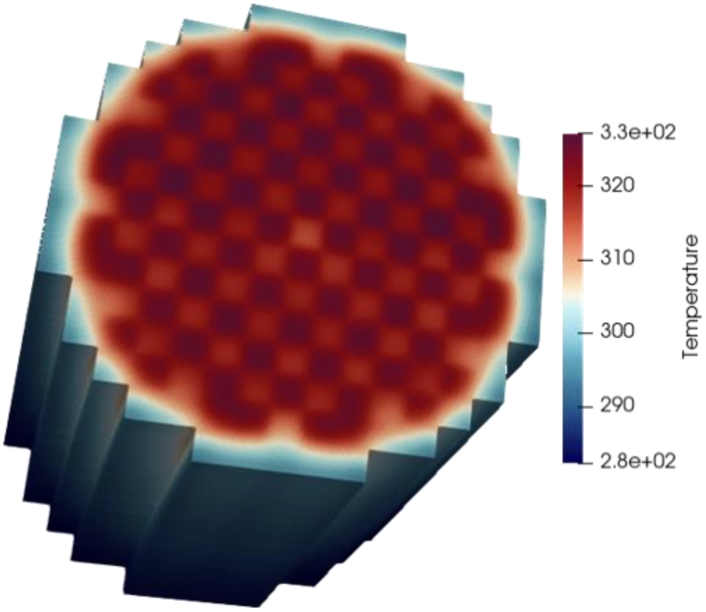

Fig. 4.28: coolant temperature distribution at t = 6.0*sec* (just before the SCRAM) for the RP case.

Fig. 4.29 and Fig. 4.30 are of more interest because they show the combined effect of the bad design of the SCRAM together with the peculiarity of this accident. In fact, in this case the coolant temperature around the stuck rod is higher than the one presented in the Fig. 4.17. Moreover, the cropped coolant temperature map shows clearly the confinement of the mixing effect to the central assembly and a slight increase in its size with the axial level, the higher the position the higher is the mixing. Similar behavior is shown for the coolant density inside Fig. 4.31 and Fig. 4.32.

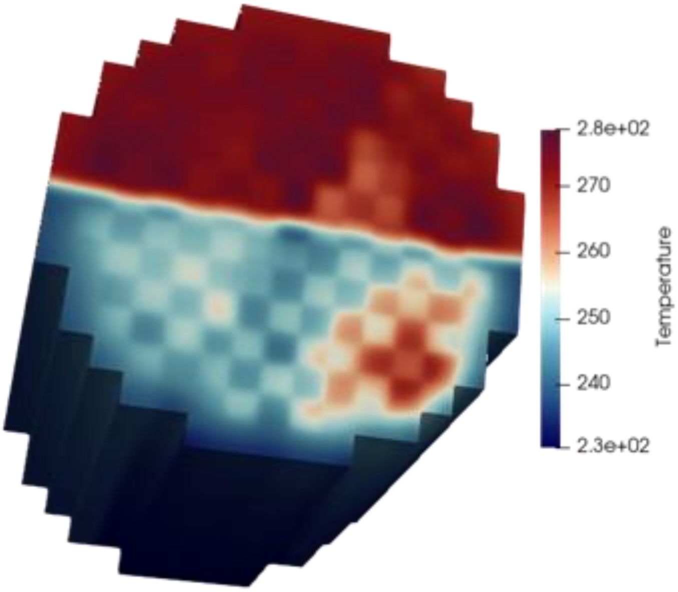

Fig. 4.29: coolant temperature distribution at $t = 58.0 sec$ (at the maximum return-to-power) for the RP case.

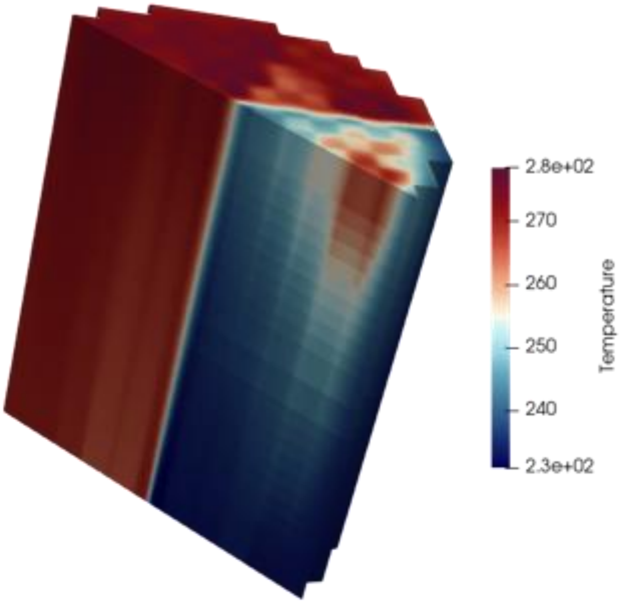

Fig. 4.30: cropped coolant temperature distribution at *t* = 58.0*sec* (at the maximum return-to-power) for the RP case.

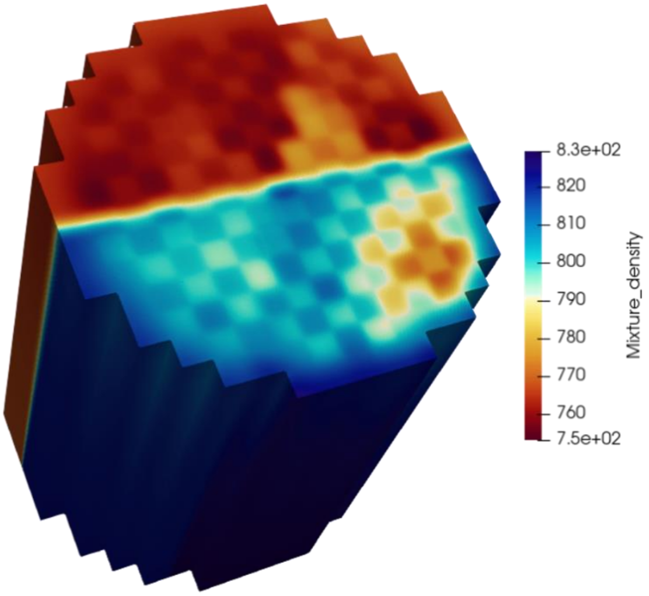

Fig. 4.31: coolant density distribution at *t* = 58.0*sec* (at the maximum return-to-power) for the RP case.

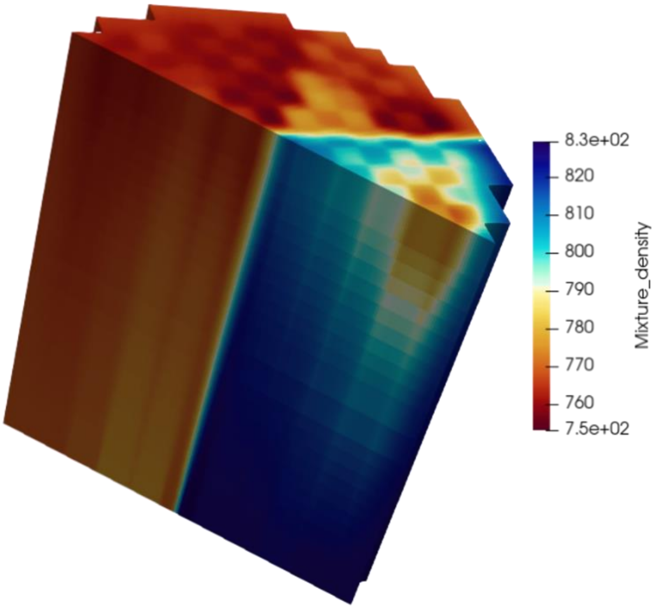

Fig. 4.32: cropped coolant density distribution at t = 58.0*sec* (at the maximum return-to-power) for the RP case.

This pin level analysis allowed to calculate the DNBR in each channel and to analyze its evolution with time. The minimum DNBR occurs at Z = ~3.3*m*. Therefore, the DNBR distribution at t = 0*sec* and t = 58*sec* for the entire axial level Z = 3.3*m* is shown inside Fig. 4.33 and Fig. 4.34. However, the three-dimensionality of this problem requires the plotting of this pin level parameter also for two more cross sections both through the stuck rod. Fig. 4.35 and Fig. 4.36 depict the DNBR at t = 0*sec* and t = 58*sec* when the reactor core is cut only in the cold side while Fig. 4.37 and Fig. 4.38 depict the DNBR at the same instants in the case of a cut through the other direction when both the hot and cold side are shown.

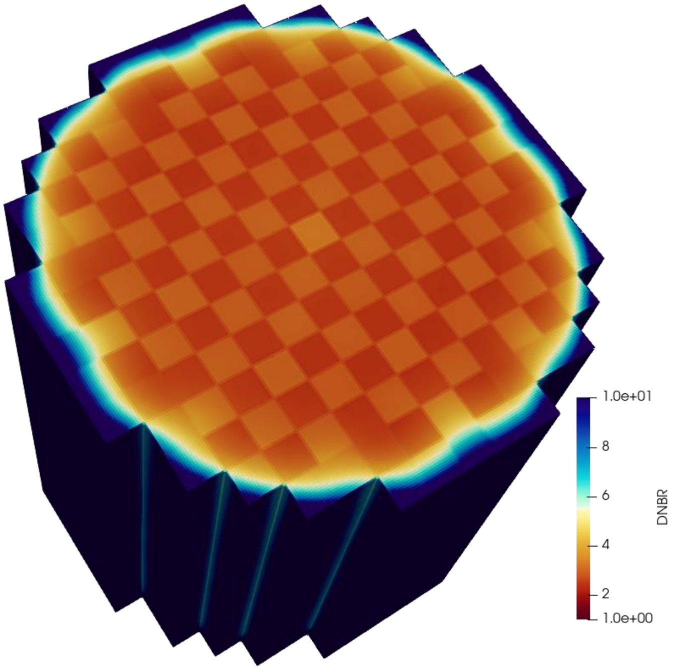

Fig. 4.33: pin-by-pin DNBR at t = 0*sec* for the axial level Z = 3.3*m*.

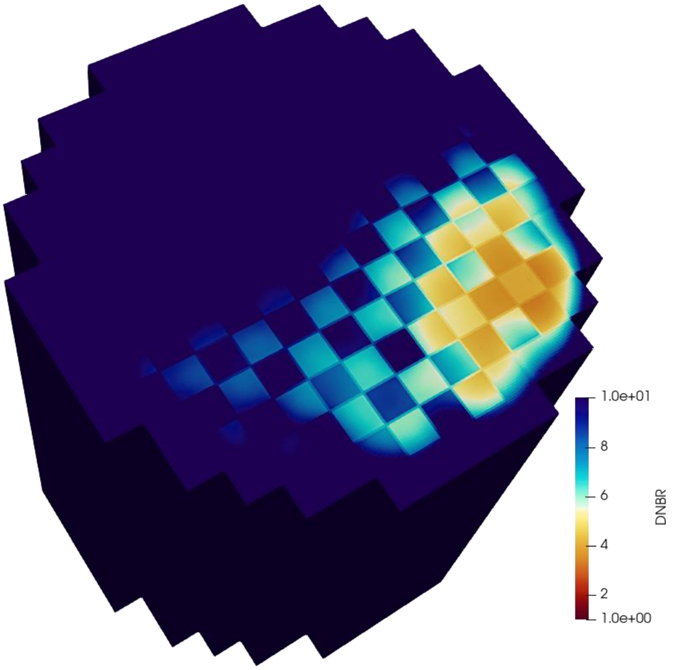

Fig. 4.34: pin-by-pin DNBR at t = 58*sec* for the axial level Z = 3.3*m*.

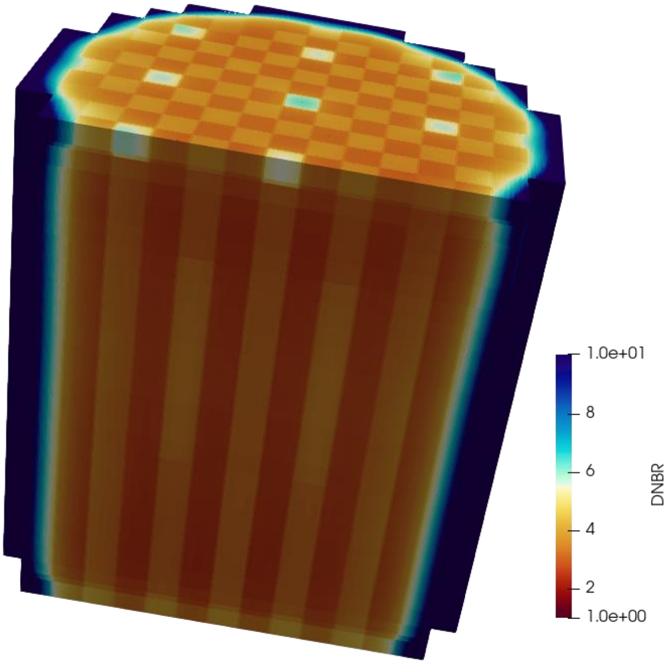

Fig. 4.35: pin-by-pin DNBR at $t = 0sec$ - cold side cross section.

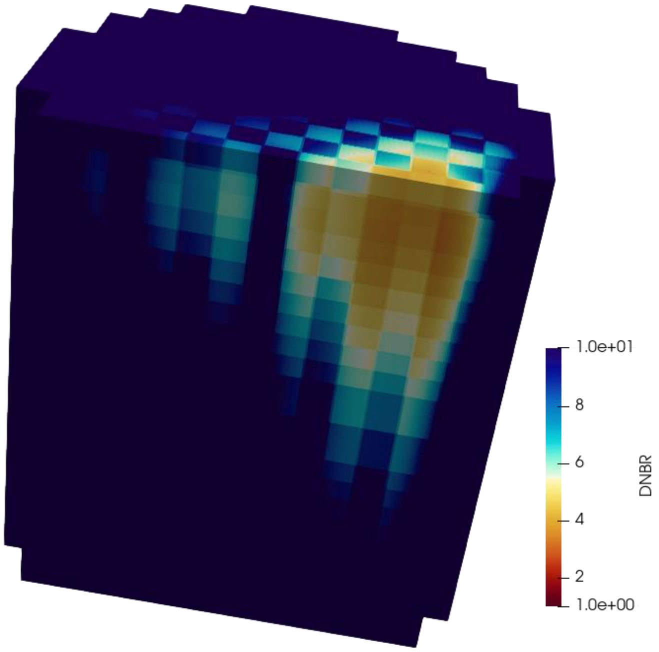

Fig. 4.36: the pin-by-pin DNBR at $t = 58sec$ - cold side cross section.

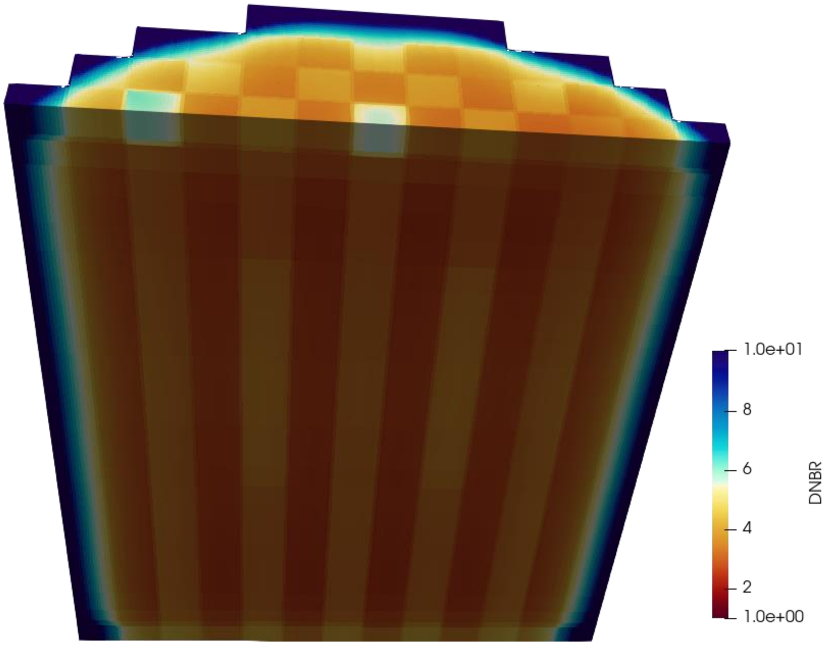

Fig. 4.37: pin-by-pin DNBR at $t = 0sec$ – hot/cold side cross section.

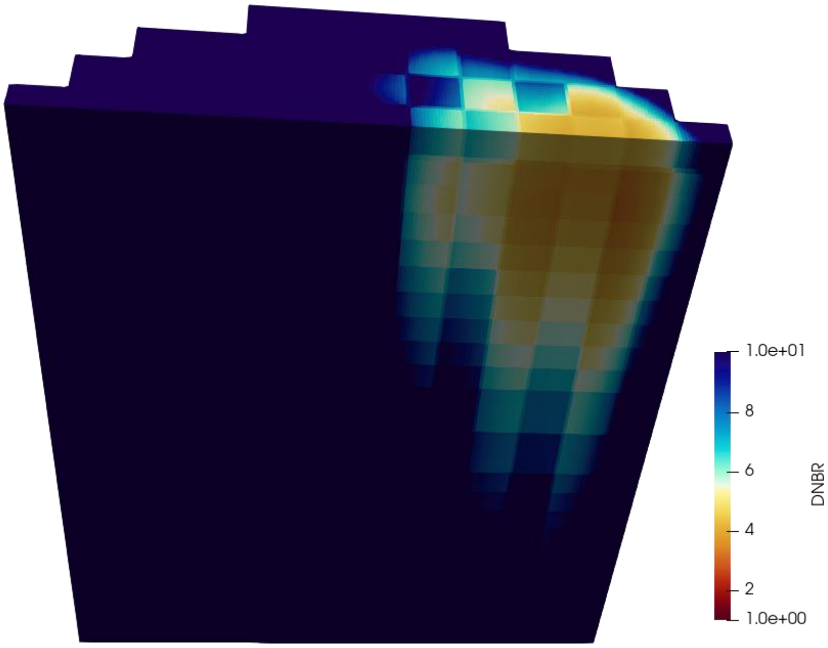

Fig. 4.38: pin-by-pin DNBR at $t = 58sec$ – hot/cold side cross section.

4.3.2.3 Performance analysis

These two calculations have been performed on the Soochiro4 cluster machine of the SNURPL which has the following characteristics:

- # of computing nodes: 9,
- CPU per node: 2 Intel Xeon E5-2630 v4 having 10 cores of 2.2 GHz each, and
- Interconnection: Mellanox Infiniband.

The total calculation time for the two analyses was 5*h* 53*min* 36*sec* for the NoRP case while for the RP was 6*h* 44*min* 2*sec*. Those two calculation times seem high but in terms of time per time-step is just 22*sec* and 25*sec*, respectively. In addition, this analysis is performed at pin level and the number of pins per plane is 54,225 in opposite to the assembly-wise solution where the number of nodes was just 241. Similar increased numbers are seen for the T/H solver, the number of subchannels in fact increased from 18 (or 241) up to 40,276.

Fig. 4.39 shows the number of neutronics and T/H iterations for NoRP (*top*) and RP (*bottom*). The solver shows the highest number of iterations during the SCRAM phase; this can be explained by the fact that in that instant the power drop is very high in a short time. ESCOT shows always one or two iterations more than the neutronics because of the initial fuel temperature prediction outside the neutronics loop and/or the coolant sweep after the fission source has converged in the time-step (see Fig. 4.1 *bottom*).

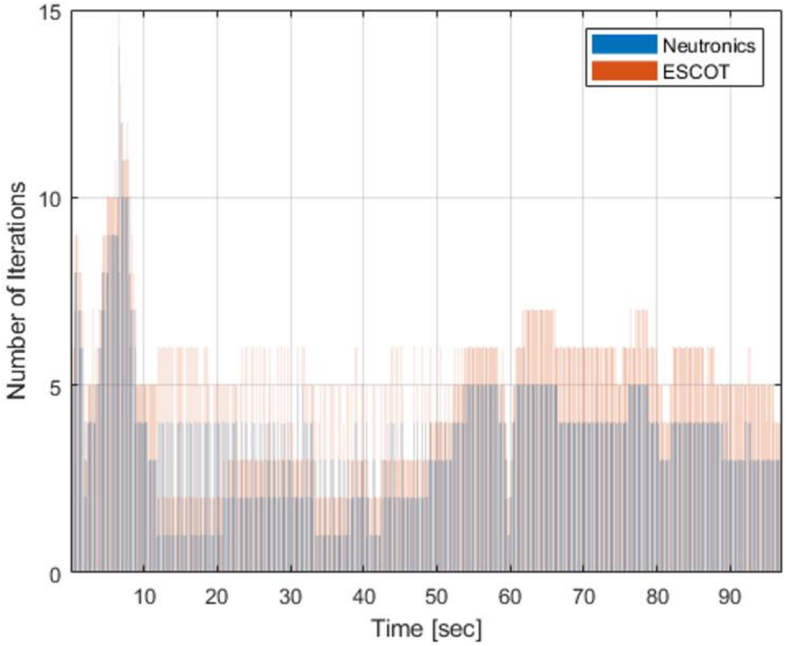

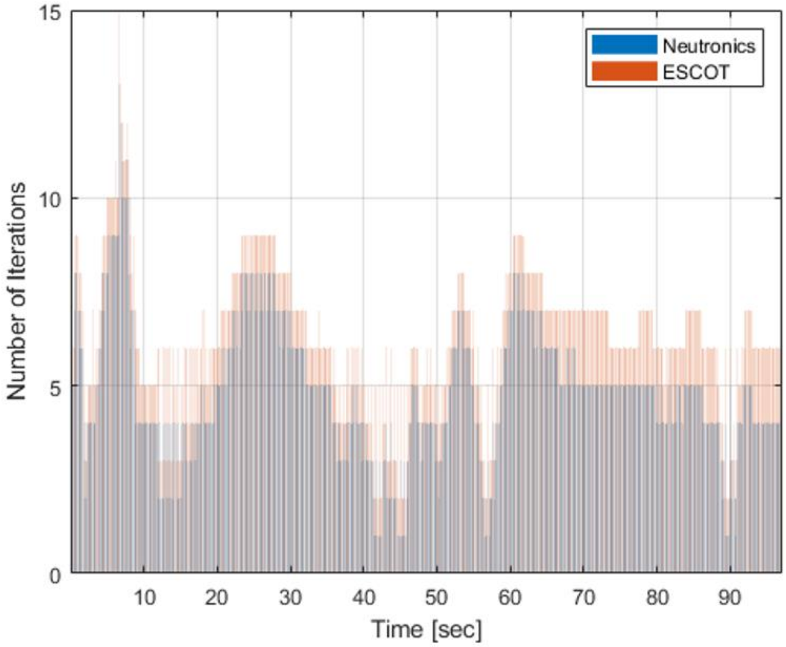

Fig. 4.39: total number of neutronics and T/H iterations for the NoRP (*top*) and RP (*bottom*).

ESCOT calculation burden was 36.5% and 35.3%, respectively. The time fractions of the entire T/H calculation time are displayed in Fig. 4.40 for the NoRP (*top*) and RP (*bottom*). Since most of the ESCOT calculation is performed using the fuel conduction solver, the highest fraction of calculation is taken by the *coupled operations* in which the T/H adjusts the common variables and passes them back to the neutronics solver. In general, this operation has a lower impact in steady-state transport calculations because the number of iterations is lower than 6 – 9 but in this case the number of ESCOT call was 4,927 and 6,039.

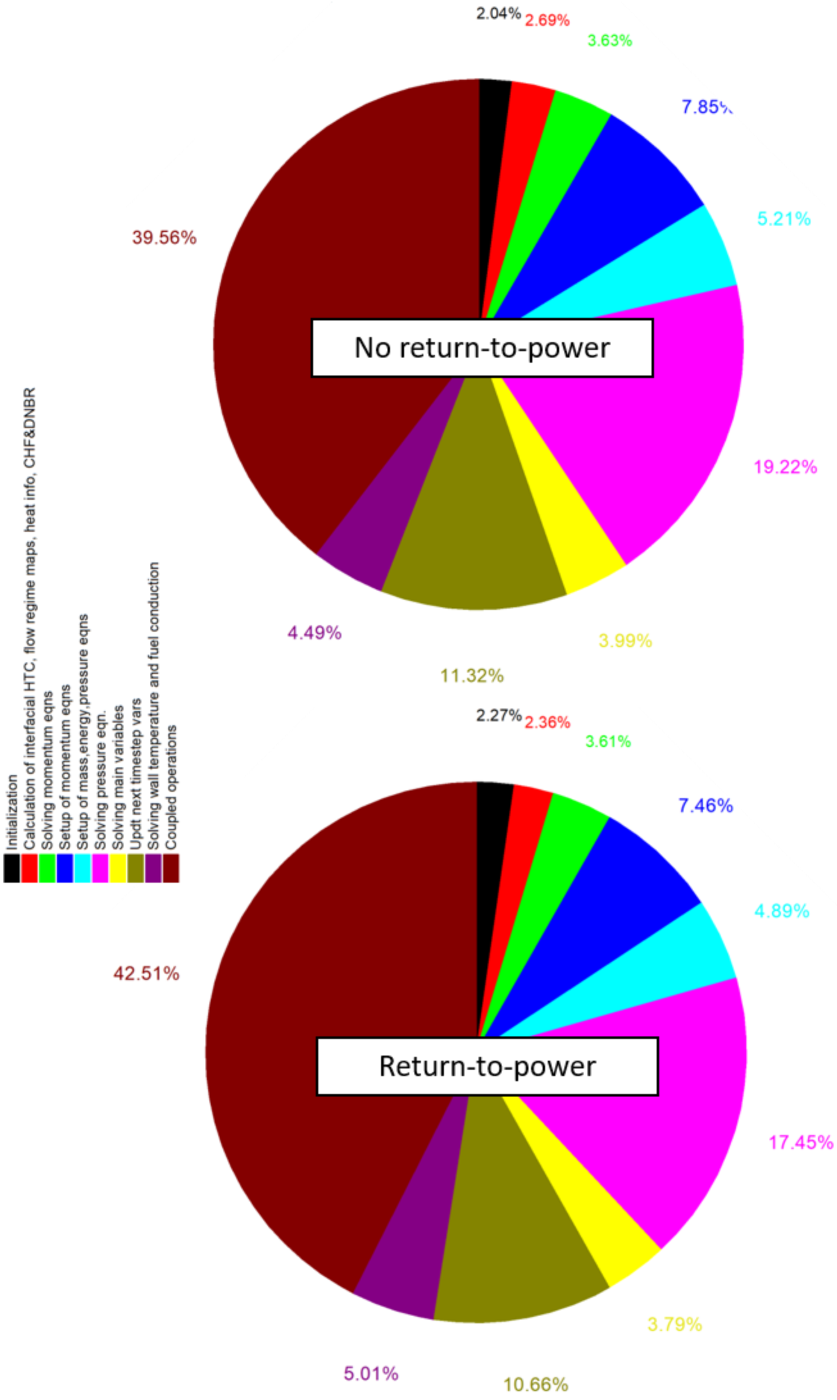

Fig. 4.40: fractions of calculation time for the ESCOT code.

Chapter 5. Summary and Conclusions

The pin level core T/H analysis code ESCOT was developed based on the 4-equation drift-flux model and the SIMPLEC numerical algorithm. Fundamental subchannel phenomena such as pressure drops, vapor generation, heat transfer at the liquid-vapor interface and turbulent mixing have been successfully implemented first, and validated after, through the use of experimental data and code-to-code comparison. In addition, a high fidelity solid conduction solver for steady-state and transient cases have been inserted in order to predict the fuel temperature profiles. The ESCOT code has been demonstrated to be a good compromise between solution accuracy and computational time compared to the standard two-fluid three-field codes for steady-state and mild transient analyses. The code showed its capability to correctly represent key phenomena of single and two phase flow at a whole core subchannel level for the pre-CHF flow regimes.

The ESCOT code has been subsequently coupled with the DWCC code nTRACER using a wrapping system in order to perform steady-state coupled neutronics-T/H core analyses. The replacement of the internal 1D simplified T/H with a subchannel code allowed to simulate the core T/H more realistically, properly predicting important pin level phenomena such as pressure drops, mixing, cross-flow and spacer grids effects. In general, coupled calculations based on Picard FPI scheme have a low robustness, thus smoothening techniques are generally employed to improve the stability but they are user and problem dependent. The Anderson Acceleration scheme has been implemented in nTRACER and nTRACER/ESCOT to stabilize the intermediate solutions obtained after each FPI in a neutronics-T/H coupled calculation and to remove the problem and user dependency of the standard application of relaxation factors. In AA, the solution at the $(k + 1)^{th}$ FPI is expressed as a linear combination of a certain number m of solutions whose coefficients are determined by minimizing the square norm of the linearly combined residual vectors. The effectiveness of AA-m was examined for several reduced problems using nTRACER standalone and then using nTRACER/ESCOT for actual core problems both for simple feedback and depletion analyses.

It turned out that the number of FPIs can be reduced by about 25% with the AA scheme. The standard convergence check based on fission source pseudo errors cannot properly catch the convergence status of fission source as the difference between two successive iterations can be large if there are oscillations from iteration to iteration around the converged solution, despite approaching it monotonously.

The GS-based scheme may run into an overshooting of the iterative solution around the reference. The removal of the oscillatory behavior which is possible with AA-m turned out to be the fundamental driving factor to show the effectiveness of AA. Namely, the oscillation of the intermediate around the true solution can be effectively removed by smoothening the solution between successive iterations.

Since the computing time is proportional to the number of FPIs, the calculation time of the nTRACER coupled neutronics-T/H simulations could be reduced by about 20 – 30% demonstrating the effectiveness of Anderson Acceleration.

It was also noted that increasing the storage depth of the Anderson Acceleration scheme does not always ensure faster convergence; as a matter of fact, AA-2 required slightly more iterations in some cases. This might be due to the limitation of determining the linear combination coefficients based only on the norm of the linearly combined residual vectors. In complex nonlinear problems such as coupled neutronics-T/H calculations, odd convergence behavior might occur due to this limitation. Nonetheless, it is recommended to use AA-2 as the default because it allows better convergence in most of the cases.

Finally, a time-dependent coupled analysis has been performed. Transient coupled analyses usually deal with RIA. In general, reactivity transients can be categorized in two types: fast (or prompt) and slow (or slow). In control rod ejection-like scenarios (fast transient), the coolant status is generally less important than the fuel temperature one. In fact, in this type of events the most important T/H phenomena occur inside the fuel pellet and a refined solver for the moderator would only increase the calculation time without providing additional important information. More benefits in using ESCOT rise if simulating slow scenarios, such as loss of power, turbine trip or MSLB, because of the large presence of asymmetry, high mixing phenomena or T/H boundary condition variation in rapid/slow times. Therefore, the transient coupling of the ESCOT code has been performed with a pin-by-pin FDM SP_3 based code with the final objective of simulating the MSLB scenario. The MSLB accident postulated in PWR safety analyses involves a considerable reduction of the inlet coolant temperature of one side of the reactor core which causes a considerable asymmetry in the radial flow conditions. The positive reactivity feedback effect introduced by the decrease of the coolant temperature appears non-uniform, because of this asymmetry. For conservatism, a stuck rod on the cold side is considered during the reactor SCRAM in the analysis. This manuscript analyzed the Exercise II of the NEA/OECD MSLB benchmark which deals only with the core level phenomena and does not require system modeling since two sets of time dependent boundary conditions and cross section libraries is provided by the benchmark administrators. It turned out that the maximum return-to-power calculated with pin level solvers was 2% lower than the one calculated with assembly-wise solvers. The main reasons were found into a higher SCRAM worth, a higher coolant temperature and a better nodalization of neutronics and T/H. In addition, the mixing region between the two sides of the core is actually limited to the central assembly row and the size of it increases with the axial level because of a CB-like power distribution in the three central assembly lines around the separation between hot and cold side. Around the stuck rod, the mixing capabilities of ESCOT were also crucial to better predict the coolant temperature distribution. The use of pin-by-pin solvers allowed also to picture the high difference (~127%) in power estimation at the instant of maximum return-to-power with the conventional assembly-wise solvers which cannot catch high gradient present in assemblies close to the stuck rod. This study demonstrates the importance of moving to pin-wise coupled transient analyses to fully understand the behavior when calculating asymmetrical time-dependent scenarios. Moreover, this system performed the calculation with an average time of 25*sec* per simulated time-step.

Some following tasks are here suggested. ESCOT development should be still constrained to coupled analyses and the extension to post-CHF, even if necessary, would not increase ESCOT usefulness. In fact, in coupled PWR analyses the 3D DFM provides good prediction of the marginal void fraction which can occur during steady-state or mild transient cases.

Three more separate works would value the ESCOT code more. One could be the extension of ESCOT to VVER analysis. This new code could be then coupled with nTRACER to have an additional DWCC tool for simulating hexagonal-based cores. Another important extension could be the triple coupling nTRACER/ESCOT/FRAPCON (or BISON) for high-fidelity PWR steady-state analyses in which the analyses is extended also to fuel performance. Finally, the extension of ESCOT from steady-state to transient analyses performed in this manuscript opened the door to a possible triple coupling system between a pin-by-pin SP_3 code, ESCOT and a system code to have a primary loop solver for PWR plants.

In parallel, the GPU conversion of the ESCOT code must continue in order to provide incredibly fast coupled solvers for steady-state and transient DWCC.

Acknowledgements

First of all, I would like to pay my biggest gratitude to Professor Joo Han Gyu for having accepted me as a graduate student at the SNU Reactor Physics Laboratory, having tutored and guided me through this long and intense four years. I will be forever grateful.

After that, I want to thank the committee Professor Cho Hyoung Kyu, Professor Kim Eung Soo, Doctor Cho Jinyoung and Doctor Lee Eun Ki for having put interest in my research and for having provided valuable advices and recommendations during the evaluation process.

Another important *thank you* goes to my dear friend and former colleague Doctor Lee Jaejin, we have worked side-by-side for two years and without his help this work would not have been possible. I want to express the same gratitude to *Doctor to be* at the writing moment and Doctor at reading moment, Choi Namjae for having helped when necessary and for having been always keen to discuss research topics and sharing ideas. Our chats have inspired me and have given me different perspectives. A big thanks goes also to the current and former members of the SNURPL Han Gyu, Seungug, Seongchan, Junsu, Seung Yop, Seo Yoon, Hyun Ho, Hyunsik, Kyung Min, Jaeuk, Yeong Suk, Jun Teak, Alex and Jorge. It has been an honor to share this experience with you all. Together with the lab members, a special thanks goes also to the other international students of the Department of Nuclear Engineering, Erol and Ali, class and coffee buddies for this period.

The first thank you not directed to the working environment goes to Chloé, thank you for your support, for your love and time you have given to me. You are the best!

To my family, my parents, my grand-parents, my brother, my cousins, my aunts and my uncles, thank you for having supported me from far away through this long path.

To the Seoul gang a huge thank you! Jorge, Adam, Vincent, Gabe, Jake, Roberto, Denis, Lucia, Lorenza, Silvia, Rahel, Charlie, you guys have filled this Korean time and you have become true friends of mine. I will always remember you.

To my friends in Italy and spread somewhere in Europe, thanks for always having been there for me when needed and when not.

And finally, thanks to everyone that in a way or another has led me to achieve this finishing line.

Onto the next one!

Alberto

Appendix 1. Derivation of the Pressure Correction Equation

In order to derive the pressure correction, it is necessary to discretize the two mass balances and the energy balance and linearize the secondary variables in order to show their dependence only on the primary ones. The scalar variables are linearized as:

$$\phi(t+\Delta t)=\phi(t)+\frac{\partial \phi(t)}{\partial t}\Delta t+\cdots, \tag{A.1}$$

thus, the mixture density can be linearized as follows:

$$\begin{aligned}
\frac{\partial \rho_m(\alpha,\rho_v,\rho_l)}{\partial t} &= \frac{\partial \alpha}{\partial t}\left(\frac{\partial \rho_m}{\partial \alpha}\right)^n+\frac{\partial \rho_v}{\partial t}\left(\frac{\partial \rho_m}{\partial \rho_v}\right)^n+\frac{\partial \rho_l}{\partial t}\left(\frac{\partial \rho_m}{\partial \rho_l}\right)^n= \\
&= \frac{\partial \alpha}{\partial t}\left(\rho_v^n-\rho_l^n\right)+\frac{\partial \rho_{v,sat}(P)}{\partial t}\alpha^n+\frac{\partial \rho_l(P,h_l)}{\partial t}\left(1-\alpha^n\right)= \\
&= \frac{\partial \alpha}{\partial t}\left(\rho_v^n-\rho_l^n\right)+\frac{\partial P}{\partial t}\left(\frac{\partial \rho_v}{\partial P}\right)^n\alpha^n+\left[\frac{\partial P}{\partial t}\left(\frac{\partial \rho_l}{\partial P}\right)^n+\frac{\partial h_l}{\partial t}\left(\frac{\partial \rho_l}{\partial h_l}\right)^n\right]\left(1-\alpha^n\right)
\end{aligned} \quad . \tag{A.2}$$

If the first order approximation is taken for temporal derivative, then the mixture density at the new time-step can be approximated as follows:

$$\begin{aligned}
\rho_m^{n+1} &= \rho_m^n+\left(\alpha^{n+1}-\alpha^n\right)\left(\rho_v^n-\rho_l^n\right)+\left(P^{n+1}-P^n\right)\left(\frac{\partial \rho_v}{\partial P}\right)^n\alpha^n+ \\
&+\left[\left(P^{n+1}-P^n\right)\left(\frac{\partial \rho_l}{\partial P}\right)^n+\left(h_l^{n+1}-h_l^n\right)\left(\frac{\partial \rho_l}{\partial h_l}\right)^n\right]\left(1-\alpha^n\right)
\end{aligned} \quad . \tag{A.3}$$

After having discretized Eq. (2.18), Eq. (A.3) is plugged in. Then, the scalar primary variables are moved to the LHS while the velocity terms are moved on the

RHS; the discretized mixture balance equation can be finally expressed as:

$$\begin{gathered} a_{11}h_{l,I,J}^{n+1} + a_{12}\alpha_{I,J}^{n+1} + a_{13}P_{I,J}^{n+1} = \\ = -\left[\sum_{ic=1}^{nb} \left[\rho_m^{\bar{n}} \left(\vec{u}_m^{n+1} \cdot \vec{s} \right)_{ic} \Delta z_J \right]_{ic,J} + \left[\rho_m^{\bar{n}} w_m^{n+1} A_c \right]_{I,j} - \left[\rho_m^{\bar{n}} w_m^{n+1} A_c \right]_{I,j-1} \right] + s_1 \end{gathered}, \quad \text{(A.4)}$$

where:

$$a_{11} = \left(\frac{\partial \rho_l}{\partial h_l} \right)_{I,J}^{n} \left(1 - \alpha_{I,J}^{n} \right) \left(\frac{A_{c,I,J} \Delta z_J}{\Delta t} \right), \quad \text{(A.5)}$$

$$a_{12} = \left(\rho_{v,I,J}^{n} - \rho_{l,I,J}^{n} \right) \left(\frac{A_{c,I,J} \Delta z_K}{\Delta t} \right), \quad \text{(A.6)}$$

$$a_{13} = \left(\left(\frac{\partial \rho_v}{\partial P} \right)_{I,J}^{n} \alpha_{I,J}^{n} + \left(\frac{\partial \rho_l}{\partial P} \right)_{I,J}^{n} \left(1 - \alpha_{I,J}^{n} \right) \right) \left(\frac{A_{c,I,J} \Delta z_J}{\Delta t} \right) \text{ and} \quad \text{(A.7)}$$

$$s_1 = a_{11} h_{l,I,J}^{n} + a_{12} \alpha_{I,J}^{n} + a_{13} P_{I,J}^{n} + \sum_{nnb} \left[TM_m \right]_{nnb}^{n} . \quad \text{(A.8)}$$

For the vapor mass balance, it is necessary to add the linearization of vapor density, liquid temperature and vapor temperature:

$$\rho_v^{n+1} = \rho_v^{n} + \left(P^{n+1} - P^{n} \right) \left(\frac{\partial \rho_v}{\partial P} \right)^{n}, \quad \text{(A.9)}$$

$$T_l^{n+1} = T_l^{n} + \left(P^{n+1} - P^{n} \right) \left(\frac{\partial T_l}{\partial P} \right)^{n} + \left(h_l^{n+1} - h_l^{n} \right) \left(\frac{\partial T_l}{\partial h_l} \right)^{n} \text{ and} \quad \text{(A.10)}$$

$$T_{v,sat}^{n+1} = T_{v,sat}^{n} + \left(P^{n+1} - P^{n} \right) \left(\frac{\partial T_{v,sat}}{\partial P} \right)^{n} . \quad \text{(A.11)}$$

The discretized vapor balance equation is then expressed as:

$$\begin{gathered} a_{21}h_{I,J}^{n+1} + a_{22}\alpha_{I,J}^{n+1} + a_{23}P_{I,J}^{n+1} = \\ = -\sum_{ic=1}^{nb} \left[\left(\alpha \rho_v \right)^{\bar{n}} \left(\vec{u}_m^{n+1} \cdot \vec{s} \right) \Delta z_J \right]_{ic,J} + \left[\left(\alpha \rho_v \right)^{\bar{n}} w_m^{n+1} A_c \right]_{I,j} - , \\ - \left[\left(\alpha \rho_v \right)^{\bar{n}} w_m^{n+1} A_c \right]_{I,j-1} + s_2 \end{gathered} \quad \text{(A.12)}$$

where:

$$a_{21} = -\frac{H_{il}^{n}}{h_{v,sat}^{n} - h_{il}^{n}} \left(\frac{\partial T_l}{\partial h_l} \right)_{I,J}^{n} A_{c,I,J} \Delta z_J \,, \tag{A.13}$$

$$a_{22} = \rho_{v,I,J}^{n} \left(\frac{A_{c,I,J} \Delta z_J}{\Delta t} \right), \tag{A.14}$$

$$\begin{gathered} a_{23} = \alpha_{I,J}^{n} \left(\frac{\partial \rho_v}{\partial P} \right)_{I,J}^{n} \left(\frac{A_{c,I,J} \Delta z_J}{\Delta t} \right) + \\ + \frac{H_{il}^{n}}{h_{v,sat}^{n} - h_{il}^{n}} \left[\left(\frac{\partial T_{v,sat}}{\partial P} \right)_{I,J}^{n} - \left(\frac{\partial T_l}{\partial P} \right)_{I,J}^{n} \right] A_{c,I,J} \Delta z_J \end{gathered} \quad \text{and} \tag{A.15}$$

$$\begin{gathered} s_2 = \left(\frac{H_{il}^{n} (T_l^{n} - T_{v,sat}^{n})}{h_{v,sat}^{n} - h_{li}^{n}} + \Gamma_w \right)_{I,J} A_{c,I,J} \Delta z_J - \sum_{nnb} \left[CV \right]_{nnb}^{n} + \\ + a_{21} h_{l,I,J}^{n} + a_{22} \alpha_{I,J}^{n} + a_{23} P_{I,J}^{n} + \sum_{nnb} \left[TM_v \right]_{nnb}^{n} \end{gathered} \,. \tag{A.16}$$

For the mixture energy balance, an additional linearization parameter is the energy density and it is formulated as:

$$\begin{gathered} \left(\rho_m h_m \right)^{n+1} = \left(\rho_m h_m \right)^{n} + \left(\alpha^{n+1} - \alpha^{n} \right) \left(\left(\rho_v h_v \right)^{n} - \left(\rho_l h_l \right)^{n} \right) + \\ + \left(\left(P^{n+1} - P^{n} \right) \left(\frac{\partial \rho_l}{\partial P} \right)^{n} + \left(h_l^{n+1} - h_l^{n} \right) \left(\frac{\partial \rho_l}{\partial h_l} \right)^{n} \right) \left(1 - \alpha^{n} \right) h_l^{n} + \\ + \left(P^{n+1} - P^{n} \right) \left(\frac{\partial \rho_v}{\partial P} \right)^{n} \left(\alpha h_v \right)^{n} + \\ + \left(h_l^{n+1} - h_l^{n} \right) \left(1 - \alpha^{n} \right) \rho_l^{n} + \left(P^{n+1} - P^{n} \right) \left(\frac{\partial h_v}{\partial P} \right)^{n} \left(\alpha \rho_v \right)^{n} \end{gathered} \,. \tag{A.17}$$

This last parameter allows to write:

$$\begin{gathered} a_{31} h_{l,I,J}^{n+1} + a_{32} \alpha_{I,J}^{n+1} + a_{33} P_{I,J}^{n+1} = \\ = - \sum_{ic=1}^{nb} \left[\left(\rho_m h_m \right)^{\bar{n}} \left(\vec{u}_m^{\,n+1} \cdot \vec{s} \right) \Delta z_J \right]_{ic,J} + \\ + \left[\left(\rho_m h_m \right)^{\bar{n}} \left(w_m \right)^{n+1} A_c \right]_{I,j} - \left[\left(\rho_m h_m \right)^{\bar{n}} \left(w_m \right)^{n+1} A_c \right]_{I,j-1} + s_3 \end{gathered} \,, \tag{A.18}$$

where:

$$a_{31} = \left(1-\alpha_{I,J}^{n}\right)\left(\left(\frac{\partial\rho_l}{\partial h_l}\right)_{I,J}^{n} h_{l,I,J}^{n} + \rho_{l,I,J}^{n}\right)\frac{A_{c,I,J}\Delta z_J}{\Delta t}, \qquad \text{(A.19)}$$

$$a_{32} = \left(\left(\rho_v h_v\right)_{I,J}^{n} - \left(\rho_l h_l\right)_{I,J}^{n}\right)\frac{A_{c,I,J}\Delta z_J}{\Delta t}, \qquad \text{(A.20)}$$

$$\begin{aligned} a_{33} = {} & \left(h_{l,I,J}^{n}\left(1-\alpha_{I,J}^{n}\right)\left(\frac{\partial\rho_l}{\partial P}\right)_{I,J}^{n} + \left(\frac{\partial\rho_v}{\partial P}\right)_{I,J}^{n}\left(\alpha h_v\right)_{I,J}^{n}\right)\left(\frac{A_{c,I,J}\Delta z_J}{\Delta t}\right) + \\ & + \left(\left(\frac{\partial h_v}{\partial P}\right)_{I,J}^{n}\left(\alpha\rho_v\right)_{I,J}^{n} - 1\right)\left(\frac{A_{c,I,J}\Delta z_J}{\Delta t}\right) \end{aligned} \quad \text{and} \quad \text{(A.21)}$$

$$\begin{aligned} s_3 = {} & \sum_{hnb}\left[TM_{en}\right]_{hnb}^{n} + q_w''\xi_c\Delta z_J + q_v'''A_{c,I,J}\Delta z_J - \\ & -\sum_{nnb}\left[CE\right]_{nnb}^{n} + a_{31}h_{l,I,J}^{n} + a_{32}\alpha_{I,J}^{n} + a_{33}P_{I,J}^{n} \end{aligned}. \qquad \text{(A.22)}$$

Finally, for a specific cell (*I*,*J*), the following system can be written as:

$$\begin{bmatrix} a_{11} & a_{12} & a_{13} \\ a_{21} & a_{22} & a_{23} \\ a_{31} & a_{32} & a_{33} \end{bmatrix}\begin{bmatrix} h_{l,I,J}^{n+1} \\ \alpha_{I,J}^{n+1} \\ P_{I,J}^{n+1} \end{bmatrix} = \begin{bmatrix} s_1 \\ s_2 \\ s_3 \end{bmatrix} - \begin{bmatrix} b_{11} & b_{12} & b_{13} & b_{14} & b_{15} & b_{16} \\ b_{21} & b_{22} & b_{23} & b_{24} & b_{25} & b_{26} \\ b_{31} & b_{32} & b_{33} & b_{23} & b_{35} & b_{36} \end{bmatrix}\begin{bmatrix} u_{ie,J}^{n+1} \\ -u_{iw,J}^{n+1} \\ v_{is,J}^{n+1} \\ -v_{in,J}^{n+1} \\ w_{I,j}^{n+1} \\ -w_{I,j-1}^{n+1} \end{bmatrix}, \text{(A.23)}$$

by inverting the 3*x*3 matrix and replacing the velocity terms with the SIMPLE-like definitions [32], the following system can be written:

$$\begin{bmatrix} h_{l,I,J}^{n+1} \\ \alpha_{I,J}^{n+1} \\ P_{I,J}^{n+1} \end{bmatrix} = \begin{bmatrix} s_1' \\ s_2' \\ s_3' \end{bmatrix} - \begin{bmatrix} b_{11}' & b_{12}' & b_{13}' & b_{14}' & b_{15}' & b_{16}' \\ b_{21}' & b_{22}' & b_{23}' & b_{24}' & b_{25}' & b_{26}' \\ b_{31}' & b_{32}' & b_{33}' & b_{23}' & b_{35}' & b_{36}' \end{bmatrix}\begin{bmatrix} d_{ie,J}\left[P_{I,J}^{n+1} - P_{IE,J}^{n+1}\right] \\ -d_{iw,J}\left[P_{I,J}^{n+1} - P_{IW,J}^{n+1}\right] \\ d_{is,J}\left[P_{I,J}^{n+1} - P_{IS,J}^{n+1}\right] \\ -d_{in,J}\left[P_{I,J}^{n+1} - P_{IN,J}^{n+1}\right] \\ d_{I,j}\left[P_{I,J}^{n+1} - P_{I,J+1}^{n+1}\right] \\ -d_{I,j-1}\left[P_{I,J}^{n+1} - P_{I,J-1}^{n+1}\right] \end{bmatrix}. \qquad \text{(A.24)}$$

The pressure correction equation is represented by the 3rd row of the previous system:

$$\begin{gathered}-b'_{36}P^{n+1}_{I,J-1}-b'_{34}P^{n+1}_{IN,J}-b'_{32}P^{n+1}_{IW,J}+\left[1+\sum_{nb}b'_{nb}\right]P^{n+1}_{I,J}- \\ -b'_{31}P^{n+1}_{IE,J}-b'_{33}P^{n+1}_{IS,J}-b'_{35}P^{n+1}_{I,J+1}=s'_3\end{gathered}. \tag{A.25}$$

Appendix 2. Single phase validation

The ESCOT code has been validated using three single phase experiments, two unheated and one heated:

- CNEN 4*x*4 [92],
- WH 14*x*14 [93], and
- PNNL 2*x*6 [94].

The first experiment was performed in Italy and it has been used to validate mixing capability of codes aiming at simulating bundle geometries. The test section has a square geometry with 16 (4*x*4) rods (see Fig. A.1). The total height is 1.4*m* and a spacer grid is located in the middle of the test facility (0.7*m*). The experiment was performed with the 5 different inlet velocity conditions: 0.64, 1.32, 2.61, 3.83, and 5.18*m/s*, at atmospheric outer pressure and without any heat source. The outlet velocity in each subchannel was measured in the experiment. The ESCOT calculated outlet velocities have been compared with the experimental data and with the results produced with different codes. The effect of the turbulent mixing model is clear when comparing the results depicted in Fig. A.2 and Fig. A.3. The corner cells which have high-resistance due to small hydraulic diameters lose their momentum more than other cells. The flow, instead, goes towards the center cells that have the lower resistance. In reality, this effect can be mitigated by the turbulent mixing mechanism. If the turbulent mixing model is disabled in the code, the lost momentum at the corner cells cannot be compensated, so the velocities at the corner are underestimated. On the other hand, the velocities in the center cells are slightly overestimated. The same tendency can be observed in the results of CUPID. By adopting the turbulent mixing model, both codes start to capture the real phenomenon. The activation of this model has reduced the maximum error between the code and the measured data at the corner from 18.5% to 2.8%. In addition, it can be noticed by Tab. A.1 that the prediction of the three codes agree. In conclusion, the turbulent mixing model in ESCOT is correctly representing the subchannel phenomenon of turbulent mixing.

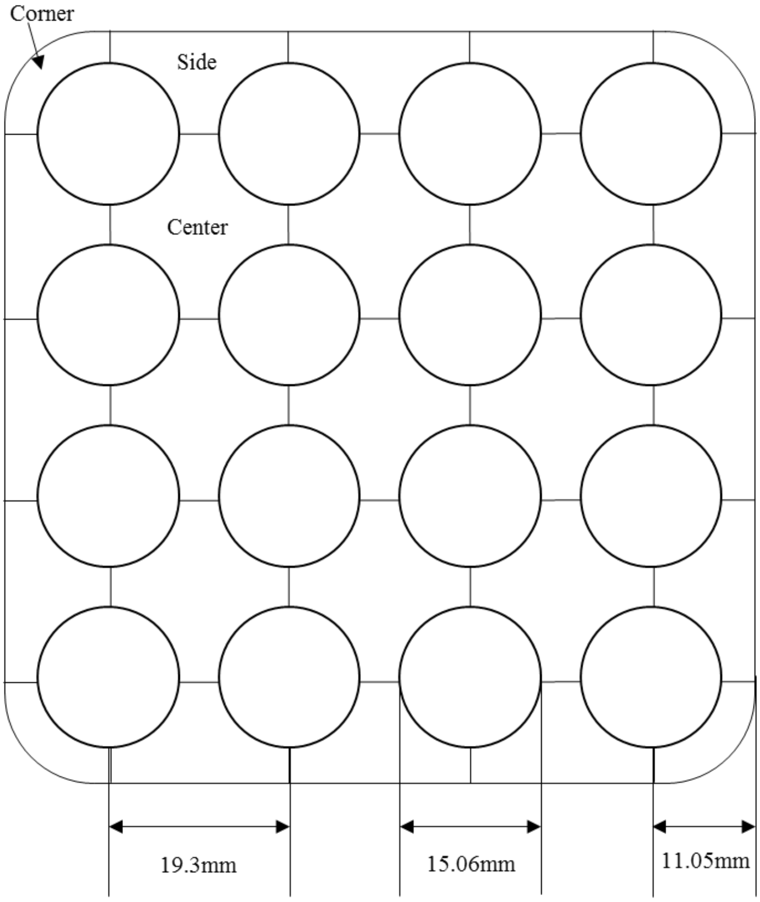

Fig. A.1: cross section of the test facility of CNEN 4*x*4.

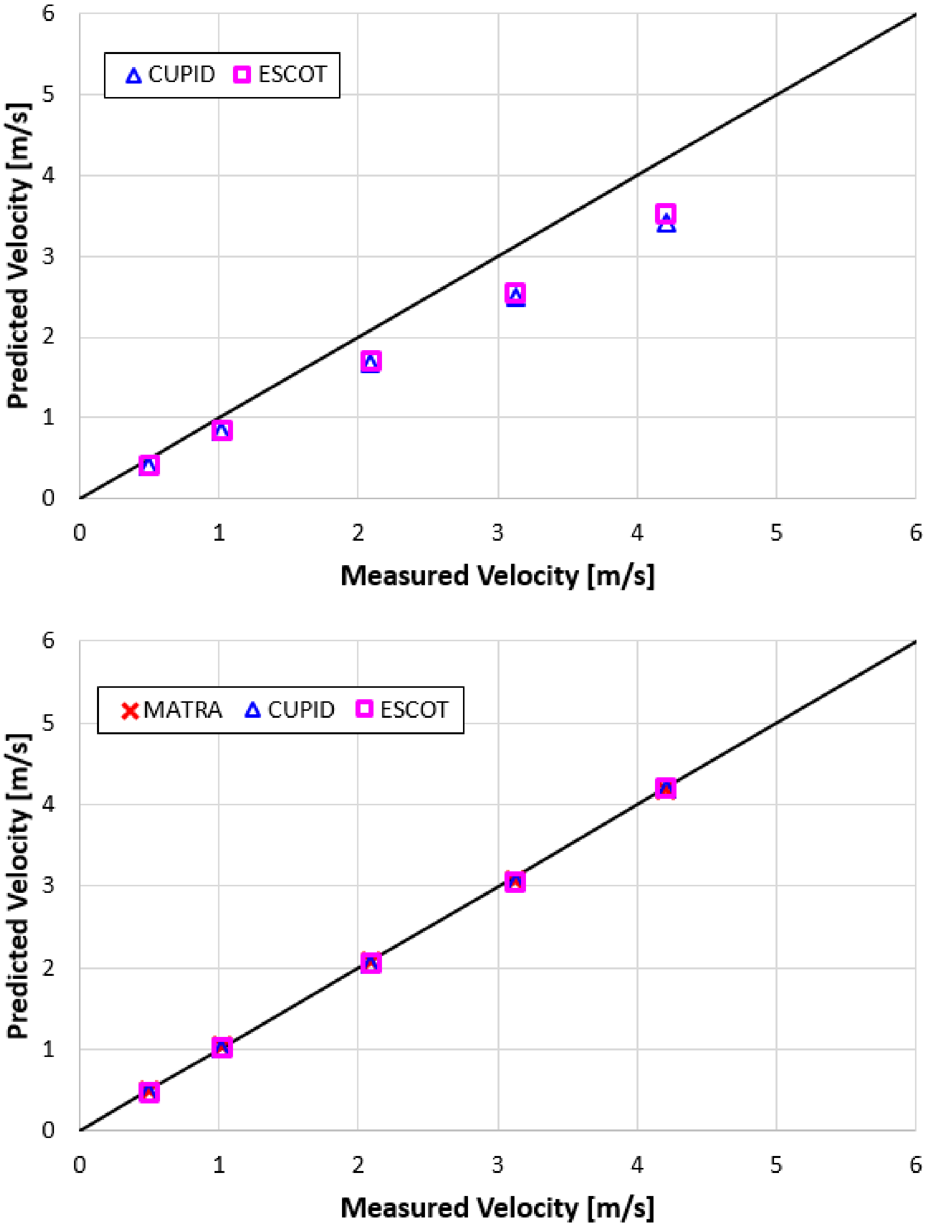

Fig. A.2: corner outlet velocities for the five analyzed cases without (top) and with (bottom) turbulent mixing model activated.

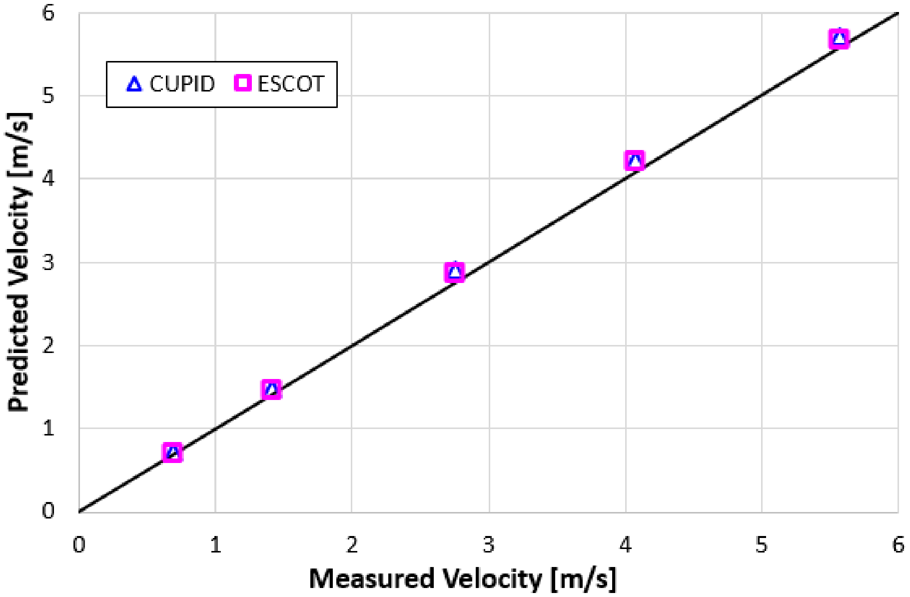

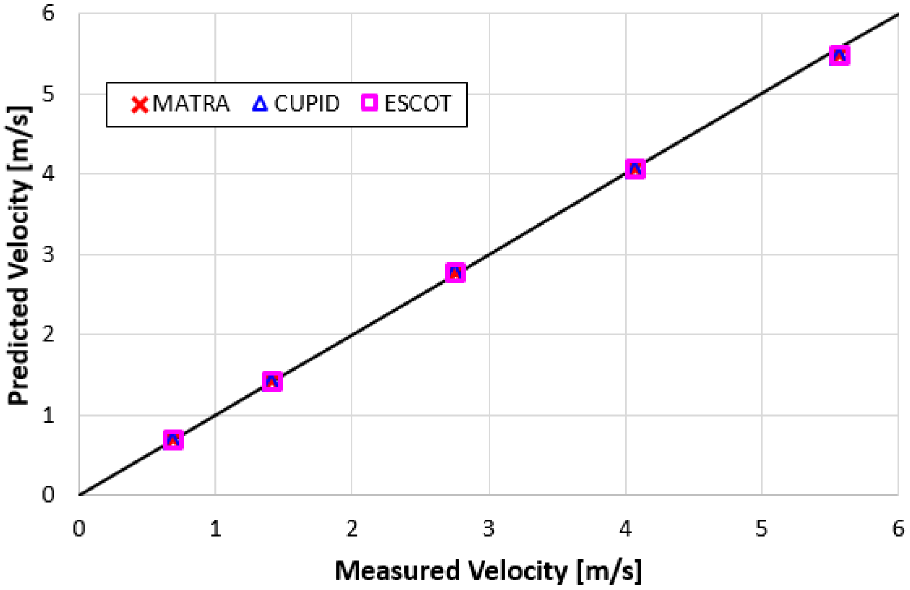

Fig. A.3: center outlet velocities for the five analyzed cases without (top) and with (bottom) turbulent mixing model activated.

Tab. A.1: error towards the experimental data of the calculated velocities of CNEN 4*x*4.

		w/o turb. mixing		**w/ turb. mixing**		
		ESCOT	**CUPID**	**ESCOT**	**CUPID**	**MATRA**
Corner	MAX [%]	18.7	20.4	3.2	3.0	2.2
	RMS [%]	17.5	19.3	1.9	1.9	1.2
Center	MAX [%]	4.7	5.5	1.7	1.6	1.6
	RMS [%]	3.9	4.7	0.9	0.9	0.9

The WH 14*x*14 experiment concerned a facility constituted by two assemblies as Fig. A.4 shows.

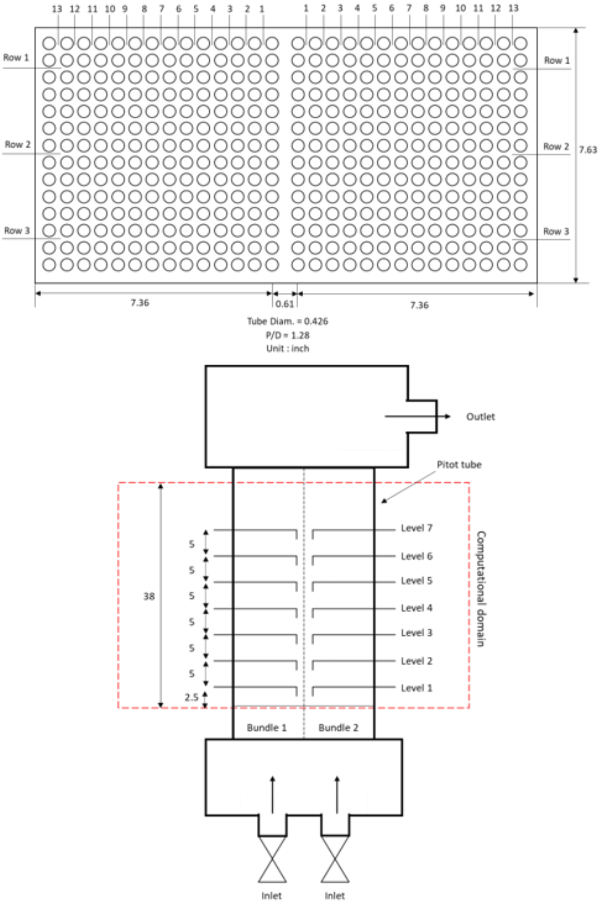

Fig. A.4: scheme of the WH 14*x*14 test facility.

Thanks to this test, the capabilities of predicting flow redistribution and reverse flow in bundles have been validated. Two main tests were carried out, the partial and full blockage. For the first one, the SNURPL had the experimental data while for the second one only a code-to-code is shown. In the case of partial blockage, the axial velocity trend is shown in Fig. A.5. The comparison towards experimental data are instead shown in Fig. A.6 and Fig. A.7 for each side averaged mass flow and for the row axial velocity at different measured levels. A complete summary of the partial blockage test is shown inside Tab. A.2.

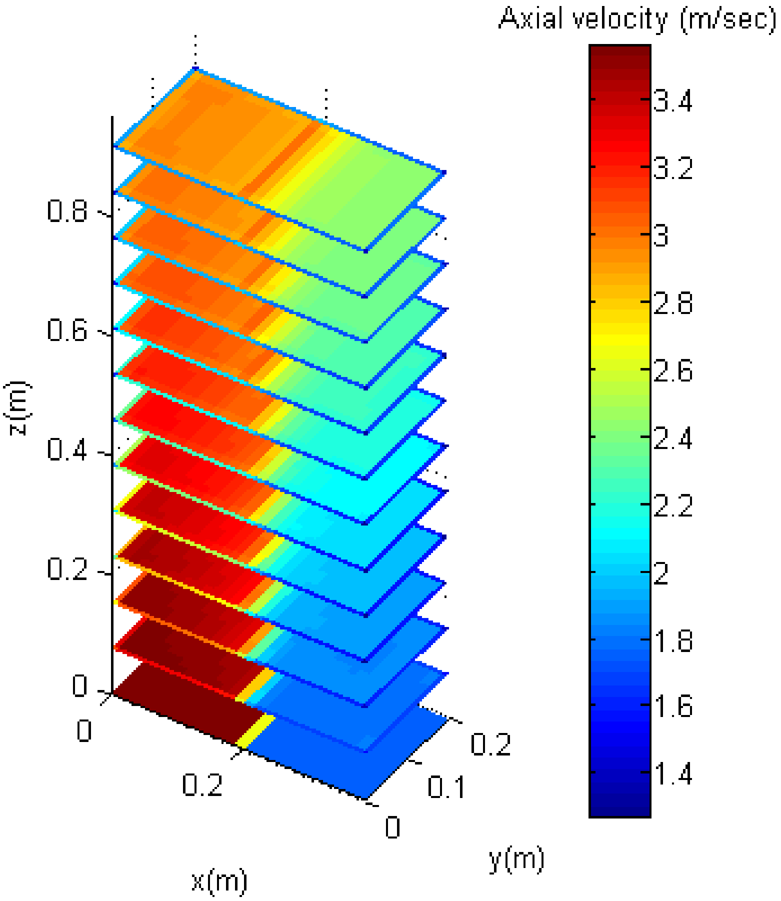

Fig. A.5: axial velocity contour map of WH 14*x*14 for the partial blockage case.

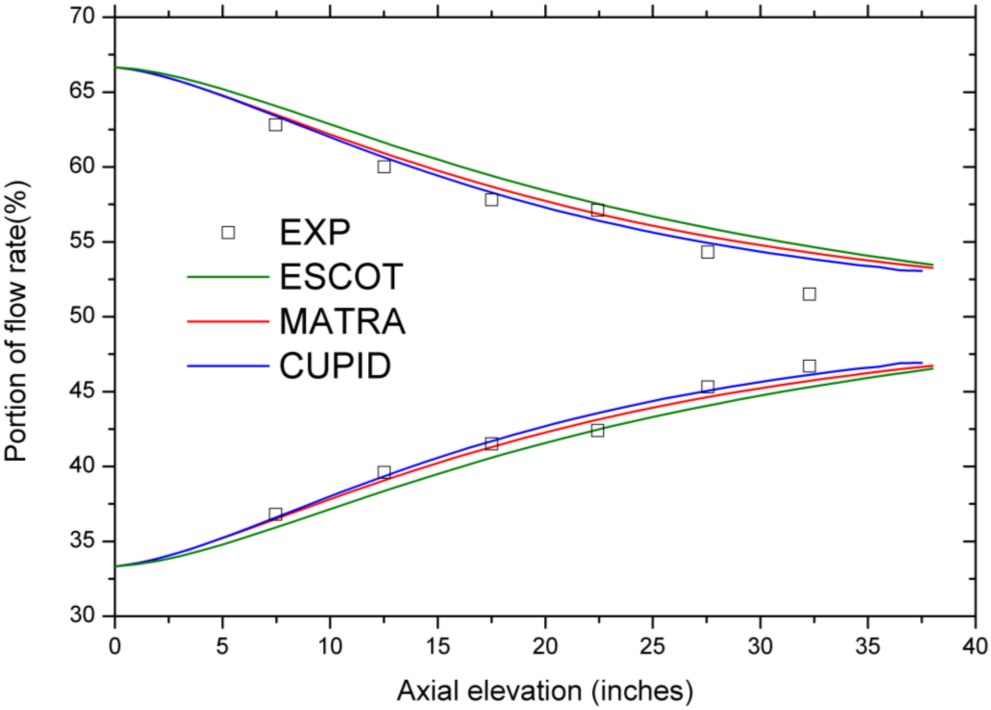

Fig. A.6: portion of assembly averaged flow rate of WH 14*x*14 in the case of partial blockage.

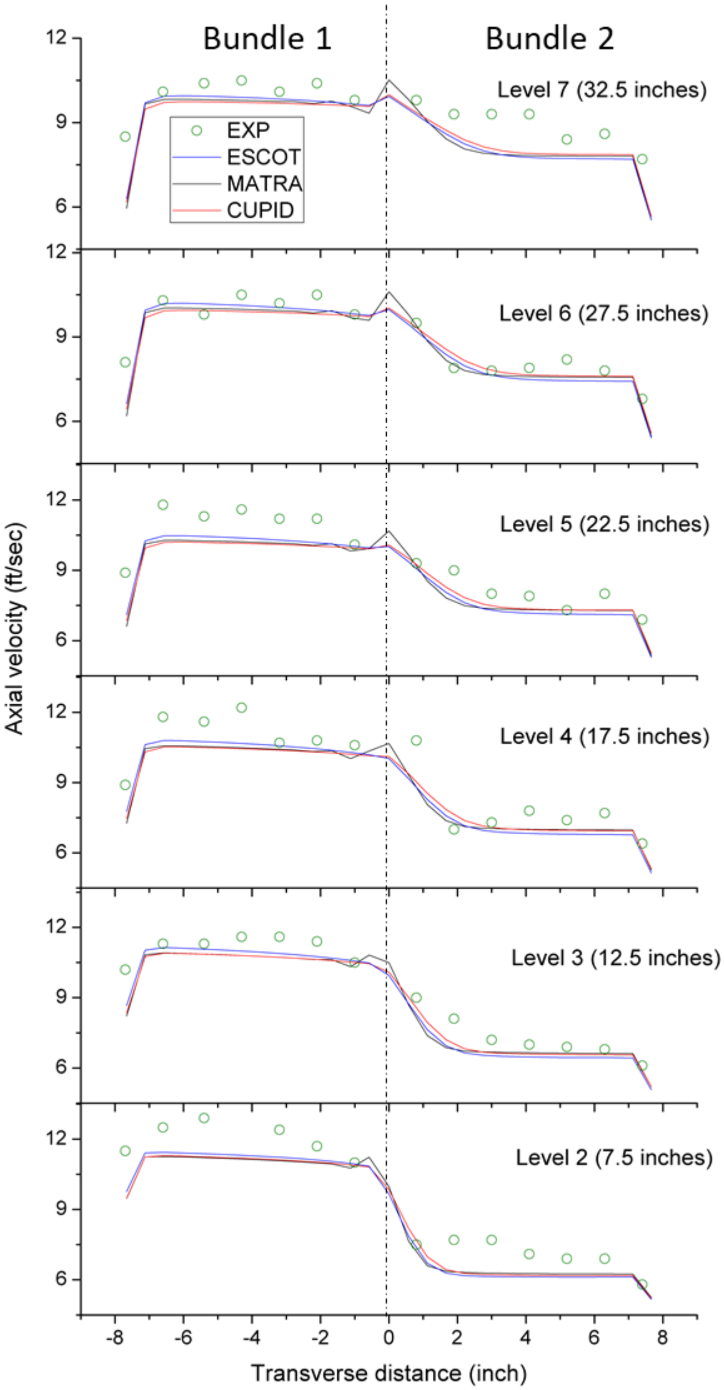

Fig. A.7: comparison of ESCOT prediction towards the experimental data for the partial blockage case.

Tab. A.2: error summary for the WH 14*x*14 partial blockage case.

		Max diff. [%]	**RMS diff. [%]**
Code-to-Exp.	ESCOT	28.12	11.61
	MATRA	29.94	12.06
	CUPID	27.44	11.27
Code-to-code	ESCOT-MATRA	7.54	2.36
	ESCOT-CUPID	4.15	2.09

On the other hand, the axial velocity vector map for full blockage case, taken from the 2nd measuring row, clearly shows the redistribution and reverse flow capabilities of ESCOT (see Fig. A.8). A comparison with CUPID for the full blockage is shown inside Fig. A.9

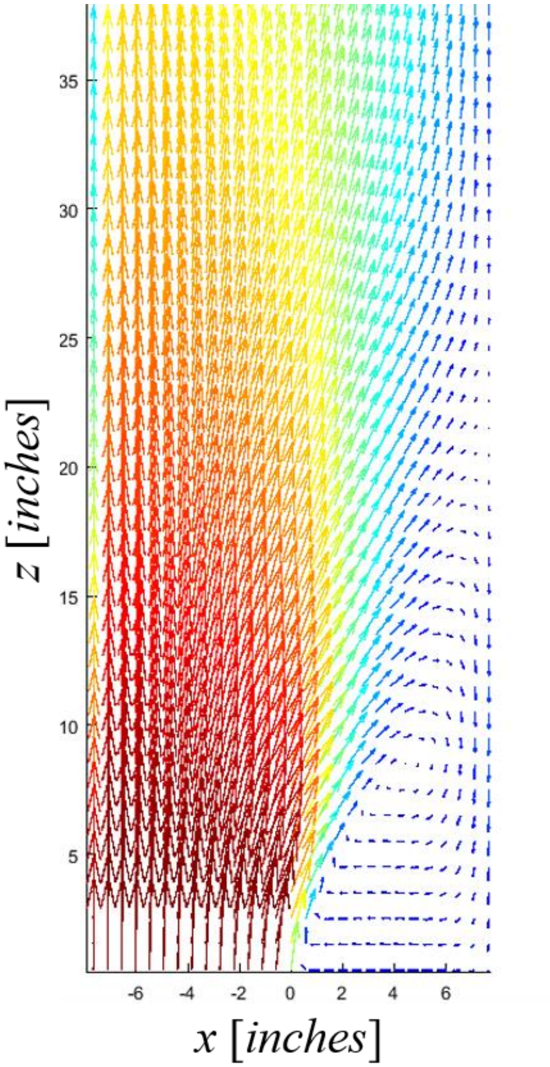

Fig. A.8: velocity vector map at the 2nd measuring row line of WH 14*x*14 full blockage case.

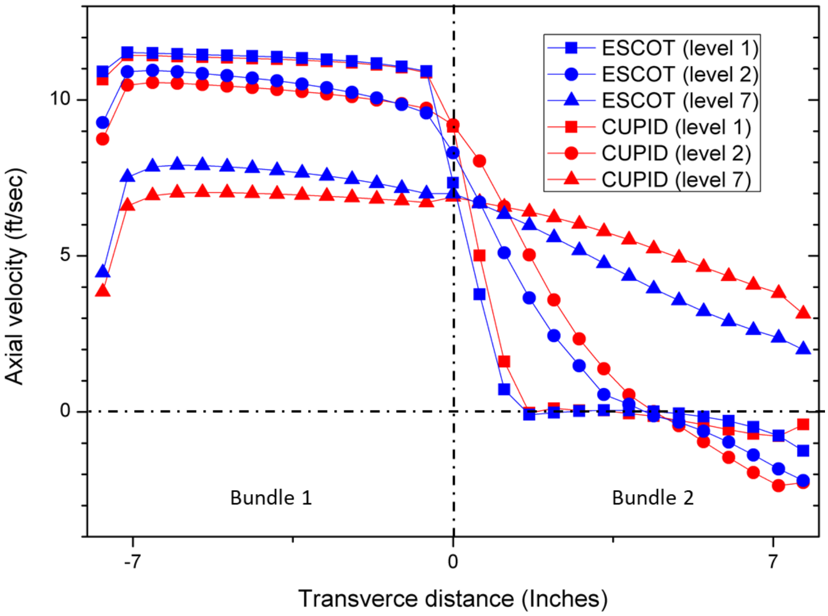

Fig. A.9: comparison of the velocity distribution between ESCOT and CUPID at different axial levels.

The last and important performed test was the PNNL 2*x*6. Twelve rods with an array 2*x*6 are present in the test facility; half part of the facility has, in every different test, a higher power as Fig. A.10 shows. One spacer grid is set in the middle of the test section. Nine windows were positioned axially to measure temperature and velocity field in the central row. Experimental data were available only for window 3 and window 7.

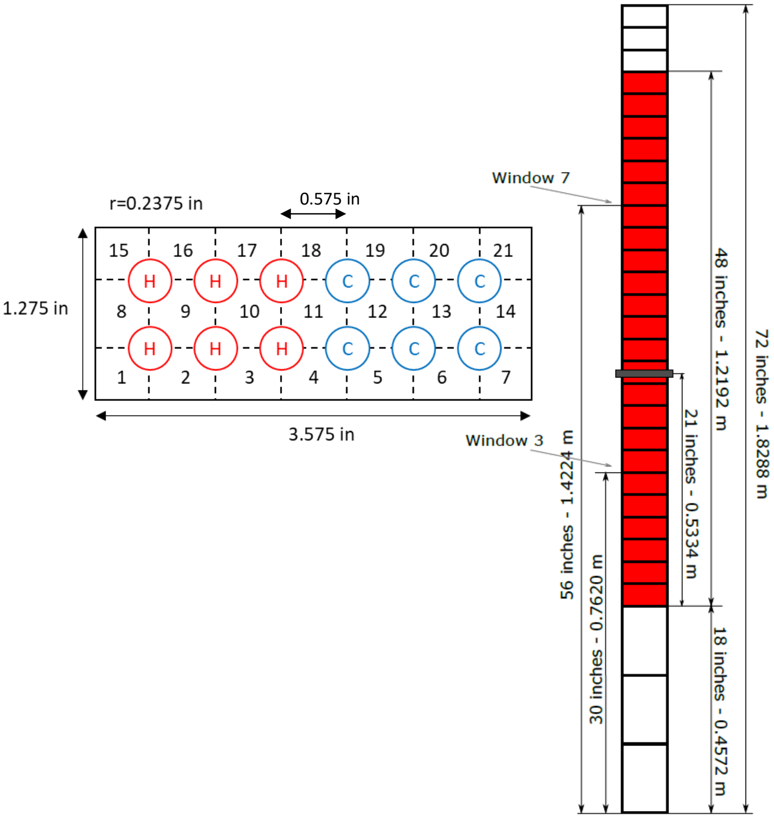

Fig. A.10: radial and axial sketch of the PNNL 2*x*6 test facility.

Fig. A.11 shows the temperature and normalized velocity distribution for the Window 3 for case #2. The velocities are normalized by the inlet velocity. The liquid flow in the hot side is accelerated by the buoyancy effect; ESCOT can catch this phenomenon. The results of ESCOT, when compared to the measured data show some discrepancies, but similar differences appear when CUPID and MATRA are used to solve this experiment as Tab. A.3 shows. The code-to-code comparison can be found in Tab. A.4 and Tab. A.5. The relative differences of the temperature are calculated as divided by the reference temperature expressed in Celsius. ESCOT agrees better with CUPID rather than with MATRA having a 5% RMS difference for each parameter.

More details, such as calculation conditions, boundary conditions and activated models are provided inside this document [76].

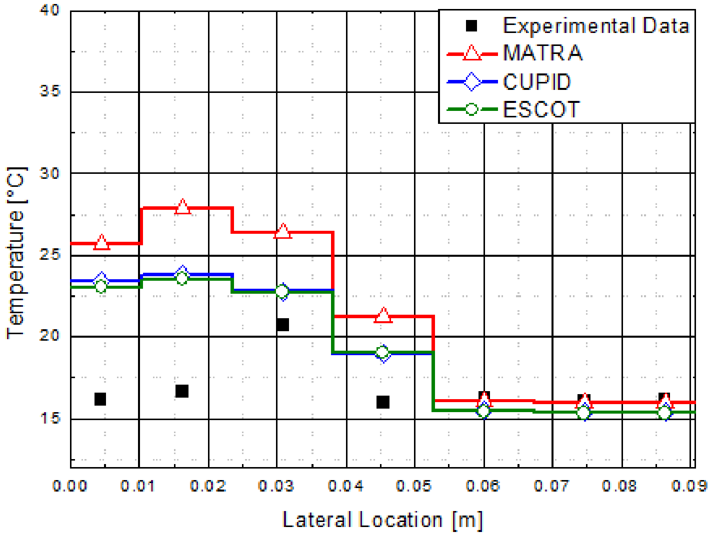

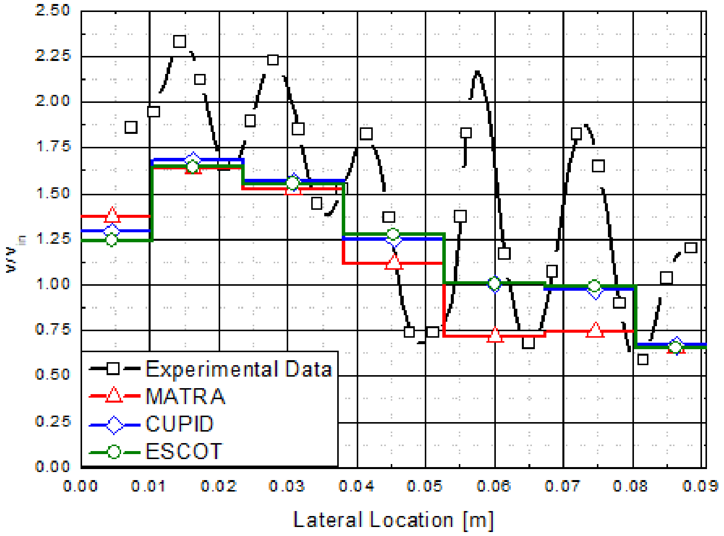

Fig. A.11: comparison with experimental results for temperature (top) and normalized velocity field (bottom) for Case #2 Window 3.

Tab. A.3: comparison of calculated temperature towards the experimental data.

Temperature		**Case #1**				**Case #2**				**Case #3**			
		Max [%]		RMS [%]		Max [%]		RMS [%]		Max [%]		RMS [%]	
		W3	W7	W3	W7	W3	W7	W3	W7	W3	W7	W3	W7
Code-to-Exp.	ESCOT	20.7	29.1	8.6	17.2	42.7	73.3	24.3	30.4	37.9	52.1	15.9	21.5
	MATRA	32.7	30.5	15.8	16.6	67.9	91.3	37.7	42.2	54.4	64.7	27.3	28.7
	CUPID	22.9	31.0	9.2	17.0	45.1	74.5	25.2	30.7	40.3	53.8	16.8	21.7

Tab. A.4: code-to-code comparison for the calculated temperatures.

Temperature		**Case #1**				**Case #2**				**Case #3**			
		Max [%]		RMS [%]		Max [%]		RMS [%]		Max [%]		RMS [%]	
		W3	W7	W3	W7	W3	W7	W3	W7	W3	W7	W3	W7
Code-to-code	ESCOT-CUPID	1.82	1.64	1.39	1.28	1.62	2.88	0.79	1.43	1.70	2.53	0.99	1.22
	ESCOT-MATRA	15.46	7.18	10.80	9.86	15.55	18.09	9.86	11.37	15.95	13.03	9.86	8.23

Tab. A.5: code-to-code comparison for the calculated normalized velocities.

Normalized Velocity		**Case #1**				**Case #2**				**Case #3**			
		Max [%]		RMS [%]		Max [%]		RMS [%]		Max [%]		RMS [%]	
		W3	W7	W3	W7	W3	W7	W3	W7	W3	W7	W3	W7
Code-to-code	ESCOT-CUPID	2.71	2.29	1.58	1.47	3.49	12.07	2.07	6.40	2.78	5.43	1.47	3.50
	ESCOT-MATRA	15.43	11.81	10.80	8.13	40.30	51.33	20.76	30.68	18.56	23.70	11.33	11.79

Appendix 3. Decay Heat Model

The reactor power does not drop immediately to zero when a scram occurs as has been clearly shown inside Chapter 4. After the shutdown, a substantial amount of heat continues to be released through the radioactive decay of both fission products and transuranic elements in the fuel rods. Thus, the released heat depends on the fission product concentrations and the operating history of the reactor. A rigorous computation of decay heat release over time can be carried out by solving a series of coupled differential equations for hundreds of fission products and their daughter nuclides. However, this computation is simplified by fitting a measured decay heat curve to a series of decay heat groups; the calculation is analogous to the delayed neutron solution [90].

The power per unit volume can be expressed as:

$$q'''\left(\vec{r},t\right)=\left(1-\alpha_T\right)\sum_{g=1}^{G}\kappa_g\Sigma_{f,g}\left(\vec{r},t\right)\phi_g\left(\vec{r},t\right)+\sum_{i=1}^{N}\varsigma_i D_i\left(\vec{r},t\right), \qquad \text{(A.26)}$$

where N is the total number of decay heat groups, $D_i\left(\vec{r},t\right)$ represents the concentration of heat precursors in the heat group i in J/cm^3, ς_i is the decay constant of the decay heat group i expressed in sec^{-1} while $\alpha_T=\sum_{i=1}^{N}\alpha_i$ is the total fraction of fission energy appearing as decay heat having α_i as the fraction of total fission energy appearing as decay heat in group i.

The concentration of decay heat precursors $D_i\left(\vec{r},t\right)$ in group i can be expressed by:

$$\frac{\partial D_i\left(\vec{r},t\right)}{\partial t}=\alpha_i\sum_{g=1}^{G}\kappa_g\Sigma_{f,g}\left(\vec{r},t\right)\phi_g\left(\vec{r},t\right)-\varsigma_i D_i\left(\vec{r},t\right). \tag{A.27}$$

The analytical solution can be obtained by integrating Eq. (A.27) over the time interval $\Delta t=t_{n+1}-t_n$:

$$\begin{aligned}&D_i\left(\vec{r},t_{n+1}\right)=D_i\left(\vec{r},t_n\right)\exp\left(-\varsigma_i\Delta t\right)+\\&+\alpha_i\int_{t_n}^{t_{n+1}}\left(\sum_{g=1}^{G}\kappa_g\Sigma_{f,g}\left(\vec{r},t'\right)\phi_g\left(\vec{r},t'\right)\exp\left[-\varsigma_i\left(t_{n+1}-t'\right)\right]\right)dt'\end{aligned}. \tag{A.28}$$

To solve the integral present in Eq. (A.28), a functional form for the time dependent fission source density must be developed. It is reasonable to assume that the fission source density remains constant and equal to the value of the previous time-step over the time interval $t' \subset [t_n, t_{n+1}]$, thus:

$$\sum_{g=1}^{G}\kappa_g\Sigma_{f,g}\left(\vec{r},t'\right)\phi_g\left(\vec{r},t'\right)=\sum_{g=1}^{G}\kappa_g\Sigma_{f,g}\left(\vec{r},t^n\right)\phi_g\left(\vec{r},t^n\right). \tag{A.29}$$

By plugging in Eq. (A.29) into Eq. (A.30), the integral over time becomes trivial and the final expression for $D_i\left(\vec{r},t\right)$ is given as follows:

$$\begin{aligned}&D_i\left(\vec{r},t_{n+1}\right)=D_i\left(\vec{r},t_n\right)\exp\left(-\varsigma_i\Delta t\right)+\\&+\frac{\alpha_i}{\varsigma_i}\left[1-\exp\left(-\varsigma_i\Delta t\right)\right]\left[\sum_{g=1}^{G}\kappa_g\Sigma_{f,g}\left(\vec{r},t_n\right)\phi_g\left(\vec{r},t_n\right)\right]\end{aligned}. \tag{A.31}$$

For the first time-step or the steady-state calculations, it is necessary to know the equilibrium value of the longest lived decay heat precursor group. By setting the time derivative present in Eq. (A.27) equal to zero and by isolating to the LHS the

$D_i\left(\vec{r},t\right)$ term, the equilibrium concentrations can be expressed as:

$$D_i\left(\vec{r},0\right)=D_i^{eq}\left(\vec{r}\right)=\frac{\alpha_i}{\varsigma_i}\sum_{g=1}^{G}\kappa_g\Sigma_{f,g}\left(\vec{r}\right)\phi_g\left(\vec{r}\right). \tag{A.32}$$

Eq. (A.32) is used to determine the initial conditions required for the transient solution of the decay heat equation.

Introducing this model in coupled neutronics-T/H code is not a hard task since the solution of Eq. (A.31) only depends on the previous time-step *κ*-fission and the decay heat constants which are generally provided for the analyzed problem. The ones used inside ESCOT are shown in Tab. A.6. The calculation of the decay heat precursor concentration is performed at the beginning of each time-step and then, when the relative pin-by-pin power is calculated, is added as in Eq. (A.26).

Tab. A.6: decay constants and fraction of total fission energy appearing as decay heat use in the ESCOT code.

ς_i	α_i
$1.05345 \cdot 10^{-1}$	$2.35402 \cdot 10^{-2}$
$8.37149 \cdot 10^{-3}$	$1.89077 \cdot 10^{-2}$
$5.20337 \cdot 10^{-4}$	$1.39236 \cdot 10^{-2}$
$4.73479 \cdot 10^{-5}$	$6.90315 \cdot 10^{-3}$
$3.28153 \cdot 10^{-6}$	$3.56888 \cdot 10^{-3}$
$1.17537 \cdot 10^{-11}$	$3.31633 \cdot 10^{-3}$

References

[1] Joo H. G., Cho J., Kim K. S., Lee C. C., and Zee S. Q., "Methods and Performance of a Three-Dimensional Whole-Core Transport Code DeCART," in: Proceedings of PHYSOR, American Nuclear Society. Chicago, Illinois, USA (2004).

[2] Jung Y. S., Shim C. B., Lim C. H., and Joo H. G., "Practical Numerical Reactor Employing Direct Whole Core Neutron Transport and Subchannel Thermal/Hydraulics Solvers," Annals of Nuclear Energy 62, 357 – 374 (2013).

[3] MPACT Team, "MPACT Theory Manual," CASL-U-2015-0078-000 (2015).

[4] Li Y., Yang W., Wang S., We H. and Cao L., "A three-dimensional PWR-core pin-by-pin analysis code NECP-Bamboo 2.0," Annals of Nuclear Energy 144, 1 – 18 (2020).

[5] Cho H. H., Kang J., Joo I. Y. and Joo H. G., "Analysis of C5G7-TD Benchmark with a Multi-group Pin Homogenized SP_3 Code SPHINCS," Nuclear Engineering and Technology, *in press* (2021).

[6] Jeon S., Choi N. and Joo H. G., "Feasibility of Fast Pinwise Nodal Core Simulation Using GPUs," in: Transaction of the Korean Nuclear Society Autumn Meeting, Changwon, Korea (2020).

[7] Kochunas B., Collins B., Shane S., Salko R., Jabaay D., Graham A., Liu Y., Kim K. S., Wieselquist W., Godfrey A., Clarno K., Palmtag S., Downar T. and Gehin J., "VERA Core Simulator Methodology for Pressurized Water Reactor Cycle Depletion," Nuclear Science and Engineering 185, 217 – 231 (2017).

[8] Choi Y., Cho H., and Cho J., "Multi-physics Solution of VERA Core Physics Benchmark using CUPID and nTER," in: Transactions of Korean Nuclear Society 2019, Autumn Meeting. Goyang, Rep. of Korea (2019).

[9] Jeong J. J., Yoon H. Y., Park I. K. and Cho H. K., "The CUPID code development and assessment," Nuclear Engineering and Technology 42(6), 636 – 655 (2010).

[10] Sánchez-Cervera S., Sabater A., Cuervo D. and García-Herranz N., "Coupled calculations COBAYA4/CTF for MSLB scenarios in the frame of NURESAFE project," in: Proc. of the International Conference on Mathematics and Computational Methods applied to Nuclear Science and Technology 2017 (M&C 2017), Jeju, Rep. of Korea (2017).

[11] Knoll D. A., and Keyes D. E., "Jacobian-free Newton-Krylov methods: a

Survey Approaches and Applications," Journal of Computational Physics 193(2), 357 – 397 (2004).

[12] Hamilton S., Berrill M., Clarno K., Pawlowski R., Toth A., Kelly C. T., Evans T. and Philp B., "An assessment of coupling algorithms for nuclear reactor core physics simulations," Journal of Computational Physics 311, 241 – 257 (2016).

[13] Gaston D. R., Permann C. J., Peterson J. W., Slaughter A. E., Andrš D., Wang Y., Short M. P., Perez D. M., Tonks M. R., Ortensi J., Zou L., and Martineau R. C., "Physics-based Multiscale Coupling for Full Core Nuclear Reactor Simulation," Annals of Nuclear Energy 84, 45 – 45 (2015).

[14] Mylonakis A., Varvayanni M., Catsaros N., Savva P., and Grigoriadis D. G. E., "Multi-physics and Multi-scale Methods Used in Nuclear Reactor Analysis," Annals of Nuclear Energy 72, 104 – 119 (2014).

[15] Toth A., Kelley C. T., Slattery S. R., Hamilton S. P., Clarno K. T., and Pawlowski R., "Analysis of Anderson Acceleration on a Simplified Neutronics/Thermal Hydraulics System," in: Proc. of the Joint International Conference on Mathematics and Computational (M&C), Supercomputing in Nuclear Application (SNA) and Monte Carlo (MC) Method, American Nuclear Society, Nashville, Tennessee, USA (2015).

[16] Anderson D. G., "Iterative Procedures for Nonlinear Integral Equations," Journal of the ACM 12, 547 – 560 (1965).

[17] Lee J., "Development and Optimization of a Neutronics Coupled Refined Core Thermal-Hydraulics Analysis System Capable of Massive Parallel Execution," Ph.D. Thesis, Seoul National Unversity, 1 Gwanak-ro, Gwanak-gu, Seoul 08826, Rep. of Korea (2020).

[18] Zuber N. and Findlay J. A., "Average Volumetric Concentration in Two-phase Flow Systems," Journal of Heat Transfer 87, 453 -468 (1965).

[19] Lee J., "Development of a Drift-Flux Model Based Pinwise Whole Core Thermal-Hydraulics Analysis Code Aiming at Highly Parallelized Execution," M.Sc. Thesis, Seoul National University, 1 Gwanak-ro, Gwanak-gu, Seoul 08826, Rep. of Korea (2016).

[20] Lee J., Facchini A., and Joo H. G., "Development of a Drift-flux Model Based Core Thermal-hydraulics Code for Efficient High-fidelity Multiphysics Calculation," Nuclear Engineering and Technology 51(6), 1487 – 1503 (2019).

[21] Hwang J. T., "Efficient Pin Level Core Transient Simulation Employing Simplified P_3 Method with Multi-Level CMFD Acceleration," M.Sc. Thesis,

Seoul National University, 1 Gwanak-ro, Gwanak-gu, Seoul 08826, Rep. of Korea (2020).

[22] Ivanov K. N., Beam T. M., Baratta A. J., Irani A. and Trikouros N., "PWR Main Steam Line Break Benchmark – Vol. I," NEA/NSC/DOC(99)8 (1999).

[23] Kwon H., Park J. P., Seo K. W., Kim S. J. and Hwang D. H., "Validation of a Subchannel Analysis Code MATRA Version 1.1," KAERI/TR-5581/2014, Daejeon, Rep. of Korea (2014).

[24] Lee J., Joo H. G., Perin Y. and Velkov K., "nTRACER/COBRA-TF Coupling and Initial Assessment," in: Transactions of the Korean Nuclear Society Spring Meeting, Jeju, Rep. of Korea (2015).

[25] Salko R. and Avramova M., "COBRA-TF Subchannel Thermal-Hydraulics Code (CTF), Theory Manual Rev. 0," CASL-U-2015-0054-000, (2015).

[26] Lee J., Facchini A. and Joo H. G., "Radial and Axial Domain Decomposition of a Core Thermal-Hydraulics Code for Massively Parallel Computing Platforms," in: Transactions of the Korean Nuclear Society Spring Meeting, Jeju, Rep. of Korea (2019).

[27] Facchini A., Lee J. and Joo H. G., "Development and Validation of the Two-Phase Flow Analysis Capability of a Drift-flux Model Based Core Thermal-Hydraulics Code ESCOT," in: Proceedings of the International Congress on Advances in Nuclear Power Plants, Juan les Pins, France (2019).

[28] Facchini A., Lee J., Cho J. Y. and Joo H. G., "Development and Assessment of ESCOT Pin-Winse Thermal-Hydraulics Coupling in a Direct Whole Core Calculation Code nTER," in: Transactions of Korean Nuclear Society Spring Online Meeting, Rep. of Korea (2020).

[29] Facchini A., Lee J. and Joo H. G., "nTRACER/ESCOT Initial Coupling and Assessment," in: Transactions of Korean Nuclear Society Spring Online Meeting, Rep. of Korea (2020).

[30] Facchini A., Hwang J. T. and Joo H. G., "Pin level analysis of the NEA/OECD Main Steam Line Break Benchmark Exercise II," in: Transactions of Korean Nuclear Society Autumn Online Meeting, Rep. of Korea (2020).

[31] Kim K. M., Lee J., Choi N. and Joo H. G., "Performance Assessment of GPU-based nTRACER/ESCOT Coupled Simulations," in: Transactions of Korean Nuclear Society Spring Online Meeting, Rep. of Korea (2020).

[32] Van Doormal J. P. and Raithby G. D., "Enhancement of the SIMPLE Method for Predicting Incompressible Fluid Flows," Numerical Heat Transfer 7(2), 147 – 163 (1984).

[33] PETSc Team, “PETSc users’ Manual - Rev. 3.10,” ANL-95/11, Argonne National Laboratory, Glen Forest, Illinois, USA (2018).

[34] Ghiaasiaan S. M., “Two-Phase Flow, Boiling, and Condensation in Conventional and Miniature Systems,” Ch. 15, Cambridge University Press (2007).

[35] Mohiptur M., Jahandarnia G. and Shams M., “An adavancement in iterative solution schemes for three-dimesional, two-fluid modeling of two-phase flow in PWR fuel bundles,” Annals of Nuclear Energy 63, 83 – 99 (2014).

[36] Ishii M. and Mishima K., “Study of Two-Fluid Model and Interfacial Area,” NUREG/CR-1873, ANL-80-111, Argonne National Laboratory, Glen Forest, Illinois, USA (1980).

[37] “The International Association for Properties of Water and Steam”, IAPWS R7-97(2012), Lucerne, Switzerland (2007).

[38] Facchini A. and Lee J., “ESCOT Theory Manual,” SNURPL-TR-050-Rev.2(18), Seoul National University, Rep. of Korea (2019).

[39] Fletcher C. D. and Schultz R. R., “RELAP5/MOD3 Code Manual”, NUREG/CR-5535 INEL-95/0175, vol. 5, Rev. 1 (1995).

[40] Chung B. D., Kim B. D., Bae S. W., Jeong J. J., Lee S. W., Hwang M. K., and Yoon C., “MARS code manual volume I: code structure, system models, and solution methods”, KAERI/TR--2812/2004, Rep. of Korea (2010).

[41] RELAP5 Team, “RELAP5-3D Code Manual Volume IV: Models and Correlations”, INEEL-EXT-98-00834, Revision 2.0 (2002).

[42] Todreas N. E. and Kazimi M. S., “Nuclear systems: Volume I,” II edition, CRC Press, (2011).

[43] Armand A. A., “The resistance during the movement of two-phase system in horizontal pipes,” translated by V. Beak, original in: Izvestiia Vsesoiuznyi Teplotekhnicheskii Institut, 16 – 23 (1946).

[44] Chexal B. and Lellouche G., “The Chexal-Lellouche Void Fraction Correlation for Generalized Applications”, NSAC-139 (1991).

[45] Todreas N. E. and Kazimi M. S., “Nuclear Systems II, Elements of Thermal Hydraulic Design”, Edition I, Taylor and Francis (2001).

[46] Kelly J. E., Kao S. P. and Kazimi M. S. “THERMIT-2: A Two-fluid Model for Light Water Reactor Sub-channel Transient Analysis,” MIT-EL-81-014, Massachusetts Institute of Technology, Cambridge, Massachussets, USA (1981).

[47] Beus S. G., “Two-Phase Turbulent Mixing Model For Flow In Rod Bundles,”

No. WAPD-T--2438, Bettis Atomic Power Lab., Pittsburgh, Pennsylvania, USA (1972).

[48] Lahey R. T., “A Mechanistic Subcooled boiling model,” in: Proceedings of the Sixth International Transfer Conference Vol. 1 293-297, Toronto, Canada, (1978).

[49] Unal H. C., “Maximum Bubble Diameter, Maximum Bubble-Growth Time and Bubble Growth Rate During the Subcooled Nucleate Flow Boiling of Water up to 17.7 MN/m^2,” International Journal of Heat and Mass Transfer 19, 643 – 649 (1976).

[50] Plesset M. S. and Zwick S. A., “The Growth of Vapor Bubbles in Superheated Liquids,” Journal of Applied Physics 25(4), 493 – 500 (1954).

[51] Lee K. and Ryley D. J., “The Evaporation of Water Droplets in Superheated Steam,” in Transactions of ASME, Journal of Heat Transfer, 445 – 451 (1968).

[52] Kreith F., “Principles of Heat Transfer”, 3rd Edition, New York: Intex Educational (1973).

[53] Theofanous T. G., “Modeling of basic condensation processes,” The Water Reactor Safety Research Workshop on Condensation, Silver Springs, Maryland, USA (1979).

[54] Brown G., “Heat Transmission of Condensation of Steam on a Spray of Water Drops,” in Proceedings of the General Discussion on Heat Transfer 1951, published by the Institution of Mechanical Engineers, 49 – 52 (1951).

[55] Dittus F. W. and Boelter L. M. K., “Heat Transfer in Automobile Radiators for the Tubular Type,” in: Publication in Engineering 2, 443 – 461, University of California, Berkely, California, USA, (1930).

[56] Sparrow E. M., Loeffer Jr. A. L. and Hubbard H. A., “Heat Transfer to Longitudinal Laminar Flow Between Cylinders,” Journal of Heat Transfer 83(4), 415 – 422 (1961).

[57] Wong S. and Hochreiter L. E., “Analysis of the FLECHT SEASET unblocked bundle steam-cooling and boiloff tests,” No. EPRI-NP—1460, Westinghouse Electric Corp. (1981).

[58] Chen J. C., “A Correlation for Boiling Heat Transfer to Saturated Fluids in Convective Flows,” Industrial & Engineering Chemistry Process Design and Development 5(3), 322 – 329 (1963).

[59] Thom J. R. S., Walker W. M., Fallon T. A. and Reising G. F. S., “Boiling in subcooled water during flow up heated tubes or annuli,” in Symposium on Boiling Heat Transfer in Steam Generating Units and Heat Exchangers, 15 –

16, (1966).

[60] Jens W. H. and Lottes P. A., “Analysis of heat transfer, burnout, pressure drop and density data for high pressure water,” ANL-4627, Argonne National Laboratory, Glen Forest, Illinois, USA (1951).

[61] Forster H. K. and Zuber N., “Dynamics of vapor bubbles and boiling heat transfer,” AlChE Journal 1(4), 531 – 535 (1951).

[62] Collier J. G., “Heat transfer in the post dryout region during quenching and reflooding,” in G. Hetsroni ed., Handbook of Multiphase Systems, New York, USA (1982).

[63] Hancox W. T. and Nicoll W. B., "A general technique for the prediction of void distributions in non-steady two-phase forced convection," International Journal of Heat and Mass Transfer 14(9), 1377 – 1394 (1971).

[64] Geelhood K. J., Luscher W. G., Raynaud P. A., and Porter I. E., “FRAPCON-4.0: A Computer Code of Steady-state, Thermal-Mechanical Behavior of Oxide Fuel Rods for High Burnup,” PNNL-19418, Pacific Northwest National Laboratory, Richland, Washington, USA (2015).

[65] Hales J. D., Williamson R. L., Novascone S. R., Pastore G., Spencer B. W., Stafford D. S., Gamble K. A., Perez D. M. and Liu W., “BISON theory manual the equations behind nuclear fuel analysis,” INL/EXT-13-29930, Idaho National Lab, Idaho Falls, Idaho, United States (2016).

[66] Hagrman D. L., Reymann G. A. and Mason R. E., “MATPRO – Version 11 (Revision 2): A Handbook of Material Properties for Use in the Analysis of Light Water Reactor Fuel Rod Behavior,” NUREG/CR-0497, TREE-1280, US Nuclear Regulatory Commission, USA (1981).

[67] Groeneveld D. C., Leung L. K. H., Guo Y., Vasic A., El Nakla S. W., Peng J., Yang J. and Cheng S. C., “Lookup tables for predicting CHF and film-boiling heat transfer: past, present and future,” Nuclear Technology 152(1), 87 – 104 (2005).

[68] Biasi L., Clerici G. C., Garribba S., Sala R. and Tozzi A., “Studies on burnout. Part 3: a new correlation for round ducts and uniform heating and its comparison with world data,” ARS SpA, University of Milan, Milan, Italy (1967).

[69] Bjornard T. A. and Griffith P., “PWR blowdown heat transfer,” in Thermal and Hydraulic Aspects of Nuclear Reactor Safety, vol. 1, 17 – 41, ASME (1977).

[70] Marinelli V., Kjellen B. and Pastori L., “Experimental investigation of mass velocity distribution and velocity profiles in an LWR rod bundle,” European

Two-Phase Flow Group Meeting, Italy (1972).

[71] Chemlemer H., Chu P. T. and Hochreiter L. E., "THINC-IV: an improved program for thermal-hydraulic analysis of rod bundle cores", WCAP-7956, Westinghouse Electric Corp., (1973).

[72] Quigley M. S., McMonagle C. A. and Bates J. M., "Investigation of Combined Free and Forced Convection in a 2x6 Rod Bundle", BNWL-2216 (1977).

[73] Sterner R. W. and Lahey Jr. R. T., "Air-Water subchannel measurement of equilibrium quality and mass flux distribution in a rod bundle," NUREG/CR-3373 (1983).

[74] Lahey Jr. R. T., Shiralkar B. S. and Radcliffe D. W., "Two-phase flow and heat transfer in multirod geometries: subchannel and pressure drop measurements in a nine-rod bundle for diabatic and adiabatic conditions," GEAP-13049, General Electrics, (1970).

[75] Rubin A., Schoedel A., Avramova M., Utsuno H., Bajorek S. and Velazquez-Lozada A., "OECD/NRC Benchmark based on NUPEC PWR sub-channel and bundle tests (PSBT) – Volume I," NEA/NSC/DOC(2012)1, OECD (2012).

[76] Facchini A. and Lee J., "ESCOT Validation & Verification Manual," SNURPL-051-Rev.2(18), Seoul National University, Seoul, Rep. of Korea (2019).

[77] Salko R. K., Blyth T. S., Dances C. A., Magedanz J. W., Jernigan C., Kelly J., Toptan A., Gergar M., Gosdin C., Avramova M. N., Palmtag S. and Gehin J. C., "CTF Validation and Verification," CASL-U-2016-1113-000, Penn State, University Park, Pennsylvania, USA (2016).

[78] Kochunas B., Fitzgerald A. and Larsen E., "Fourier analysis of iteration schemes for k-eigenvalue transport problems with flux-dependent cross sections," Journal of Computational Physics 345, 294 – 307 (2017).

[79] Folland G. B., "Fourier Analysis and Its Application," pp. 60 – 61, Wadsworth: Brooks/Cole Edition, Pacific Grove, California, USA (1992).

[80] Kuo B. C. and Golnaraghi M. F., "Automatic Control System – 8th Edition," pp. 236 - 237, John Wiley & Sons, Inc., New York, New York, USA (2002).

[81] Fang H. and Saad Y., "Two classes of Multisecant Methods for Convergence Acceleration of Iterative Sequences," Numerical Linear Algebra with Applications 16(3), 197 – 221 (2009).

[82] Walker H. F. and Ni P., "Anderson Acceleration for Fixed-Point Iterations," SIAM Journal on Numerical Analysis 49(4), 1715 – 1735 (2011).

[83] Eyert V., "A Comparative Study on Methods for Convergence Acceleration of

Iterative Vector Sequences," Journal of Computational Physics 124(2), 271 – 285 (1996).

[84] An H., Jia X., and Walker H. F., "Anderson Acceleration and Application to the Three-temperature Energy Equations," Journal of Computational Physics 347, 1 – 19 (2017).

[85] Walker H. F., "Anderson Acceleration: Algorithms and Implementations," Research Report MS-6-15-50, Worcester Polytechnic Institute, Mathematical Sciences Department, Massachusetts, USA (2011).

[86] Horelik N., Herman B., Forget B. and Smith K., "Benchmark for Evaluation and Validation of Reactor Simulations (BEAVRS), v1.0.1," in: Proceedings of International Conference on Mathematics and Computational Methods Applied to Nuclear Science and Engineering, Sun Valley, Idaho, USA (2013).

[87] Facchini A., Lee J. and Joo H. G., "Investigation of Anderson Acceleration in Neutronics-Thermal Hydraulics Coupled Direct Whole Core Calculation," Annals of Nuclear Energy 153, (2021).

[88] González-Amorós J., Cho H. H. and Joo H. G., "Validation of the Multi-Group Pin Homogenized SP3 Code SPHINCS through BEAVRS Benchmark Analyses," in: Transactions of the Korean Nuclear Society Spring Online Meeting, Rep. of Korea (2020).

[89] Joo H. G., Cho B.-O., Yoo Y. J. and Zee S.-Q., "Analysis of OECD MSLB Benchmark Exercise II using the MASTER Code," in: Proceedings of the International Conference on Mathematics and Computational Methods applied to Nuclear Science and Technology (M&C) 1999, Madrid, Spain (1999).

[90] Dunn F. E., "Decay Heat Calculations for Transient Analysis," Transactions of the American Nuclear Society Winter Meeting, California, USA (1989).

[91] Taylor J. B. and Ivanonv K. N., "Statistical methods used for code-to-code comparisons in the OECD/NRE PWR MSLB benchmark," Annals of Nuclear Energy 27(17), 1589 – 1605 (2000).

[92] Marinelli V., Kjellen B. and Pastori L., "Experimental investigation of mass velocity distribution and velocity profiles in an LWR rod bundle", European Two-Phase Flow Group Meeting, Italy (1972).

[93] Chemlemer H., Chu P. T. and Hochreiter L. E., "THINC-IV: an improved program for thermal-hydraulic analysis of rod bundle cores", WCAP-7956, Westinghouse Electric Corp. (1973).

[94] Quigley M. S., McMonagle C. A. and Bates J. M., "Investigation of Combined Free and Forced Convection in a 2x6 Rod Bundle", BNWL-2216 (1977).